Experimental study on the aerodynamic performance of feather-inspired flexible structures for development of a perceptible and intellectual flying robot

February 2023

YUTA MURAYAMA

Graduate School of

Science and Engineering

CHIBA UNIVERSITY

（千葉大学審査学位論文）

Experimental study on the aerodynamic performance of feather-inspired flexible structures for development of a perceptible and intellectual flying robot

February 2023

YUTA MURAYAMA

Graduate School of

Science and Engineering

CHIBA UNIVERSITY

Abstract

For man-made flying vehicles such as drones that fly at low altitudes in the atmospheric boundary layer, where they are exposed to unpredictable wind disturbance such as gust, the loss of attitude stability due to the wind disturbance is one of challenges to overcome. On the other hand, birds and other flying animals, which are also affected by wind disturbance, are thought to have acquired their superior flight capabilities through evolution and adaptation, and engineers have studies inspired by the flight of the natural flyers to improve the performance of artificial flyers. However, the mechanisms of birds' superior flying ability have not been completely revealed, and there must remain a lot of valuable knowledge about bird flight, which is contained in unsteady hydrodynamic phenomena in the transitional Reynolds number.

In this thesis, first, several wing models with flexible flaps inspired by the flexible covert feathers of birds were developed to suppress aerodynamic fluctuations by passive mechanisms that enhance the robustness of flying robots. To evaluate the aerodynamic performance of the wing models, aerodynamic force measurements and flow visualization (PIV) were conducted in wind tunnel, with a specific focus on its robustness against disturbances. In addition, feather-based flexible sensors were also developed for use in sensing airflow near the wing surface, taking the inspiration from covert feathers as before. Wind tunnel experiments were conducted to evaluate the sensing function and aerodynamic characteristics of the feather-based flexible sensors that behaves like fluttering due to the wind. As a result, it was shown that the feather-based sensor has the potential to provide a sensing function capable of predicting stalls, which can be dangerous for flying robots. These feather-based devices have shown that their simplicity can be used as convenient methods to improve the flight stability of small fixed-wing flying robots working under disturbed wind environments.

Development of bird-inspired robot was further carried out to utilize the feather-based devices with passive mechanisms. The robot, which has a bird-inspired multi-degrees-of-freedom morphing tail, can actively control redundant aerodynamic forces and aerodynamic moments with its wings and tail. The robot can be used as a platform to develop stable flight control methods utilizing airflow information.

Acknowledgement

First and foremost, I would like to express my sincere gratitude to my supervisor, Professor Hao Liu, and Associate Professor Toshiyuki Nakata for their support and help in pursuing my research. I owe a special thanks to them for their intelligent advice that has given me so much significant insights into my study.

I sincerely thank Associate Professor Akio Namiki, Associate Professor Satoshi Suzuki and Professor Sachiyo Arai who accepted to be a committee member and review my thesis, giving me valuable suggestions.

I also thank faculty members of the Center for Aerial Intelligent Vehicle (CAIV) for providing a lot of precious suggestions, including Associate Professor Kouichi Yonezawa, and Researcher Saori Tanaka.

I sincerely thank my colleague, Dr. Sakito Koizumi for his uncountable help, camaraderie, and fruitful discussions in the six years, and all members of Biomechanical Engineering Laboratory for their helps and valuable discussions. I owe thanks to Dr. Ryusuke Noda and Dr. Takashi Fujiwara, former members of the laboratory, for giving me a lot of advice and help in my research life. I would also thank secretary of the laboratory Ms. Tamiko Kanke for her help and support.

I want to appreciate to Dr. Takeo Fujii and Dr. Teruaki Ikeda of TERAL Inc. for their advice on my undergraduate study. I would also thank TERAL Inc. for building the wind tunnel apparatus at Chiba University that I used in the experiments of my study.

Finally, I would like to express my gratitude to my families who have supported my life at Chiba University.

This work was supported by Grant-in-Aid for Scientific Research of KAKENHI Numbers 18H05468, 19H02060, and 20H02107, JSPS, Grant Number JPMJSP2109, JST SPRING, and a Global Prominent Research Program and Aerial Intelligent Vehicle Program, Chiba University.

Yuta Murayama

Graduate School of Science and Engineering, Chiba University

February 2023

Contents

List of Figures

List of Table

Chapter 1

General Introductions

1.1 Background

As unmanned aerial vehicles, called drones or micro aerial vehicles (MAVs), have been developed and used for various tasks recently (Floreano and Wood, 2015), it is becoming increasingly important to make further improvements in their flight capabilities, particularly in terms of stability and efficiency. MAVs flying in airspace closer to the grand surface than airplanes are exposed to the strong and unpredictable effects of winds caused by the atmospheric boundary layer, which deteriorates their flight stability and efficiency (Watkins et al., 2020). Further improvements in safety and reliability of flying robots against unpredictable wind disturbances are needed for them to safely perform wider tasks, especially in urban areas. Although superior flight control methods for multi-rotor drones have been developed (e.g., Kazim et al., 2021; Suzuki, 2018), there are only a few attempts to make the hardware of a flying robot more robust against the wind effects. Approaches that make a flying robot more robust against wind effects from the viewpoint of aeronautical engineering, fluid dynamics and biomimetics could lead to further advances in the performance of a flying robot.

To deal with the challenge of improving drone flight capabilities, engineers have often used methods inspired by the abilities of flying animals in nature, known as biomimetics. Birds, with superior performance in variable wind environments, are often chosen as a source of ideas for improving the capabilities of flying vehicles (Bechert et al., 2000; Luca et al., 2017). One reason why birds are considered a source of inspiration for the development of a flying robot is that birds and drones are similar in size (i.e., similar in Reynolds number) . Birds have various features in their design, such as flexible muscles and wings, and a variety of their flight modes and flight techniques, which distinguish

them from man-made flying robots with rigid components. Although birds are exposed to the ever-changing wind environment in nature, as well as drones, the fact that flying animals, including birds, have evolved and flourished while adapting to such harsh environments is noteworthy. For example, it has been observed that the common kestrel can hover in windy conditions while keeping its center of gravity fluctuating slightly (Videler et al., 1983), suggesting that the bird has acquired the ability to hover with great stability. In addition to the stable hovering performance, birds that use wind well to fly long distances are expected to provide insights for superior flight efficiency. Inspired by bird soaring, an attempt to utilize wind in glider drone flight has been proposed (Reddy et al., 2018).

This chapter presents general overviews of knowledge about the superior flight capabilities of birds and technologies related to flying robots that have been developed inspired by natural flyers including birds.

1.2 Avian Flight

Unpredictable wind can be a risk to the stability of flying objects, including drones and natural flyers. However, It is thought that over 10,000 species of birds have evolved through a long period of time to adapt to the diverse environments of all over the world, such as oceans, mountains, and deserts, and have acquired superior flight performance (Chin et al., 2017; Sullivan et al., 2017; Xu et al., 2014). Birds have various features that distinguished them from artificial flying robots. It has been suggested that these features enhance their flight capabilities. In this section, some general information about bird flight with remarkable features are introduced.

1.2.1 Morphology of bird wing

It is believed that a bird has acquired body design optimized for flight through natural selection: it is composed of lightweight bones and asymmetric feathers that are advantageous for flying (Sullivan et al., 2016, 2017, 2019), and it has a large number of sensory organs to sense the airflow near its surface (Brown and Fedde, 1993). Some studies have suggested that the flight muscles that generate the flapping motion can also act like the suspension of a vehicle to dampen the effects of wind disturbances such as

gusts (Cheney et al., 2020; Reynolds et al., 2014). The morphology of the birds, which has many unique characteristics that differ from those of artificial flying robots, is thought to contain interesting insights that could be useful in development of flying robots.

A unique characteristic of birds, that differ from other flying animals such as insects and bats, is that their bodies are covered with many feathers (Fig. 1.1(A)), which allow them to transform the shape of their wings and tails (Matloff et al. 2020). This deformability is called morphing, and birds can adjust the aerodynamic forces generated by their wings and tail morphing to control their flights (Harvey et al., 2022; Lentink et al., 2007). It is assumed that birds can optimize their flight profiles by morphing, such as spreading or sweeping wings and tail, according to their flight modes and speed (Videler, 2006). Birds are also able to independently control their left and right wings and tail morphing to achieve highly maneuverable flight (Gillies et al., 2011). Interestingly, bird tail, which is not seen in other flying animals, is decoupled from the rest of the body parts (Gatesy at al., 1993), and is controlled independently, indicating that it functions specifically for flight control (Harvey et al., 2022).

Avian feathers have been observed to deform in interaction with aerodynamic forces and are thought to benefit aerodynamic performance of birds' flight (Carruthers et al., 2007). In spite of being flexible and lightweight compared to the artificial materials, the feathers have an extremely elaborate and complex design with a microscopic level hierarchical structure and transmissibility (Sullivan et al., 2016; Müller and Patone, 1998), which also provide aerodynamic functions. it is known that flight feathers, such as primaries, have asymmetric shape around the feather shaft (rachis) (top and middle of Fig. 1.1(B)) and that the feathers themselves contribute to generate aerodynamic forces (Klaassen et al., 2020.). The aerodynamic function of asymmetric feather also provided evidence to support the hypothesis that some of feathered dinosaurs such as Archaeopteryx was able to fly (Feduccia and Tordoff, 1979) (bottom of Fig. 1.1(B)). It has been suggested that the slits of primaries seen in some species such as a hawk (Figs. 1.1(A) and 1.1(C)) help reduce induced drag (Tucker, 1995). Feathers on dorsal and ventral wing surface, called coverts, have been observed to float up by wind (Fig. 1.1(A) and 1.1(D)) and it has been hypothesized that their deformation may function as the device of passive flow controlling and sensing (Brown and Fedde, 1993; Carruthers et al., 2007) (top of Fig. 1.1(E)). In addition, several previous studies have indicated that the passive deformable structures inspired by avian coverts are also effective in enhancing aerodynamic performance as applied to airfoils of aircrafts (Bechert et

al., 2000; Rosti et al., 2017; Schlüter, 2009). The feather called alula, which is small structure on the leading edge at the joint between hand-wing and arm-wing (Fig. 1.1(A)), is observed to be used in slow and high angles of attack flight such as landing phase (Carruthers et al., 2007). The alula has been assumed to increase lift and delay stall in the similar role as the leading-edge slat of aircrafts (Álvarez et al., 2001; Lee et al., 2015) (bottom of Fig. 1.1(E)).

1.2.2 Flight modes of birds

Birds can flap their wings to fly in common, except for terrestrial species. Birds perform flapping motion to generate the lift and thrust forces necessary for highly maneuverable flight, such as forward, such as forward flight, steep climb, sharp turning, and hovering (Videler, 2006). In addition, birds also use other flight modes such as gliding and soring flight. Gliding flight is a method for efficiently traveling long distances by converting the sinking velocity gained with altitude loss into forward speed and lift force (Tucker, 1987). Soaring flight is a type of gliding performed by capturing updraft wind, which makes it possible to fly for a long time or gain altitude without flapping (Tucker and Parrott, 1970). It is thought that birds fly by appropriately switching between these flight modes and adjusting the balance between efficiency and maneuverability. It is known that larger species tend to perform gliding and soaring flights more frequently because their heavier body weight requires more energy to flap their wings (Williams et al., 2020). It has been suggested that a mode of flight called intermittent flight, in which some birds perform alternating flapping and gliding, is efficient (Tobalske, 2007). The bird's ability to switch various flight modes in response to the situation is one of the difficulties that a flying robot with certain flight configuration cannot easily replicate.

Kestrel (*Falco tinnunculus*) is one of the species that performs a unique flight: intermittent flight and hanging flight. It has observed that the kestrels search for food while using the wind in their flight known as hanging and wind hovering (Videler et al., 1983; Videler and Groenewold, 1991). Their study shows that the kestrel can suppress the variation of its center-of-gravity’s position while wind hovering in strong winds. Their remarkably stable flight may have been achieved by active or passive flight control with fully utilizing the sensory organs and morphing ability (Mohamed et al., 2014). Such a highly stable flight, which has not been achieved by current bird-modeled flying robots, may be a hint for how a flying robot overcomes the effects of unpredictable wind disturbances.

1.3 Bio-inspired engineering

1.3.1 Flying robots inspired by a bird flight

Superior flight abilities of birds can be a source to extend the envelope of the capability of a flying robot. In order to improve the performance of flying robots, engineers have often taken an approach called biomimetics, which is the engineering application of the superior essence of flying animals. In this section, various types of bird-inspired flying robots that have been developed by applying the functions of birds are introduced (Fig. 1.2).

The RoboSwift team (2007) developed a MAV, called RoboSwift, inspired by common swift. RoboSwift had wingspan of approximately 50 cm and a weight of less than 100 g, and it was able to hold its wing backwards like the common swift dose (Fig. 1.2(A)). In contrast to the RoboSwift that had a wing morphing function, around the same time, Parga et al. (2007) developed the fixed-wing MAV with a tail that had two degrees of freedom in elevation and rotation angle relative to the body (Fig. 1.2(B)). This rotatable tail is one example of the studies that demonstrated that aerodynamic forces can be controlled by tail independently from the main wings. Flapping types of MAV, known as an ornithopter, have been developed (Figs. 1.2(C), 1.2(D), and 1.2(E)). The ornithopter type gets lift and thrust force to fly by flapping its wings, mimicking the flapping flight of a bird. In order to actuate the flapping motion, a single motor connected to a gear box and crank mechanism (e. g., crank-rocker mechanism) was often used (Gerdes et al., 2014; Yang et al., 2018). Similar in concept to the RoboSwift, several variations of propeller-type MAVs with morphing wings have been developed in recent years (Figs. 1.2(F), 1.2(G), and 1.2(H)). MAVs with morphing wings commonly benefit especially in maneuverability, such as turning, through asymmetric shape control of the left and right wings (Luca et al., 2017; Ajanic et al., 2020).

1.3.2 Airflow sensors in birds and engineering

Birds have rich sensory organs to detect the changes of airflow and atmospheric pressure, called a mechanoreceptor (Fig. 1.3(A)). Altshuler et al. (2014) described the function of mechanoreceptors that slowly adapting receptors like Merkel cells and Ruffini endings sense the forces that sustain the

deformation of feathers and skin, such as wind speed and stall (Necker 1985), whereas vibration receptors like Herbst corpuscles function to discriminate the high-frequency elements of flow disturbances (Hörster 1990). It is also known that mechanoreceptors are exist in other flying animals such as insects and bats. Sterbing-D'Angelo et al. (2011) studied that removing the microscopic hairs on the membranous wings of bats resulted in a deterioration of their flight performance. It is assumed that flying animals use environmental information obtained from these micro-sensory organs to fly in unpredictable wind disturbances.

Similar to the biological airflow sensors (mechanoreceptors), miniature size sensors with engineering mechanisms, also called MEMS, have been developed in previous studies. MEMS flow sensors are commonly categorized into two types based on the differences in their sensing mechanisms. One is a mechanical type that use a cantilever-based structure and can sense flows by its strain changes caused by the deformation of cantilever (Fig. 1.3(B)). The other is a thermal type that can sense the flow rate by measuring resistance of a heating element or current values required to keep the heating element temperature (Fig. 1.3(C)). These miniature sensors, which can be designed to be small, lightweight, and flexible, are considered to be compatible with MAVs. It has been also proposed to integrate these small and flexible sensors into the MAVs' configuration (Fig. 1.3(D)). Although these small flow sensors are considered potentially useful for applications in MAVs, research into flow-based sensing is still underdeveloped, with few proven in-flight systems available (Mohamed et al., 2014). Apart from engineering applications such as MAVs, these sensors have also shown their availability in the biological field. Takahashi et al. (2012) developed a piezo resistive cantilever type differential pressure sensor (Fig. 1.3(E)) and showed that the sensor can be also applied for biologging of seabirds (Fig. 1.3(F)) (Takahashi et al., 2018).

As discussed in previous studies, birds have the flow-sensing sensor function that contribute to their flight performance, and engineering sensors have been developed that can replace it. However, these engineering sensors, which were not necessarily designed to be biomimetic, do not provide the multifunctionality often found in living organisms, but were developed to specialize only in flow-sensing function. On the other hand, birds use their feathers as sensing elements to detect airflow with their mechanoreceptors (Fig. 1.3(A)) and may also use their feathers for airflow control, as described in Subsection 1.2.1. The development of an airflow sensor inspired by the multifunctionality found in bird

feathers is expected to enhance the applicability of such airflow sensors to a bird-based flying robot. A feather-based airflow sensor is presented in Chapter 3 of this thesis.

1.4 Objective of this study

In this thesis, several methods to enhance capability of the aerodynamic performances inspired by the birds' flight were studied, aiming at development of a perceptible and intellectual flying robot that will be highly robust against wind disturbances.

Taking inspiration from the covert feathers of a bird described in Subsection 1.2.1, the effect of a feather-like flexible structure, that deforms passively in response to wind disturbances, on the aerodynamic performance of a fixed wing was examined. The wing model with covert-inspired flexible flaps were fabricated and tested in wind tunnel experiments. Its performance was investigated through aerodynamic force measurements and flow visualization experiments (PIV), and discussions also are held regarding its robustness against wind disturbances.

Design and fabrication of airflow sensors, also inspired by covert feathers, were then carried out for the purpose of detecting wind disturbances and assisting the active attitude control of a flying robot. The sensing and aerodynamic characteristics of these sensors, that is capable of detecting changes in airflow as the deformations, were evaluated in wind tunnel experiments. With a specific focus on their applicability to a flying robot, the perceptibility of these sensors is discussed.

Then, development of a bird-shaped flying robot that can be equipped with a wind sensor and actively control its aerodynamics and attitude was carried out. The robot was designed and fabricated so that it has a multi-degree-of-freedom morphing tail suitable for active aerodynamic moment control independently of the wings that are equipped airflow sensors. The aerodynamic controllability of the morphing tail was investigated in wind tunnel experiments and discussed with a focus on how the attitude change of the tail can be used to actively control aerodynamic forces.

References

Ajanic, E., Feroskhan, M., Mintchev, S., Noca, F. and Floreano, D. (2020) Bioinspired wing and tail morphing extends drone flight capabilities. *Sci. Robot.* **5**, eabc2897, doi: 10.1126/scirobotics.abc2897.

Altshuler, D. L., Bahlman, J. W., Dakin, R., Gaede, A. H., Goller, B., Lentink, D., Segre, P. S., and Skandalis, D. A. (2014) The biophysics of bird flight: Functional relationships integrate aerodynamics, morphology, kinematics, muscles, and sensors. *Can. J. Zool.* **93**, 961-975, doi: 10.1139/cjz-2015-0103.

Álvarez, J. C., Meseguer, J., Meseguer, E., and Pérez, A. (2001) On the role of the alula in the steady flight of birds. *Ardeola* **48**, 161-173.

Bechert, D.W., Bruse, M., Hage, W., and Meyer, R. (2000) Fluid mechanics of biological surfaces and their technological application. *Naturwissenschaften* **87**, 157-171, doi: 10.1007/s001140050696.

Brown R. E. and Fedde M. R. (1993) Airflow sensors in the avian wing. *J. of Exp. Biol.* **179**, 13-30.

Carruthers, A. C., Thomas, A. L. R., and Taylor, G. K. (2007) Automatic aeroelastic devices in the wings of a steppe eagle *Aquila nipalensis*. *J. Exp. Biol.* **210**, 4136-4149, doi: 10.1242/jeb.011197.

Chang, E., Matloff, L. Y., Stowers, A. K., and Lentink, D. (2020) Soft biohybrid morphing wings with feathers underactuated by wrist and finger motion. *Sci. Robot.* **5**, eaay1246, doi: 10.1126/scirobotics.aay1246.

Cheney, J. A., Stevenson, J. P. J., Durston, N. E., Song, J., Usherwood, J. R., Bomphrey, R. J., and Windsor, S. P. (2020) Bird wings act as a suspension system that rejects gusts. *Proc. R. Soc. B* **287**, 20201748, doi: 10.1098/rspb.2020.1748.

Chin D. D., Matloff L. Y., Stowers A. K., Tucci E. R., and Lentink D. (2017) Inspiration for wing design: how forelimb specialization enables active flight in modern vertebrates. *J. R. Soc. Interface* **14**, 20170240, doi: 10.1098/rsif.2017.0240.

Feduccia, A. and Tordoff, H. B. (1979) Feathers of Archaeopteryx: Asymmetric vanes indicate aerodynamic function. *Science* **203**, 1021-1022, doi: 10.1126/science.203.4384.1021.

Festo (2011) SmartBird. www.festo.com/net/SupportPortal/Files/46270/Brosch_SmartBird_en_8s_RZ_110311_lo.pdf, accessed 15 September 2022.

Floreano, D., and Wood, R. J. (2015) Science, technology and the future of small autonomous drones. *Nature* **521**, 460-466, doi: 10.1038/nature14542.

Gatesy, S. M. and Dial, K. P. (1993) Tail muscle activity patterns in walking and flying pigeons (*Columba livia*). *J. Exp. Biol.* **176**, 55–76, doi: 10.1242/jeb.176.1.55.

Gerdes, J., Holness, A., Perez-Rosado, A., Roberts, L., Greisinger, A., Barnett, E., Kempny, J., Lingam, D., Yeh, C. H., Bruck, H. A., and Gupta, S. K. (2014) Robo Raven: A flapping-wing air vehicle with highly compliant and independently controlled wings. *Soft Robot.* **1**, 275-288, doi: 10.1089/soro.2014.0019.

Gillies, J. A., Thomas, A. L. R. and Taylor, G. K. (2011) Soaring and manoeuvring flight of a steppe eagle Aquila nipalensis. *J. Avian Biol.* **42**,.377-386, doi: 10.1111/j.1600-048X.2011.05105.x.

Harvey, C., Gamble, L. L., Bolander, C. R., Hunsaker, D. F., Joo, J. J. and Inman, D. J. (2022) A review of avian-inspired morphing for UAV flight control. *Prog. Aeosp. Sci.* 132, 100825, doi: 10.1016/j.paerosci.2022.100825.

Hörster, W. (1990) Vibrational sensitivity of the wing of the pigeon (*Columba livia*) - a study using heart rate conditioning. *J. Comp. Physiol. A* **167**, 545-549, doi: 10.1007/BF00190825.

Kazim, M., Azar, A. T., Koubaa, A., and Zaidi, A. (2021) Disturbance-Rejection-Based Optimized Robust Adaptive Controllers for UAVs. *IEEE Syst. J.* **15**, 3097-3108, doi: 10.1109/JSYST.2020.3006059.

Kim, D. K., Kang, S. G., Park, J. Y., Sim, J. H., Shin, J. K., Choi, P., and Lee, J. H. (2000) Characteristics of piezoresistive mass flow sensor fabricated by porous silicon micromachining. *Proceedings of 2000 International Microprocesses and Nanotechnology Conference*, 7134-7137, doi: 10.1109/IMNC.2000.872632.

Kim, S., Nam, T., and Park, S. (2004) Measurement of flow direction and velocity using a micromachined flow sensor. *Sens. Actuator A-Phys.* **114**, 312-318, doi: 10.1016/j.sna.2003.12.019.

Klaassen, v. O. B., Choroszucha, R., and Tobalske, B. W. (2020) Passive aeroelastic deflection of avian primary feathers. *Bioinspir. Biomim.* **15**, 056008, doi: 10.1088/1748-3190/ab97fd.

Lee, S.-i., Kim, J., Park, H., Jabłoński, P. G., and Choi, H. (2015) The function of the alula in avian flight. *Sci. Rep.* **5**, 9914, doi: 10.1038/srep09914.

Lentink, D., Müller, U. K., Stamhuis, E. J., de Kat, R., van Gestel, W., Veldhuis, L. L.M., Henningsson, P., Hedenström, A., Videler, J. J., and van Leeuwen, J. L. (2007) How swifts control their glide

performance with morphing wings. *Nature* **446**, 1082-1085, doi: 10.1038/nature05733.

Lindhe Norberg U. M. (2002) Structure, form, and function of flight in engineering and the living world. *J. Morphol.* **252**, 52–81, doi: 10.1002/jmor.10013.

Luca, M. D., Mintchev, S., Heitz, G., Noca, F., and Floreano, D. (2017) Bioinspired morphing wings for extended flight envelope and roll control of small drones. *Interface Focus* **7**, 20160092, doi: 10.1098/rsfs.2016.0092.

Matloff, L. Y., Chang, E., Feo, T. J., Jeffries, L., Stowers, A. K., Thomson, C., and Lentink, D. (2020) How flight feathers stick together to form a continuous morphing wing. *Science* **367**, 293-297, doi: 10.1126/science.aaz3358.

Mohamed, A., Watkins, S., Clothier, R., Abdulrahim, M., Massey, K., and Sabatini, R. (2014) Fixed-wing MAV attitude stability in atmospheric turbulence - Part 2: Investigating biologically-inspired sensors. *Prog. Aeosp. Sci.* **71**, 1-13, doi: 10.1016/j.paerosci.2014.06.002.

Müller W. and Patone G. (1998) Air transmissivity of feathers. *J. Exp. Biol.* **201**, 2591-2599, doi: 10.1242/jeb.201.18.2591.

Necker, R. (1985) Observations on the function of a slowly-adapting mechanoreceptor associated with filoplumes in the feathered skin of pigeons. *J. Comp. Physiol. A* **156**, 391-394, doi: 10.1007/BF00610731.

Parga, J. R., Reeder, M. F., Leveron, T., and Blackburn, K. (2007) Experimental study of a micro air vehicle with a rotatable tail. *J. of Aircr.* **44**, 1761-1768, doi: 10.2514/1.24192.

Reddy, G., Wong-Ng, J., Celani, A., Sejnowski, T. J., and Vergassola, M. (2018) Glider soaring via reinforcement learning in the field. *Nature* **562**, 236-239, doi: 10.1038/s41586-018-0533-0.

Reynolds, K. V., Thomas, A. L. R., and Taylor, G. K. (2014) Wing tucks are a response to atmospheric turbulence in the soaring flight of the steppe eagle *Aquila nipalensis*. *J. R. Soc. Interface* **11**, 20140645, doi:10.1098/rsif.2014.0645.

Rosti, M. E., Kamps, L., Bruecker, C., Omidyeganeh, M., and Pinelli, A. (2017) The PELskin project-part V: towards the control of the flow around aerofoils at high angle of attack using a self-activated deployable flap. *Meccanica* **52**, 1811-1824, doi: 10.1007/s11012-016-0524-x.

Schlüter, J. U. (2009) Lift enhancement at low Reynolds numbers using pop-up feathers. *39th AIAA Fluid Dynamics Conference*, AIAA 2009-4195, doi: 10.2514/6.2009-4195.

Sullivan, T. N., Meyers, M. A., and Arzt, E. (2019) Scaling of bird wings and feathers for efficient flight. *Sci. Adv.* **5**, 1-8, doi: 10.1126/sciadv.aat4269.

Sullivan, T. N., Pissarenko, A., Herrera, S. A., Kisailus, D., Lubarda, V. A., and Meyers, M. A. (2016) A lightweight, biological structure with tailored stiffness: The feather vane. *Acta Biomater.* **41**, 27-39, doi: 10.1016/j.actbio.2016.05.022.

Sullivan, T. N., Wang, B., Espinosa, H. D., and Meyers, M. A. (2017) Extreme lightwight structures: avian feathers and bones. *Mater. Today.* **20**, 377-391, doi: 10.1016/j.mattod.2017.02.004.

Suzuki, S. (2018) Recent researches on innovative drone technologies in robotics field. *Adv. Robot.* **32**, 1008-1022, doi: 10.1080/01691864.2018.1515660.

Takahashi, H., Dung, N. M., Matsumoto, K., and Shimoyama, I. (2012) Differential pressure sensor using a piezoresistive cantilever. *J. Micromech. Microeng.* **22**, 1-6, doi: 10.1088/0960-1317/22/5/055015.

Takahashi, H., Nakai, A., and Shimoyama, I. (2018) Waterproof airflow sensor for seabird bio-logging using a highly sensitive differential pressure sensor and nano-hole array. *Sens. Actuator A-Phys.* **281**, 243-249, doi: 10.1016/j.sna.2018.08.050.

The RoboSwift team (2007) RoboSwift. www.roboswift.nl/, accessed 15 September 2022.

Tobalske, B. W. (2007) Biomechanics of bird flight. *J. Exp. Biol.* **210**, 3135-3146, doi: 10.1242/jeb.000273.

Tucker, V. A. (1987) Gliding birds: The effect of variable wing span. *J. Exp. Biol.* **133**, 33-58, doi: 10.1242/jeb.133.1.33.

Tucker, V. A. (1995) Drag reduction by wing tip slots in a gliding Harris' hawk, *Parabuteo unicinctus*. *J. Exp. Biol.* **198**, 775-781, doi: 10.1242/jeb.198.3.775.

Videler, J. J. (2006) *Avian flight*. Oxford scholarship online, doi: 10.1093/acprof:oso/9780199299928.001.0001.

Videler, J. J., Weihs, D, and Daan, S. (1983) Intermittent gliding in hunting flight of the Kestrel, *Falco tinnunculus* L. *J. exp. Biol.* **102**, 1-12, doi: 10.1242/jeb.102.1.1.

Videler, J. and Groenewold, A. (1991) Field measurements of hanging flight aerodynamics in the kestrel *Falco tinnunculus*. *J. exp. Biol.* **155**, 519-530, doi: 10.1242/jeb.155.1.519.

Watkins, S., Burry, J., Mohamed, A., Marino, M., Prudden, S., Fisher, A., Kloet, N., Jakobi, T., and

Clothier, R. (2020) Ten questions concerning the use of drones in urban environments. *Build. Environ.***167**, 106458, doi: 10.1016/j.buildenv.2019.106458.

Whittow, G. C. (Ed.) (2000) *Sturkie's Avian Physiology*. Academic Press.

Williams H. J., Shepard E. L. C., Holton M. D., Alarcon P. A. E., Wilson R. P., and Lambertucci S. A. (2020) Physical limits of flight performance in the heaviest soaring bird. *Proc. Natl. Acad. Sci. U. S. A.* **117**, 17884-17890, doi: 10.1073/pnas.1907360117.

Xu, X., Zhou, Z., Dudley, R., MacKem, S., Chuong, C. M., Erickson, G. M., and Varricchio, D. J. (2014) An integrative approach to understanding bird origins. *Science* **346**, 1253293, doi: 10.1126/science.1253293.

Yang, W., Wang, L., and Song, B. (2018) Dove: A biomimetic flapping-wing micro air vehicle. *Int. J. Micro Air Veh.* **10**, 70-84, doi: 10.1177/1756829317734837.

Zhu, R., Liu, P., Liu, X. D., Zhang, F. X., and Zhou, Z. Y. (2009) A low-cost flexible hot-film sensor system for flow sensing and its application to aircraft. *Proceedings of the IEEE International Conference on Micro Electro Mechanical Systems*, 527-230, doi: 10.1109/MEMSYS.2009.4805435.

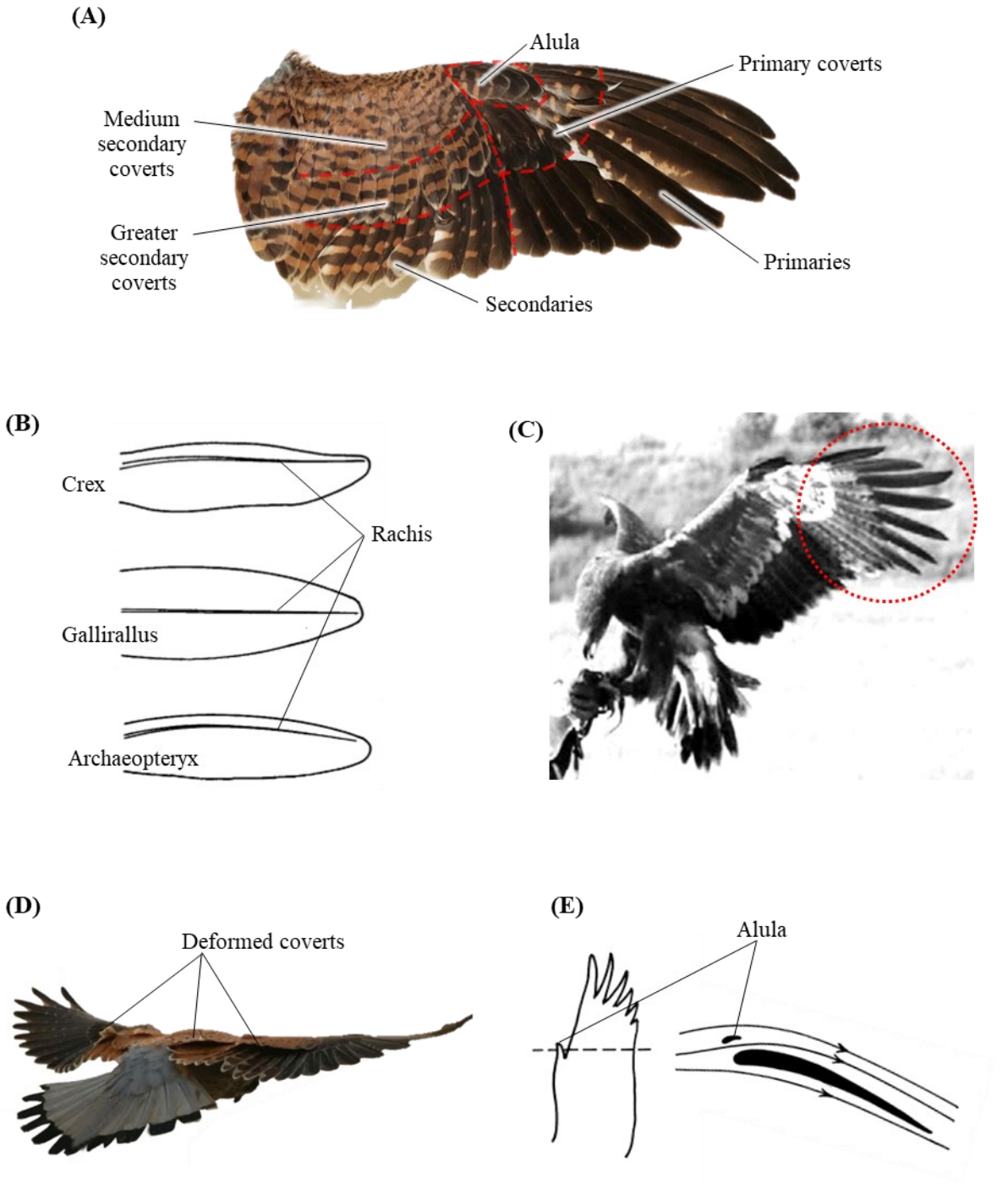

Fig. 1.1 (A) Names of typical avian wing feathers. The picture shows dorsa wing surface of a kestrel. (B) Morphological characteristics of the feather (from Feduccia and Tordoff, 1979). Asymmetric shape in flying species (e. g., Crex and Archaeopteryx) and symmetric shape in terrestrial species (e. g., Gallirallus). (C) Separated primaries of Aquila nipalensis (from Carruthers et al., 2007). (D) Kestrel's wing and deformed coverts in response to oncoming gust (from Mohamed et al., 2014). (E) Hypothesized functions of alula (from Lindhe Norberg, 2002).

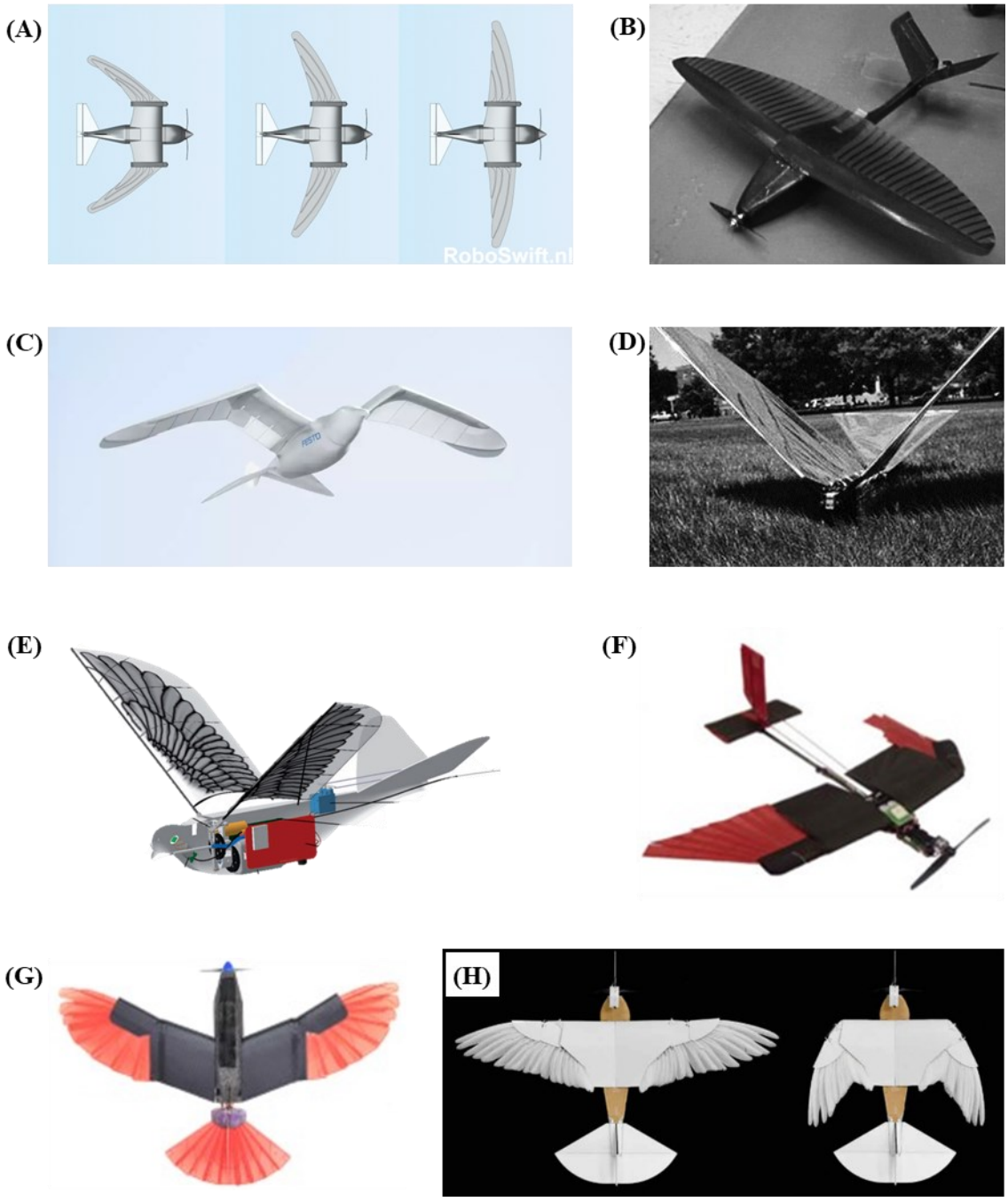

Fig. 1.2 Bird-inspired flying robots. (A) RoboSwift with sweep morphing wing developed by the Roboswift team, 2007. (B) MAV with rotatable tail by Parga et al., 2007. (C) SmartBird with flapping wing by Festo, 2011. (D) Robo Raven with flapping wing and morphing tail by Gerdes et al., 2014. (E) Dove with flapping wing by Yang et al., 2018. (F) Morphing wing MAV by Luca et al., 2017. (G) LisHawk with morphing wing and tail by Ajanic et al., 2020. (H) Soft biohybrid morphing wing MAV by Chang et al., 2020.

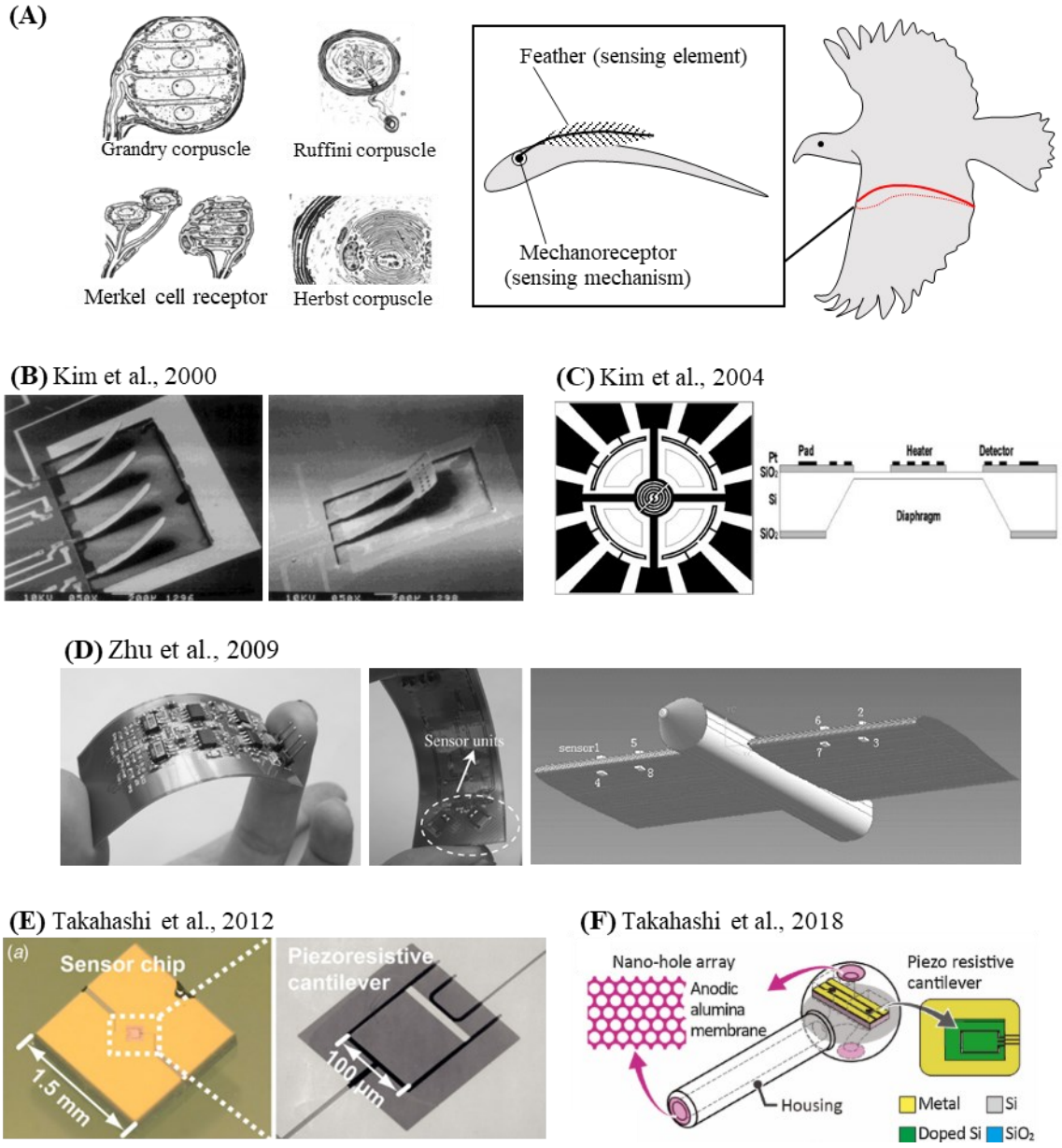

Fig. 1.3 Avian mechanoreceptor that is a bio-sensing elements, and Bio-inspired airflow sensors manufactured by the MEMS technology. (A) Four main types of mechanosensitive sensory corpuscles in birds (left, from Whittow G. C., 2000), and schematic diagram of a mechanoreceptor and feather in a bird wing (right, from Mohamed et al., 2014). (B) Various types of piezoresistive flow sensor with microcantilever structures. (C) A circle-type thermal flow sensor that detects flow direction and velocity (D) A flexible hot-film type airflow sensor for a MAV. (E) A piezo resistive cantilever type differential pressure sensor with high sensitivity to small differential pressure changes. (F) A waterproofed airflow sensor for bio-logging seabirds.

Chapter 2

Flexible flaps inspired by avian feathers for highly robust wing

2.1 Introduction

Drones have been used for various tasks recently (Floreano and Wood, 2015; Liu et al., 2016), it has been increasingly more important to improve their flight performance, such as stability and efficiency, especially when they fly in urban areas. The drones tend to become unstable under the unpredictable wind that is commonly observed in natural environments. The perturbations in the attitude must be fixed as quickly as possible in order to stay airborne even though the disturbances are difficult to predict.

To tackle these problems, engineers have often been inspired by the functions of flying animals in nature (Bechert et al., 2000; Luca et al., 2017; Chin et al., 2017). Birds are frequently selected for the source of inspiration because birds and drones have similar sizes, i.e., Reynolds numbers. It is known that avian wings have various features in their design (Fig. 1A) and flight techniques that make them seem different from aerial vehicles with rigid wings: for example, flexible muscles, feather transmissibility, and flexibility (e.g., Reynolds et al., 2014; Müller and Patone, 1998; Brown and Fedde, 1993).

Previous studies showed that these characteristics contribute to the improvement of bird flight performance. For example, it is known that the separated wing tip slots reduce the induced drag (Tucker, 1995), and that small feather called alula near the leading-edge delays stall at a high angle of attack (Álvarez et al., 2001; Lee et al., 2015). Attentions are also paid to the role of flexible feathers that deform during a flight (Carruthers et al., 2007; Cleaver et al., 2014). Experimental and/or computational studies

on the wings with additional flap inspired by covert feathers have shown that passively pop-up flap enhances the lift force and improve the efficiency.

The studies shown above have been performed mostly under the assumption of uniform flow (Kernstine et al., 2008; Schlüter, 2009; Rosti et al., 2017). Drones are, however, expected to operate at the atmospheric boundary layer where the various unsteady wind is generated due to the friction of the wind and the ground (Watkins et al., 2006). For drones, the improvement of flight stability under the unsteady and unpredictable wind disturbances (e.g., gusts and eddy currents) is as important as improvement of the efficiency.

In this study, aiming at the development of a highly robust wing for drones against disturbances, an experimental wing with covert-inspired flexible flaps near the leading edge of the upper surface was fabricated. With a specific focus on the effect of flexible flaps on the robustness of the wing in disturbance flow, three types of flexible flaps with different stiffnesses were tested by wind tunnel experiments.

2.2 Materials and methods

2.2.1 Design of flexible feathered Wing

The experimental wing model (Fig. 2.1(A)) is inspired and simplified from the avian wing (Fig. 2.1(B)). The wing model is composed of NACA0012 airfoil with an extended trailing-edge plate and flexible flaps. The basic form of the wing was made by cutting the aluminum plate (A5052) with a CNC cutting machine (MDX-540, Roland DG Corporation). The chordwise and spanwise length of the wing were 50 and 100 mm, respectively. After several films with different lengths and widths were tested, rectangular low-density polyethylene films with a length of 20 mm and a width of 5 mm were selected for this study. Eighteen flaps were fixed to the upper surface of the wing by a double-stick tape at 2.5 mm (5% chord) from leading-edge like a cantilever. In this study, three models with flexible flaps with 30, 50, and 80 μm-thickness were tested in this study compared with basic wing without flexible flaps.

2.2.2 Wind tunnel experiment

Experiments were conducted in a low-speed wind tunnel at Chiba University (Ikeda et al., 2018). The test section of the wind tunnel is 2 m-long with a cross-section of 1×1 m. The side walls are made of transparent acrylic boards. In this work, experiments of force measurement and particle image velocimetry were performed at wind speed U = 5 ms^{-1}. In this study, with the wing chord to be a reference for the length scale and the wind speed to be a reference for the velocity scale, Reynolds number is about 16,000.

Aerodynamic force measurement

Fig. 2.2 is a schematic diagram of the setup for the aerodynamic force measurements. As shown in Fig. 2.2(A), the wing assembly was mounted vertically to a six-axes force sensor (Nano17Ti, ATI Industrial Automation) with a 3D-printed sting at the quarter chord. The force sensor was fixed on a rotating stage (SGSP-80YAW, SIGMAKOKI Co., Ltd.), and thus angle of incidence (AoI) of the wing was varied remotely. The rotating stage was operated by a stage controller (SHOT-702, SIGMAKOKI Co., Ltd) with an accuracy of 0.15 °. The aerodynamic forces on the wing were dynamically measured by the force sensor and were digitalized by an A/D converter (USB-6210, National Instruments Corp.) with the sampling rate of 1,000 Hz.

The aerodynamic forces were measured in two experimental conditions: in uniform flow and in disturbed flow. Measurements in uniform flow were performed in the AoI of 0 ° to 20 °(1 ° increments) with a sampling time of 10 seconds. For the experiments in disturbed flow, the disturbance generator was additionally mounted to the wind tunnel at 0.5 m upstream of the wing. The disturbance generator (Fig. 2.2(B)) consists of a motor-driven slider-crank mechanism with a rigid plate made of aluminum. The frequencies of the flow fluctuation were altered by controlling the rotating speed of the motor. In this research, the frequencies of the flow fluctuation are 2 Hz to 25 Hz (1 Hz increments) with a sampling time of 30 seconds at AoI of 5 °. The measured forces at the force sensor were transformed into the lift, L, and drag, D, based on the AoI (Fig. 2.2(C)). Non-dimensional lift and drag coefficients (C_L, C_D) were computed by Eq. (2.1) and (2.2), where ρ is the air density, U is the wind velocity, S is the projected wing area. These aerodynamic forces dynamically changed with time, especially in disturbed flow. Therefore, the robustness of the wing was evaluated by using the standard deviation of the aerodynamic

forces across the sampling time.

$$C_L = 2L/(\rho U^2 S) \tag{2.1}$$

$$C_D = 2L/(\rho U^2 S) \tag{2.2}$$

Particle image velocimetry (PIV)

The PIV measurement system (Fig. 2.3(A)) consists of an Nd:YAG pulsed laser (LDP-100MQG, Lee Laser, Inc.), a timing controller (LC880, SEIKA Digital Image Corporation), a seeding generator (PivPart14, PivTec GmbH), and a high-speed camera (FASTCAM SA3, PHOTRON LIMITED) with an optical lens (150 mm, SIGMA Corporation). The wing assembly was mounted horizontally to sting, unlike the force measurement. A light sheet generated by a pulsed laser via a cylindrical lens was positioned above the wing to illuminate a mid-span streamwise plane, and images were recorded by the camera positioned to the side. The exposure timing of the laser and camera was synchronized through the timing controller. The PIV images were acquired at a rate of 250 pairs per second for a total time of two seconds. The resolution of the image sensor was 1024 × 1024 pixels, and the field of view was about 72 × 72 mm. The PIV images (Fig. 2.3(B)) were analyzed using commercial PIV software (Koncerto II, SEIKA Digital Image Corporation).

The interrogation window size of 24 × 24 pixels with 12 pixels step size was selected to generate a vector field. The lower wing regions which were shadowed by the wing were masked, and thus upper wing regions were used for PIV analysis. In order to evaluate the effect of the flexible flaps on the flow field, the ratio of the area where the vorticity was larger than a threshold (1.0 s^{-1}) was calculated from the vector field. The area defined for comparing the vorticity was inside the fixed region shown by the dashed lines in Fig. 2.3(C). The defined area excludes the vorticity of the wing surface in order to assess only the vortices that are detached from the wing. The raw images of the PIV measurements contained not only the particles but also the illuminated flexible flap. Therefore, the images were also used to measure the deformation of the flexible flap. The trajectory of the tip of the flexible flap was tracked using commercial software (MATLAB, The MathWorks, Inc.).

2.3 Result

2.3.1 Aerodynamic performance

Figs. 2.4(A) and 2.4(B) shows the result for lift and drag coefficients of the wings at each AoI in uniform flow. While the difference in the lift coefficient was small among the models, the model-50 showed a smoother stall behavior than the other models. Additionally, it was found that the coefficient of drag decreases in the models with flexible flaps compared with the basic wing, especially when AoI was greater than 10 °. The standard deviations of lift and drag coefficients (Figs. 2.5(A) and 2.5(B)) were smaller in the models with flexible flaps than in the basic wing at AoI around 6 °. By comparing the frequency spectra of the standard deviation of lift and drag coefficient at AoI of 6 °(Figs. 2.6(A) and 2.6(B)), it was found that the basic wing showed a larger peek at high frequency (around 240 Hz) than the other models with flexible flaps. The force fluctuations in the basic wing are thought to be due to the laminar separation (Kim et al., 2010), which induces the vibration of the trailing-edge plate. It can also be seen that the variation of the model-30 was smaller than the other models at AoI around 15 °.

Fig. 2.7 shows the effect of the flexible flaps on the standard deviation of the lift and drag coefficient divided by those of the basic wing at various disturbance frequencies. These results were obtained after filtering the raw data by a third-order low-pass Butterworth filter with a cut-off frequency of 1.5 times the disturbance frequency in order to reduce the effect of the wing and force sensor resonance (about 36 Hz) contained in the raw data. With reference to the basic wing, the differences of the standard deviation were clearer for the drag coefficient than those for the lift coefficient. The model-80 reduced the standard deviation in the drag about 10 % around the disturbance frequency of 6-9 Hz. Similarly, the comparison of the frequency spectra for a disturbance frequency of 6 Hz (Fig. 2.8) shows that the model-80 reduces the disturbance frequency peak compared with the basic wing, especially in the case of the drag coefficient.

2.3.2 Flow visualization

Fig. 2.9 shows a time-series of the vorticity distribution near the wings in the disturbance of 6 Hz, where the standard deviation of the drag coefficient in the model-80 was reduced in force measurements

(Fig. 2.7(B)). The vortices were separated and moved toward the trailing-edge of the wing for 8-24 milliseconds in Fig. 2.9(A). While the large vortex is generated due to the separation on the basic wing for 12-20 milliseconds in Fig. 2.9(A), the model-80 with the flexible flap generated smaller vortices shedding for 20 milliseconds in Fig. 2.9(D). It was also observed that the flexible flap was deformed in response to the timing of the vortex. The negative pressure of the vortex presumably induced the deformation of the flexible flap.

The time-series of the high vorticity area defined in Fig. 2.3(C) and the tip deflections of the flexible flaps obtained from images are summarized in Figs. 2.10(A) and 2.11(A). The model-80 shows the smaller vorticity than other models with flexible flap and smaller peek than the basic wing at disturbance of 6 Hz (Fig. 2.10(B)). Similar results were obtained at disturbance of 15 Hz (Fig. 2.11(B)), but the differences between the models were relatively smaller than those at 6 Hz. The time-series of the tip deflection of flaps in Figs. 2.10(A) and 2.11(A) reveals that the amount of the deformation of the flexible flap in each model corresponds to its stiffness; the flap deflection is larger in the less stiff model. With the disturbance of 6 Hz, the timing of the maximum deformation of the model 80 was approximately matched with the timing of the maximum vorticity, but the timings of the other models were delayed from the timing of the vorticity peeks. Similarly, the deformation of the flexible flaps was delayed more with the less stiff flaps at a disturbance frequency of 15 Hz.

2.4 Discussion

We found that the variation of the aerodynamic force on the wing in uniform flow can be reduced by attaching the flexible flaps near the leading-edge. It is suggested that the passive deflection of the flexible structure around the leading-edge suppressed the flow separation at the leading-edge, and thus did not induce high-frequency vibration (Figs. 2.5(A) and 2.5(B)). Since the birds' feathers are observed to deflect at a high angle of attack when the flow is thought to be highly unsteady (Carruthers et al., 2007), it is reasonable to assume that the dorsal coverts of birds near the leading-edge have the similar function for the suppression of the flow separation in a uniform flow. This effect is comparable to the function of alula, which delays flow separation by generating longitudinal vortices (Lee et al., 2015),

while the results in this study pointed out that the passive deformation of the feathers can suppress the flow separations.

The flexible flaps on the upper surface of the airfoil enhanced lift in previous studies (e.g., Bechert et al., 2000; Schlüter, 2009; Traub and Jaybush, 2010), but the lift enhancement was not clearly observed in this study (Fig. 2.4(A)). The difference is thought to be because the previous studies placed the flaps near the trailing-edge, while the flexible flaps were attached around the leading-edge in order to see the effect of the coverts in this study. Therefore, the flexible flaps may have multiple roles depending on the locations with respect to the wing chord.

The variation of the aerodynamic forces of the model-80 with flexible flaps are found to be decreased at disturbance frequencies of 6-9 Hz compared with the basic wing without flexible flaps (Fig. 2.7). The force reduction of the other models with flexible flaps was relatively smaller than the model-80, while the tip deflection of the flexible flap was smallest in the model-80 (Fig. 2.10(A)). The reduction of the variations is, therefore, thought to require the appropriate amount of the deformation of the flexible flaps in response to the disturbances. From the flow visualization, we found that the vortex shedding of the model-80 was smaller than that of the basic wing (Fig. 2.9), which is probably because the timing of the deformation of the model-80 flaps matches with the vortex separation (Fig. 2.10). Given that the response of the flaps is completely passive, the mass and the flexibility of the attached flaps should be appropriately designed depending on the disturbance frequency in order to reduce the force fluctuations under disturbances. The hierarchical structure and the taper toward the tip of the bird feathers (Sullivan et al., 2017) may be beneficial in the more complex, natural environments because the complex structures may be able to respond to the disturbances in a wider range of the frequencies.

The application of flexible flaps may not be limited only to the wing for drones. For example, the reduction of aerodynamic force fluctuation is beneficial for the slender vertical structures that are continuously exposed to wind load fluctuation, which leads to mechanical fatigue and damage (Repetto and Solari, 2004). A large number of studies have been devoted to the aerodynamics over a bluff body such as cylinders, and rigid or flexible splitter plate in the wake of bluff bodies are known to control the vortex shedding (e.g., Akili et al., 1999; Shukla et al., 2013). Mazellier et al. (2012) showed that the mean drag force applied on the square cylinder was reduced by feather-inspired porous plates fitted on the sides of the cylinder. As shown in this study, the interaction between the fluid and flexible flaps may

also reduce the fluctuations of aerodynamic forces applied to the bluff bodies. Thus, the adaptive, flexible flaps on the structure surfaces can be suggested as a simple strategy to enhance the maintainability and reliability of structures exposed to various wind disturbances.

References

Akili, H., Sahin, B., and Tumen, N. F. (2005) Suppression of vortex shedding of circular cylinder in shallow water by a splitter plate. *Flow Meas. Instrum.* **16**, 211-219, doi: 10.1016/j.flowmeasinst.2005.04.004.

Álvarez, J. C., Meseguer, J., Meseguer, E., and Pérez, A. (2001) On the role of the alula in the steady flight of birds. *Ardeola* **48**, 161-173.

Bechert, D.W., Bruse, M., Hage, W., and Meyer, R. (2000) Fluid mechanics of biological surfaces and their technological application. *Naturwissenschaften* **87**, 157-171, doi: 10.1007/s001140050696.

Brown, R. E., and Fedde, M. R. (1993). Airflow sensors in the avian wing. *J. Exp. Biol.* **179**, 13-30.

Carruthers, A. C., Thomas, A. L. R., and Taylor, G. K. (2007) Automatic aeroelastic devices in the wings of a steppe eagle Aquila nipalensis. *J. Exp. Biol.* **210**, 4136-4149, doi: 10.1242/jeb.011197.

Chin, D. D., Matloff, L. Y., Stowers, A. K., Tucci, E. R., and Lentink, D. (2017) Inspiration for wing design: how forelimb specialization enables active flight in modern vertebrates. *J. R. Soc. Interface.* **14**, 20170240, doi: 10.1098/rsif.2017.0240.

Cleaver, D. J., Gursul, I., Calderon, D. E., and Wang, Z. (2014) Thrust enhancement due to flexible trailing-edge of plunging foils. *J. Fluids Struct.* **51**, 401-412, doi: 10.1016/j.jfluidstructs.2014.09.006.

Floreano, D., and Wood, R. J. (2015) Science, technology and the future of small autonomous drones. Nature **521**, 460-466, doi: 10.1038/nature14542.

Ikeda, T., Ueda, T., Nakata, T., Noda, R., Tanaka, H., Fujii, T., and Liu, H. (2018) Morphology effects of leading-edge serrations on aerodynamic force production: an integrated study using PIV and force measurements. *J. Bionic Eng.* **15**, 661-672, doi: 10.1007/s42235-018-0054-4.

Kernstine, K. H., Moore, C. J., Cutler, A., and Mittal, R. (2008) Initial characterization of self-activated movable flaps, “pop-up feathers”. *46th AIAA Aerospace Sciences Meeting and Exhibit*, AIAA-2008-

369.

Kim, D.-H., and Chang, J.-W. (2010) Unsteady boundary layer for a piching airfoil at low Reynols numbers. *J. Mech. Sci. Technol.* **24**, 429-440, doi: 10.1007/s12206-009-1105-x.

Lee, S.-I., Kim, J., Park, H., Jabłoński, P. G., and Choi, H. (2015) The function of the alula in avian flight. *Sci Rep.* **5**, 1-5, doi: 10.1038/srep09914.

Liu, H., Ravi, S., Kolomenskiy, D., and Tanaka, H. (2016) Biomechanics and biomimetics in insect-inspired flight systems. *Phil. Trans. R. Soc. B* **371**, doi: 10.1098/rstb.2015.0390.

Luca, M. D., Mintchev, S., Heitz, G., Noca, F., and Floreano, D. (2017) Bioinspired morphing wings for extended flight envelope and roll control of small drones. *Interface Focus* **7**, 20160092, doi: 10.1098/rsfs.2016.0092.

Mazellier, N., Feuvrier, A., and Kourta, A. (2012) Biomimetic bluff body drag reduction by self-adaptive porous flaps. *C. R. Mecanique* **304**, 81-94, doi: 10.1016/j.crme.2011.11.006.

Müller, W. and Patone G. (1998) Air transmissivity of feathers. *J. Exp. Biol.* **201**, 2591-2599, doi: 10.1242/jeb.201.18.2591.

Repetto, M. P. and Solari, G. (2004) Directional wind-induced fatigue of slender vertical structures. *J. Struct. Eng.* **130**, 1032-1040, doi: 10.1061/(ASCE)0733-9445(2004)130:7(1032).

Reynolds, K. V., Thomas, A. L.R., and Taylor, G. K. (2014) Wing tucks are a response to atmospheric turbulence in the soaring flight of the steppe eagle *Aquila nipalensis*. *J. R. Soc. Interface* **11**, 20140645, doi: 10.1098/rsif.2014.0645.

Rosti, M. E., Kamps, L., Bruecker, C., Omidyeganeh, M., and Pinelli, A. (2017) The PELskin project-part V: towards the control of the flow around aerofoils at high angle of attack using a self-activated deployable flap. *Meccanica* **52**, 1811-1824, doi: 10.1007/s11012-016-0524-x.

Schlüter, J. U. (2009) Lift enhancement at low Reynolds numbers using pop-up feathers. *39th AIAA Fluid Dynamics Conference*, AIAA-2009-4195, doi: 10.2514/6.2009-4195.

Shukla, S., Govardhan, R. N., and Arakeri, J. H. (2013) Dynamics of a flexible splitter plate in the wake of a circular cylinder. *J. Fluids Struct.* **41**, 127-134, doi: 10.1016/j.jfluidstructs.2013.03.002.

Sullivan, T. N., Wang, B., Espinosa, H. D., and Meyers, M. A. (2017) Extreme lightwight structures: avian feathers and bones. *Mater. Today* **20**, 377-391, doi: 10.1016/j.mattod.2017.02.004.

Traub, L. W., and Jaybush, L. (2010) Experimental investigation of separation control using upper-

surface spoilers. *J. Aircr.* **47**, 714-717, doi: 10.2514/1.45434.

Tucker V. A. (1995) Drag reduction by wing tip slots in a gliding Harris' hawk, *Parabuteo unicinctus*. *J. Exp. Biol.* **198**, 775-781.

Watkins, S., Milbank, J., Loxton, B. J., and Melbourne, W. H. (2006) Atmospheric winds and their implications for microair vehicles. *AIAA j.* **44**, 2591-2600, doi: 10.2514/1.22670.

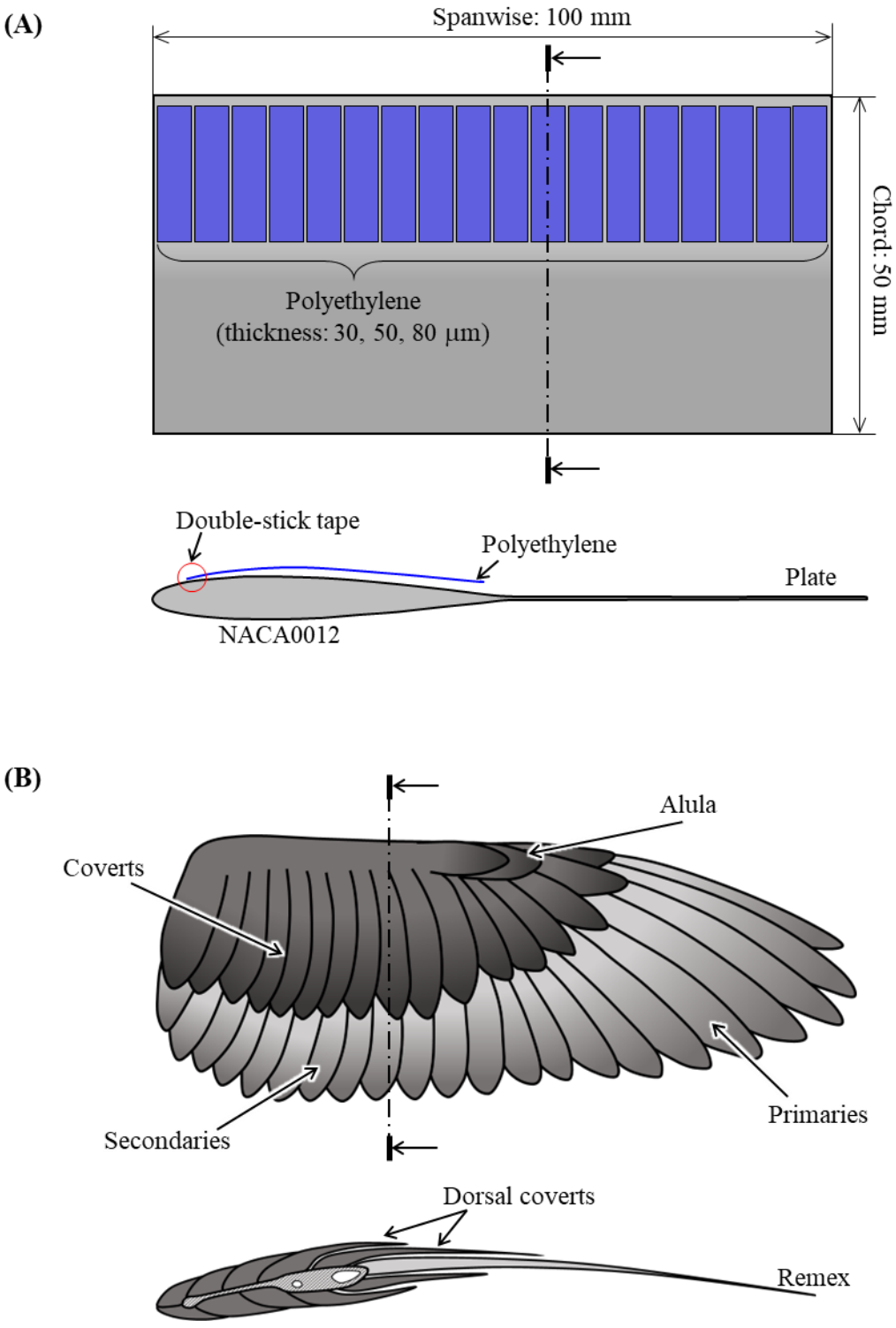

Fig. 2.1 Schematic diagram of (A) the bird-inspired wing model and (B) a bird wing and its cross-section.

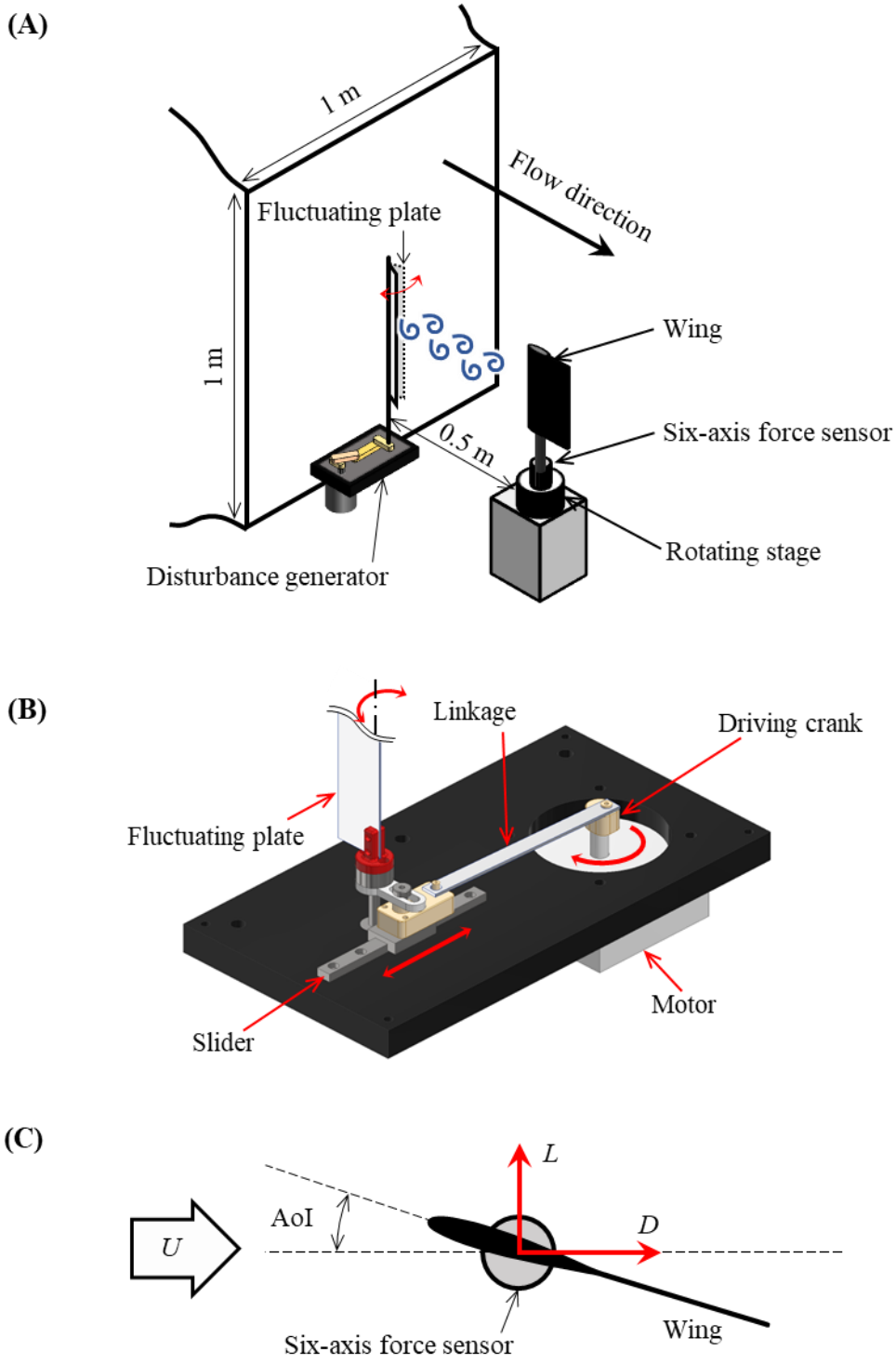

Fig. 2.2 (A) Experimental setup for aerodynamic force measurements in the low-speed wind tunnel. The fluctuation generator was mounted upstream for measurements in disturbed flow. (B) The fluctuation plate was driven by a motor via a slider-crank mechanism. (C) Lift, *L*, and Drag, *D*, were measured by the six-axis force sensor.

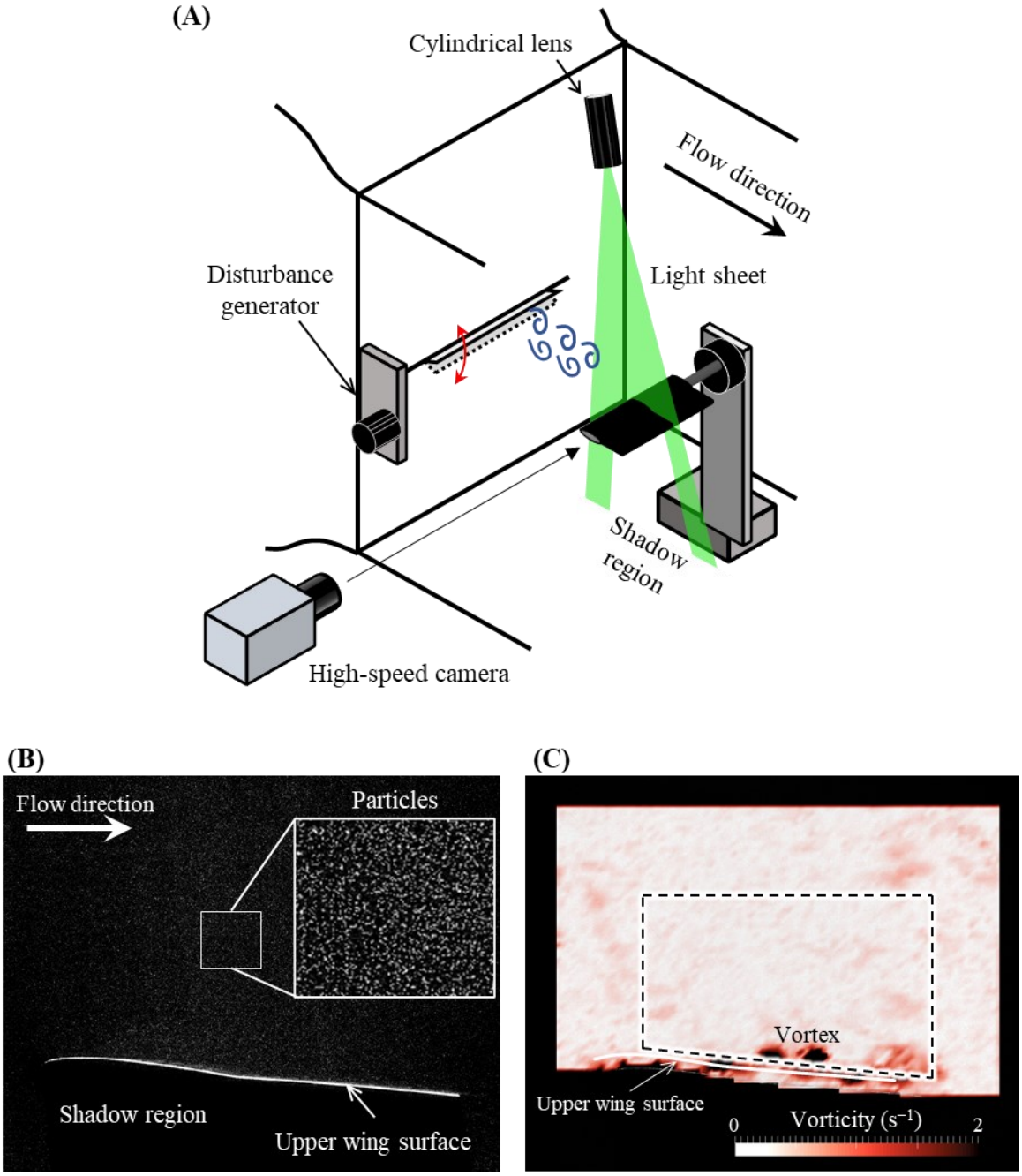

Fig. 2.3 (A) Schematic diagram of the experimental setup for 2D-PIV measurements. (B) A raw image of PIV measurements. Since the laser light was irradiated from above of the wing, the area lower than the wing was in the shadows and too dark to see the particles. (C) The sample flow field is visualized by the distribution of the vorticity. The surrounding area in black was masked during the analysis of the PIV due to the low light level. The area inside the dashed line was defined to calculate the ratio of high vorticity area.

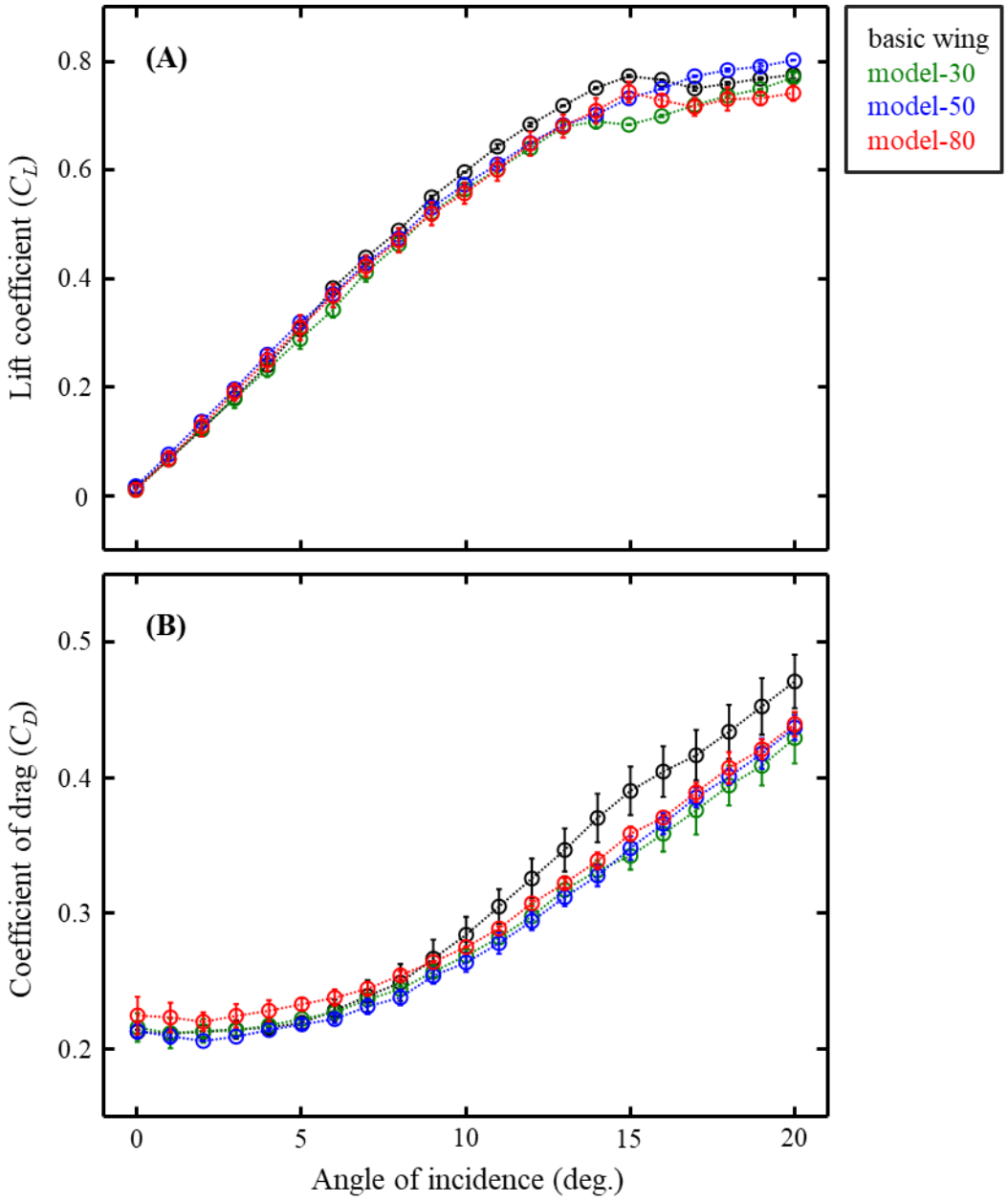

Fig. 2.4 Coefficients of aerodynamic forces with change in angle of incidence. Time-averaged (A) lift coefficient (C_L) and (B) drag coefficient (C_D).

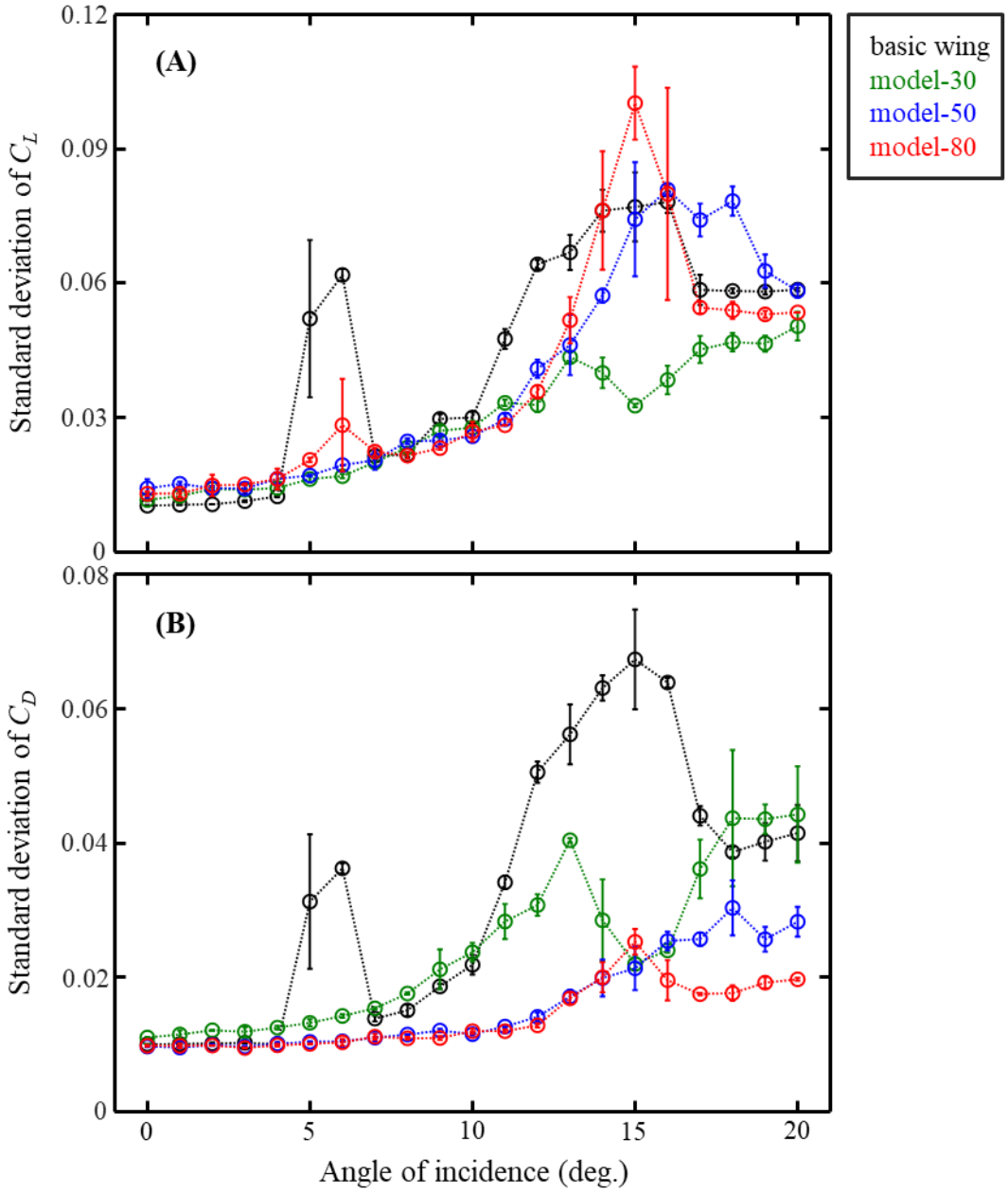

Fig. 2.5 The standard deviations of (A) lift and (B) drag coefficients.

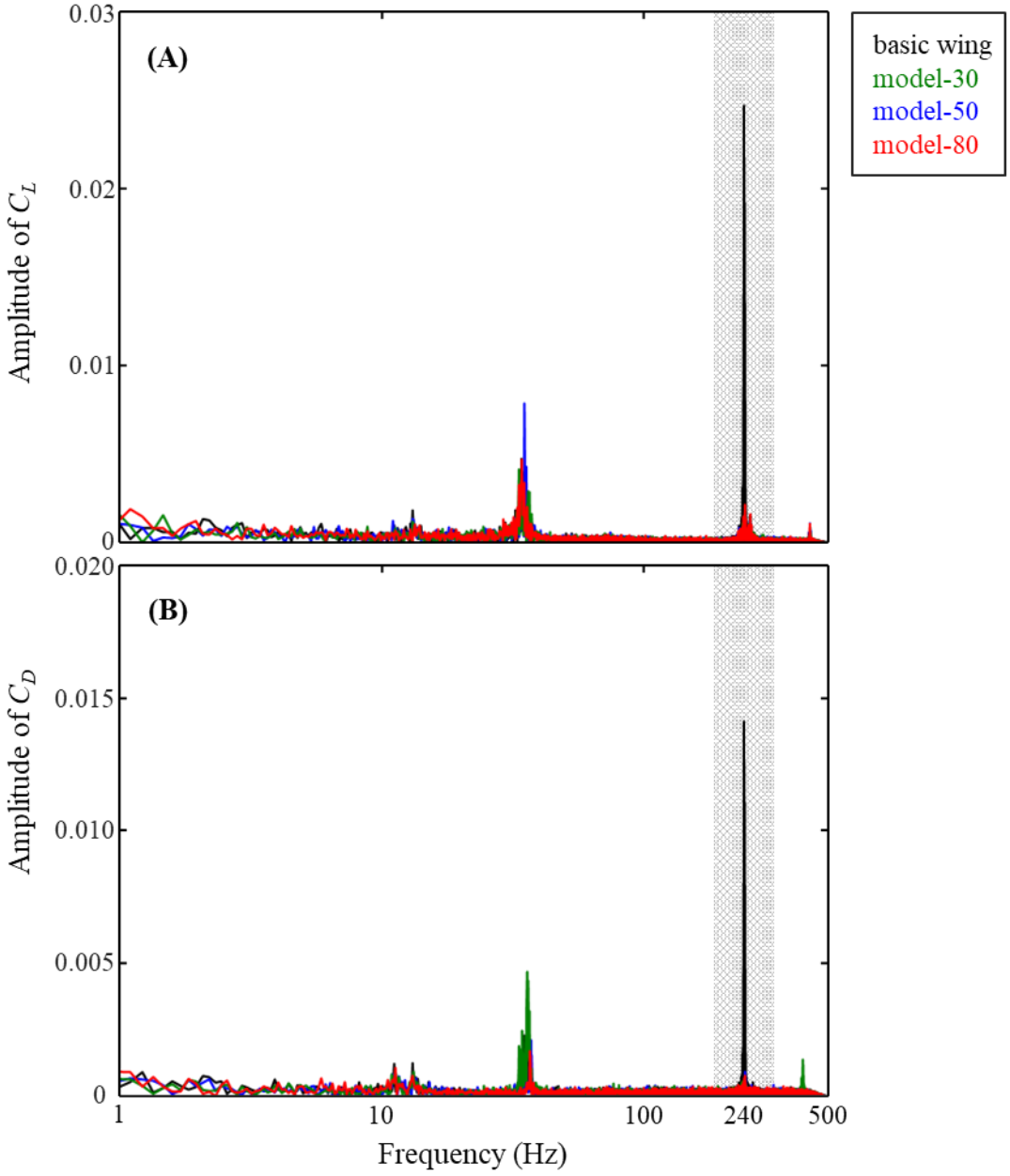

Fig. 2.6 The frequency spectra of (A) lift and (B) drag coefficients at an angle of incidence of 6 °.

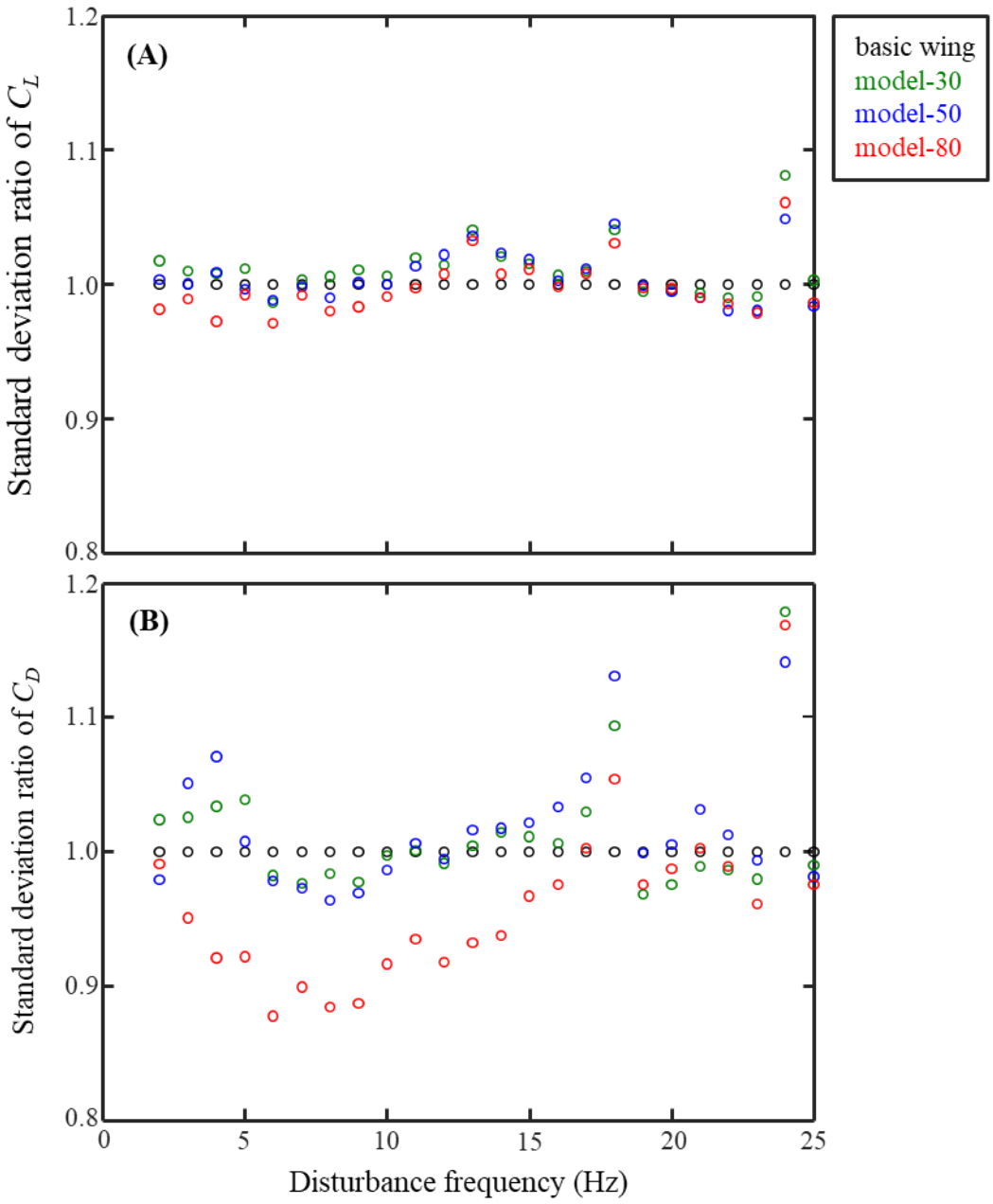

Fig. 2.7 Effect of the disturbance frequencies on the standard deviation ratio of (A) lift coefficient and (B) drag coefficient relative to the basic wing at an angle of incidence of 5 °.

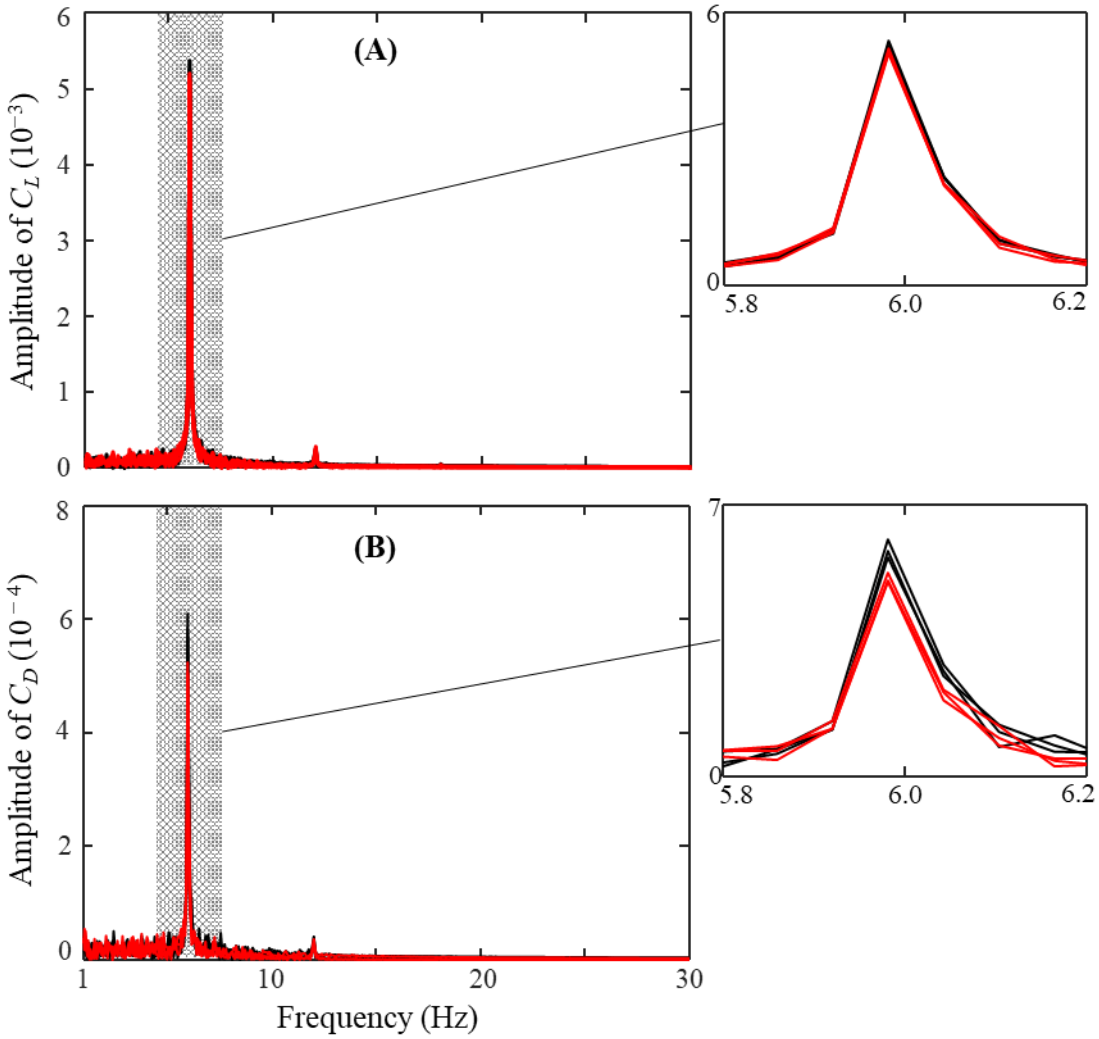

Fig. 2.8 Frequency spectra of (A) lift and (B) drag coefficient at disturbance frequency of 6 Hz.

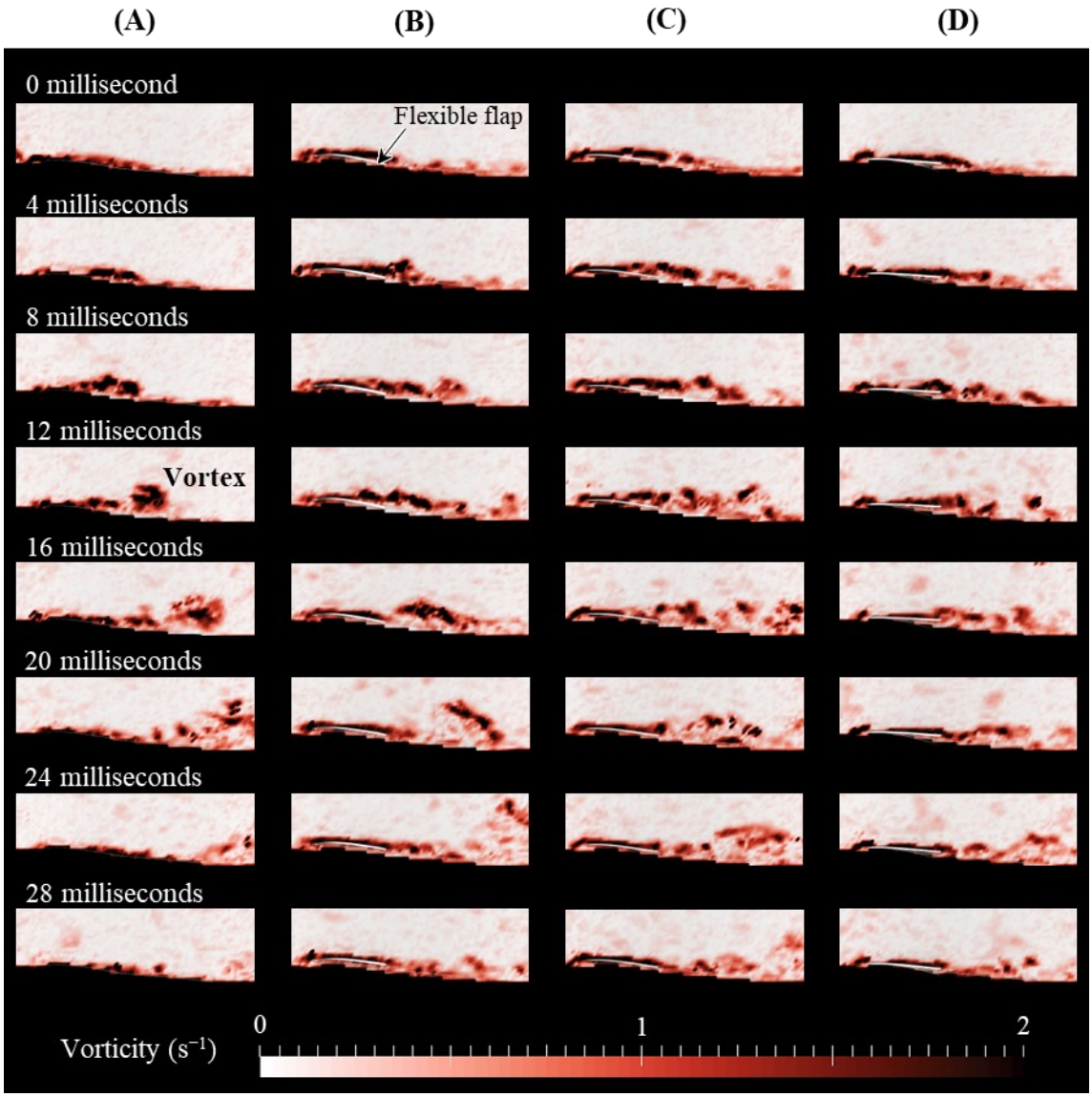

Fig. 2.9 Time-series of the vorticity field within 28 milliseconds around (A) basic wing, (B) model-30, (C) model-50, and (D) model-80 at disturbance frequency of 6 Hz. The ratio of high vorticity area is minimized when t = 0 milliseconds in each model.

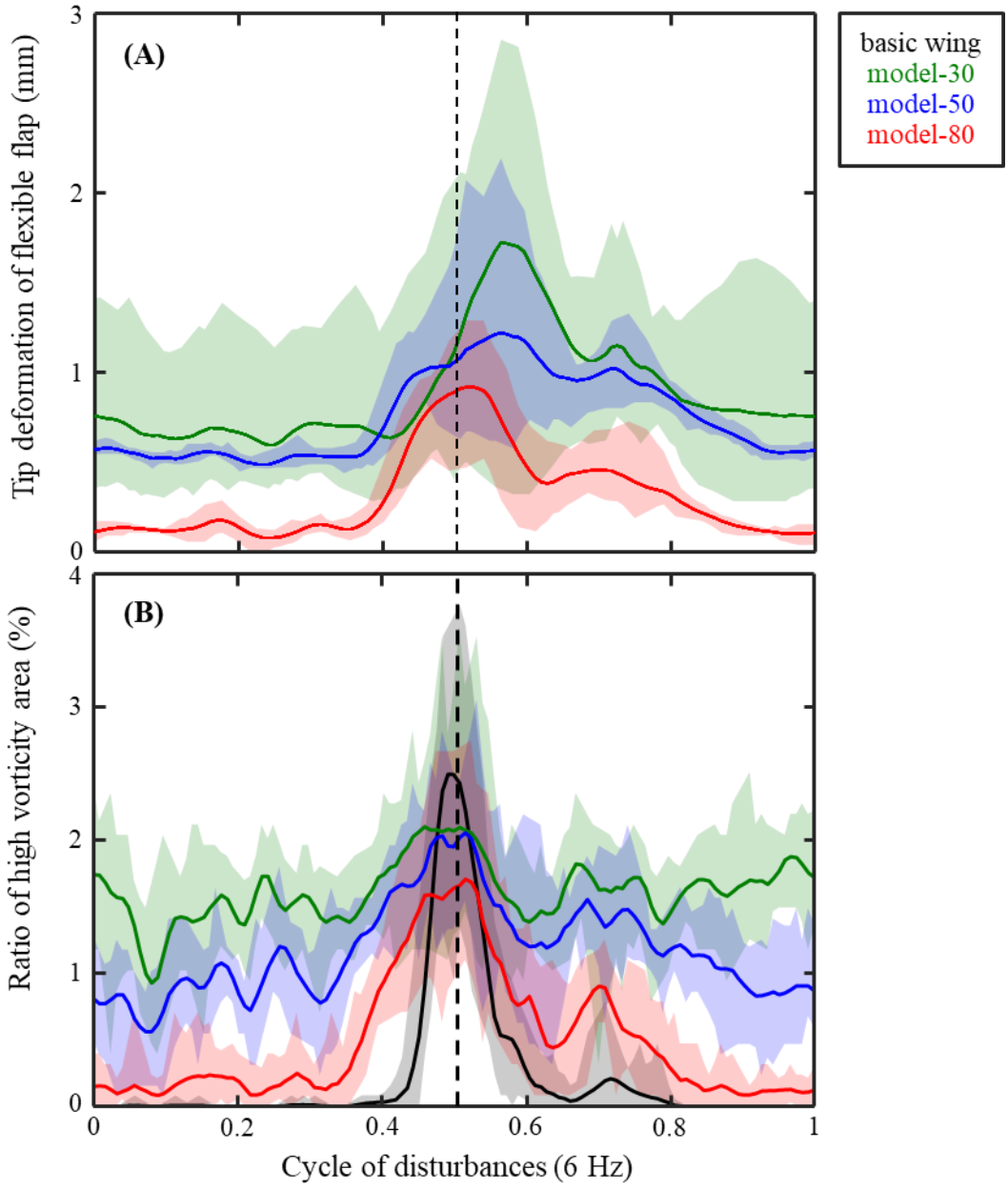

Fig. 2.10 Time-series of (A) the deflection of the tip of flexible flaps and (B) the ratio of high vorticity area in the disturbance of 6 Hz.

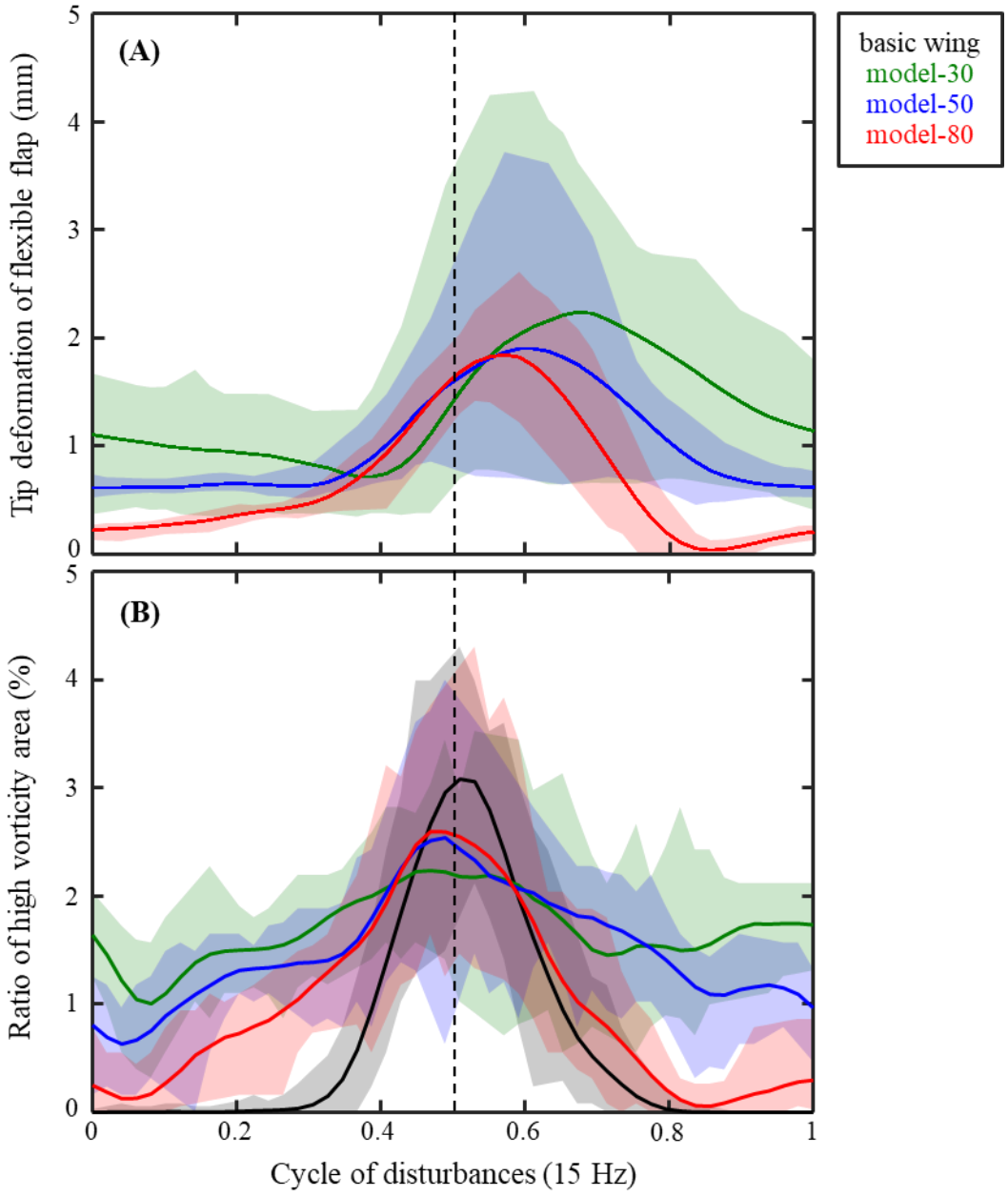

Fig. 2.11 Time-series of (A) the deflection of the tip of flexible flaps and (B) the ratio of high vorticity area in the disturbance of 15 Hz.

Chapter 3

An airflow sensor inspired by avian flexible feathers

3.1 Introduction

Flying animals and drones are exposed to the ever-changing winds that change moment by moment in nature. The wind fluctuations are caused by atmospheric boundary layer (ABL). In the ABL, wind gusts and other phenomena can affect the flight stability of drones negatively (Watkins et al., 2020), causing them to crash in the worst cases. On the other hand, it is interesting to see how flying animals are able to adapt to their surrounding environments and thrive under the unpredictable influence of wind. For example, it was reported that the common kestrel (*Falco tinnunculus*) can keep the fluctuation of its center of gravity very slight while hovering in the wind (Videler et al., 1983). This suggests that birds have the skill to control their behavior in response to the wind environments. In order to enable flying robots to engage in a wider variety of tasks, further improvements are required to ensure stable flight under the influence of the ABL.

Birds flight with outstanding performance in variable wind environment could be the sources that provide ideas to enhance the performance of artificial fliers such as drones. In fact, engineers and scientists were inspired the great interests by flying animals that are thought to have acquired optimized bodies and features for flight to survive through long-term evolution (Chin et al., 2017; Sullivan et al., 2017; Xu et al., 2014). It has been studied that the complex and ingeniously designed bodies and wings of birds have functions that contribute to aerodynamic performance and support the bird's superior flight. Morphing , a unique wing morphology change of birds, helps them to actively control aerodynamic

forces during flight. In addition to active morphing, it has been suggested that bird's bodies and wings also have passive mechanisms that assist them in maintaining stable flight. For example, it has revealed that the deflection of flexible feathers such as the primaries, alula, and coverts due to wind can provide beneficial effects on aerodynamic performance (Carruthers et al., 2007; Klaassen et al., 2020; Lee et al., 2015; Tucker, 1995; Fig. 3.1(A)). Other studies have suggested that the flight muscles on the bird's shoulders like hinges act like the suspension of a vehicle to dampen the effects of gusts of wind (Cheney et al., 2020; Reynolds et al., 2014).

Avian wings, with various remarkable functions, are composed of a musculature and a large number of feathers forming smooth wing surface: the feathers are thought to be useful in detecting flow fluctuations through the flexible deformation, as well as maintaining their body temperature and external display. From a microscopic level, sensory organs are known to present on the body surface of flying animals, not only birds but also insects and bats (Chin et al., 2017). Birds have rich sensory organs called mechanoreceptors in their bodies and seem to sense environmental parameters such as flow and pressure through the mechanoreceptors (Brown and Fedde, 1993). Previous research has shown that removing the microscopic hairs on the membranous wings of bats can influence their flight (Sterbing-D'Angelo et al., 2011). Flying animals may effectively use the function of sensing flow near their bodies via their mechanoreceptors to enable highly stable flight.

The capability of flying animals to detect wind variations on their body surfaces is one of their distinctive features compared to artificial flyers. It has been suggested that flying animals seem to utilize atmospheric information obtained from mechanoreceptors for flight control. On the other hand, control of flying robots has been attempted by using various sensors, such as inertial measurement unit (IMU), global positioning system (GPS), and laser imaging detection and ranging (LiDAR). Multi-rotor drones have developed along with the improvement in flight controllers that use the information driven from these sensors. Therefore, an approach of utilizing atmospheric information for flight control, as in the case of flying animals, have been underdeveloped in flying robots.

To aim at applying to the small flying robots, various sensors have been developed in order to detect the flow variation. Since it is difficult to completely mimic biological structures such as mechanoreceptors, several bioinspired sensors have been devised that focus on specific functions. For example, micro sensors have been developed based on MEMS technology, which detect the flow or

differential pressure (e.g., Kim et al., 2004; Takahashi et al., 2012). Actually, some approaches to acquire airflow information by installing such small sensors on a MAVs have been proposed. (e.g., Mohamed et al., 2014; Zhu et al., 2009). Actually, it is expected that controlling artificial flyers can be improved by the function of detecting airflow. For example, airflow information gained by pressure sensors and strain gauges in fixed-wing airframes suggests that sensing local state of airflow and aerodynamic forces can be useful for flight control (Araujo-Estrad et al., 2017). On the other hand, even though the aerodynamic effectiveness of artificial feather deflection has been pointed out, there are few studies on the detection of airflow using feather-based flexible structures. Furthermore, it is unclear what information can be encoded by the deformation of the feather-like structures in a dynamic situation. Therefore, it is necessary to investigate the role of deformation by flexible structures based on feathers in acquiring information about the variable airflow.

In this study, aiming at exploring the possibility of applying the sensor to a small flying robot, two types of airflow sensors with flexible structures inspired by avian feather were fabricated and their characteristics of aerodynamics and sensing were investigated by wind tunnel experiments. Instead of perfectly replicating the bird's feathers and mechanoreceptors, fabrications of flexible sensors with simpler mechanisms that have sensing function were tried inspired by the covert feathers (Fig. 3.1(B)). A simplified wing modeled on the common kestrel was also fabricated for wind tunnel experiments. Two types of sensors were taped on the upper surface of the wing and tested. In this study, we report the response characteristics and aerodynamic performance of a feather-based sensor that detects changes in airflow. Then, discussions are given toward the development into a flying robot with high robustness against wind disturbances.

3.2 Stain-gauge-type airflow sensor

3.2.1 Material and method

Design and fabrication of the model

Feather-based airflow sensors of strain-gauge type were made of polyethylene terephthalate (PET) sheets on which silver nano-ink can be printed. Silver nano-ink (NBSIJ-MU01 , Mitsubishi Paper Mills Ltd.) loaded in a commercial inkjet printer (PX-S160T, Seiko Epson Corp.) was printed on a PET sheet coated with a specific chemical that reacts with the silver nano-ink to form a conductive layer (NB-TP-3GU100, Mitsubishi Paper Mills Ltd.). The circuit shown in the Fig. 3.2(A) was printed by using the method with silver nano-ink printing. The printed circuit was designed to mimic a typical quarter-bridge circuit for measuring a strain gage sensor (Fig. 3.2(B)). This sensor (Fig. 3.2(A)) was composed of four resistances and one of them functioned cantilever for a sensing element. The other resistor elements (R_2, R_3, and R_4) were printed to be the same resistance value of R_1 as much as possible, by adjusting the circuit length. With constant voltage (V_{in}) applied to this circuit, changes in the resistance value of R_1 produces differences in output voltage (V_{out}), allowing the deformation of the sensor to be acquired as electrical signals. The output voltage was calculated by the following equation.

$$V_{out} = \frac{(R_1+\Delta R)\cdot R_3 - R_2\cdot R_4}{(R_1+\Delta R+R_2)\cdot(R_3+R_4)}\cdot V_{in} \tag{3.1}$$

This hand-made strain-gauge-type sensor circuit was printed on one side of PET film. Thus, it was expected that the changes in resistance would depend on the direction of sensor bending (Fig. 3.3(A)). The base of the sensor was fixed, and the tip of the sensor was lifted up to bend it (Fig. 3.3(B)). Bending tests were performed in stretching and shrinking sides of the sensor. Fig. 3.3(C) showed that differences in output voltage dur to the differences in bending direction between stretching and shrinking. It was confirmed that output voltage increased when the stain gauge was bent in the stretching direction and decreased when it was bent in the direction of shrinking. Tests were performed three times (n3) in each side, and it was also found that the measured output voltage showed larger variations when the strain

gage was stretched. This was probably due to a minute irregularity in the silver nano-ink circuit as it was being stretched. For better measurement reproducibility, it was decided that the surface on which the circuit was printed faced up when this hand-made strain-gauge-type airflow sensor was tested in a wind tunnel.

A wing model was fabricated to equip the airflow sensor, aiming at the development of a bird-inspired robot for the final objective. Referring to the common kestrel (*Falco tinnunculus*), the wing model was designed to generate lift force in order to support a weight of 100 g with single wing of 250 mm half span. The details of the wing model are described again in following Section 4.2 of Chapter 4.

Wind tunnel experiment

Experiments were conducted in order to evaluate the strain-gauge-type airflow sensor in a wind tunnel at Chiba University (Ikeda et al., 2018), as shown in Fig. 3.4(A). The wind tunnel has a test volume of 1.0 × 1.0 × 2.0 m. The sensor was taped onto the proximal side of the wing, approximately 60% chord length from the leading edge. Measurements were conducted in a uniform flow of 8 ms^{-1} and 10 ms^{-1}.

In the experiments, the constant voltage (V_{in}) applied to the sensor circuit was set to 5 V. Sensor's output voltages and deformation were measured synchronously (Fig. 3.4(B)). Analog voltage data from the sensor were acquired synchronously through an A/D converter (NI-9205, National Instruments Corp.) at a sampling rate of 250 Hz. Shooting speed of the high-speed camera (Mini AX50, PHOTRON LIMITED) was set to 250 fps. Since time resolution of 50 fps was enough to actually track the deformation of the sensor, the tracking results in Subsection 3.2.2 were tracked at 50 fps.

3.2.2 Result

It was confirmed that the strain-gauge-type sensor can output electrical signals in response to its deformation at high angle of incidence of the wing. However, the signal included a lot of noise (Fig. 3.5(A)), thus post-processing to remove outliers was applied (Fig. 3.5(B)). Post-processed sensor's voltage signal was compared to the deformation data tracked by high-speed camera images (Fig. 3.5(C)). The voltage value decreases as the sensor deforms in upward direction (Fig. 3.3), thus the voltage signal was vertically reversed and overlapped with the image tracking results (Fig. 3.5(D)). This comparison

showed that the peak positions of both data coincide, indicating that the strain-gauge-type sensor can capture the deformation by wind as a change in the voltage signal.

Although the measurements of sensor response were performed at various angles of attack of the wing, the coincidence between the deformation data and voltage signals as shown in Fig. 3.5(D) could not be confirmed at lower angles of attack. In other words, current design of the strain-gauge-type sensor may have limited the capability of acquiring the sensor deformation as a voltage signal to the higher angles of attack over 30 °.

On the other hand, a simple experiment was conducted to observe the output voltage behavior of this sensor made of a flexible PET sheet when it is vibrated. When the free-tip of the sensor was vibrated by flicking it with a finger, the voltage signal changed according to the strength of the flicking (Figs. 3.6(A) and 3.6(B)). However, when the sensor was strongly flicked, the residuals were about 10 mV higher than the initial voltage values even after the vibration had been attenuated (Fig. 3.6(B)).

3.2.3 Discussion

Strain-gauge-type sensor was fabricated and evaluated its applicability for airflow sensing. Wind tunnel experiments have revealed that the strain-gauge-type sensor performs airflow sensing function under certain conditions, but also that there are difficulties in the practicality of the sensor.

Two hypotheses can be considered as reasons for the strain-gauge-type sensor being significantly affected by noise as seen in Fig. 3.5(A). First, the experiment was performed in a setup without temperature compensation, and the wind directly blowing on the sensor with silver nano-ink circuit could have been a disturbance to the resistance change of the circuit. Second, the degradation of silver nano-ink due to the time passage may have caused an irregularity in the sensor's circuit. It is known that the resistance of silver nano-ink changes along with the passage of time due to the effects of oxidation and light. As a solution, it is preferable to mold the circuit surface with a protective layer, but this countermeasure was not suitable for the fabrication of the airflow sensor which is the more flexible the better.

There were other difficulties in the practicality of this strain-gauge-type sensor. One is that the sensor value drifts as shown in Fig. 3.6(B). After the sensor was significantly deformed, the residual strain could cause the resistance value of the circuit to change from the initial value. This phenomenon was

undesirable for the purpose of collecting reproducible sensor information. Second, in order to configure a quarter-bridge circuit, dummy parts with the same resistance values as that of the cantilever-type sensor part must be printed, making it difficult to save the area of a single sensor. This problem is a disadvantage when multiple sensors are to be placed on the wing surface. Third, the voltage signal output from the sensor was faint. As shown in Eq. 3.1, the sensor output voltage is proportional to the V_{in}, but a large V_{in} causes resistance heating in the circuit. Too much resistance heating causes thermal deformation of the PET sheet, which limits the sensor's capability to increase the output signal by increasing $V_{in.}$

The strain-gauge-type sensor fabricated in this section presented practical difficulties due to its mechanical and electrical characteristics, but at the same time, it also showed the advantage of the flexible PET sheet with electrical circuits of any shape. The simple method in which the sensor element can be fabricated using only a PET sheet printed with a silver nano-ink circuit could be an advantage over the other type developed in the following Section 3.3. For example, it can be useful when the main objective is not to measure reproducible quantitative values but to collect information on vibrations such as those shown in Fig. 3.6.

3.3 Hall-effect-type airflow sensor

3.3.1 Material and method

Design and fabrication of the model

Hall-effect-type airflow sensors of hall-effect type were made of two primary materials: PET sheets on which silver nano-ink can be printed (same as described in Subsection 3.2.1) and unipolar linear hall-effect magnetic sensors (DRV5056A3, Texas Instruments Inc.), as shown in Fig. 3.7(A). Neodymium magnets with a diameter of 5 mm and a thickness of 1 mm (ND0051, Magfine Corp.) were also included in the sensor configuration. The relatively heavier magnets were buried inside the hollow wing (i.e., under the PP wing surface), while the lightweight hall-effect sensors were attached with conductive paste to the PET sheets, which raise up under the influence of wind (Fig. 3.7(B)). Signals from the hall-

effect sensors were recorded by an A/D converter through a conductive circuit printed on the PET sheets and cables. Seven sensors, named Sens1 to Sens7, were taped on the upper surface of the wing at equal intervals along the span direction (Fig. 3.8(A)). Sen1 was at wing tip side and smaller in size, and Sens7 was at wing root side and relatively larger in size. Dimensions of each sensor are shown in Table 3.1. The front edge of the sensors was taped to the 25% chord position of the wing so that the rear edge of the sensors aligned with the trailing edge of the wing. They output high voltage (5 V) when they are close to the wing surface (i.e., the distance between the hall-effect sensors and the magnets is minimal). Conversely, the output voltage of sensors drops as the sensors are lifted by the wind and far from magnets. In the following results, the sensors' behavior described above corresponds to the graphs showing the response of hall-effect-type flexible sensors.

Wind tunnel experiments

Aerodynamic performance of the wing and the response of the sensors were studied in a static and dynamic variation of the angle of incidence in a wind tunnel at Chiba University (Ikeda et al., 2018). The wind tunnel has a test volume of 1.0 × 1.0 × 2.0 m. The angle of incidence of the wing was changed by the servo motor (SG-90, Umemoto LLC) from 0 ° to 20 ° with a driving controller (Arduino Uno). In order to measure the aerodynamic forces, we set the wing and servo motor on the six-axis force sensor (PFS020YA500G6, Leptrino Inc.). Servo motor and force balance were covered by a windbreak shaped a NACA airfoil (Fig. 3.8(B)). Analog data from the force balance and feather-based sensors were acquired synchronously through an A/D converter (NI-9205, National Instruments Corp.) at a sampling rate of 1,000 Hz.

Measurements of the aerodynamic force and the sensors' responses were conducted in a uniform flow of 8 ms^{-1} and 10 ms^{-1}. In this study, the wind speed conditions were determined based on the assumption that the sensors would be applied to a bird-size flying robot in the future study. The angle of incidence of the wing was varied from 0 ° to 20 ° in 2 ° increments. Measurements were taken three times for experimental models with and without sensors, respectively.

As the static test, measurements were taken for 10 seconds at each angle of incidence with wind speeds of 8 ms^{-1} and 10 ms^{-1}. The wing was set horizontally in a no-wind condition. However, since the dihedral angle increases as the wind speed increases, the lift force was calculated by appropriately

calculating the force component acquired by the force balance. Measurement of the flow near the upper surface of plane wing with hot-wire anemometer (Smart CTA 7250, Kanomax Japan Inc.) was conducted to investigate fluid oscillations below the stall angle. Measurements were performed with the hot-wire probe fixed a few millimeters from the wing surface at six points; 25 % and 60 % chord length form leading edge at wing-tip side, mid-span, and wing-root side (Fig. 3.8(C)).

In the dynamic test, the wing was set as the same as in the static test. The angle of incidence of the wing was tested from 0 ° to 20 ° at two different actuation speeds of the servo motor. A faster pitch-up condition of 20 ° per second and a slower one of 10 ° per second were tested with wind speeds of 8 ms^{-1} and 10 ms^{-1}. Thus, in faster motion, the angle changes from 0 ° to 20 ° in about 1.5 seconds, and in slower motion, it changes in about 3 seconds. It is confirmed that the influence of the inertial changes caused by the servo motor actuating on the flexible sensor and force sensor was slight.

3.3.2 Result

Static measurements test

It was confirmed that the hall-effect-type airflow sensors were passively deformed by wind, just as it is known in previous studies that avian feathers or feather-based flexible flaps float under the influence of wind (Bechert et al., 2000; Carruthers et al., 2007; Rosti et al., 2017). Interestingly, it was also found that each hall-effect-type sensor distributed in the spanwise direction responded differently according to the change in the angle of incidence of the wing (Figs. 3.9). Each plot represents the average value measured for 10 s, and the error bars indicate the standard deviation of the average values measured three times. The black plots are lift curves measured together, which show a stall at the angle of incidence around 10 °. It should be noted that the average values for Sens1 differ significantly from those of the other sensors, but this is due to the installation problem that the distance between the hall-effect sensor and the magnet is always a certain distance away from each other. Therefore, it is not meaningful to compare the average values of Sens1 and other sensors relatively. Sens1, 2, 4, and 6 gradually began to show changes in responses when the angle of incidence is 6 ° to 8 °, earlier than when the angle reaches 10 ° where the stall occurs. Over the stall angle, each sensor lifted and vibrated more, with correspondingly larger changes in the mean values.

Standard deviations of the sensor values are given in the Fig. 3.10 since the sensors were fluttering during the measurement. In each wind speed, the sensors on the mid-span of the wing were relatively oscillating at the low angle of attack before the stall. Sensor fluttering, which was observed even at low angles of attack, is thought to be induced by the subtle flow oscillations on the upper surfaces of the wing measured by hot-wire anemometer (Fig. 3.11). All of the sensors were observed to oscillate over the stall angle, but the Sens7 sensor exhibited relatively small oscillations. This could have been due to the larger size of Sens7 than the others or to wing tip effects on the wing-root side.

Compared to wings without the sensors, wings with sensors showed improvements in aerodynamic performance (Figs. 3.12 and 3.13). Experiments were conducted in wind speeds of 8 ms^{-1} and 10 ms^{-1}, resulting in the Reynolds numbers based on the mean chord length are about 53,000 and 66,000, respectively. A slight increase in the maximum lift coefficient was observed (Fig. 3.12(A)). There was also a difference in how the lift coefficient curves changed, showing that the wing with the sensor had a gentler drop in lift over the stall angle. The curves of the drag coefficient tended to have a slightly larger inclination for the wing model with the sensors (Fig. 3.13(A)). The standard deviation of the lift coefficient needs to be known because unstable fluctuations in aerodynamic force can have a negative influence on flight dynamics. The results in Figs. 3.12(B) and 3.13(B) revealed that the standard deviation of the lift coefficient was slightly smaller for the wing with the sensor for every wind speed. This means that the feather-based structure on the upper surface of the wing for the purpose of airflow sensing does not have a serious negative influence on the aerodynamic performance of the wing. Conversely, it was found to contribute to the improvement of aerodynamic robustness through feather-based structures. This is caused by the interaction between the passive deformation of flexible structure and the flow fluctuations over the wing surface.

Dynamic measurements test

In this experiment, characteristics of the sensor was evaluated with a specific focus on its transient response caused by changes in the angle of incidence. To reproduce the effects of the changes in angle of attack dynamically, the servo motor was driven to change the angle of incidence. To provide some initial insights, two driving speeds of the servo motor were tested, 10 ° per second and 20 ° per second in uniform flow of 8 ms^{-1} and 10 ms^{-1}. The angle of incidence was varied from −10 ° to 20 ° in 1.5

seconds (Fig. 3.14) and in 3.0 seconds (Fig. 3.15). Every graph shows that the lift force plotted in red lines gradually increased along the time and dropped after a certain point of time when the angle of incidence reaches the stall angle. Maximum lift shown was lower in the wind speed of 8 ms^{-1} than 10 ms^{-1} because the dynamic pressure was smaller (Figs. 3.14(A) and 3.15(A)).

An interesting result that is that the sensor responses showed some peaks just before the point of time when the lift dropped due to the stall in every graph (Figs. 3.14 and 3.15). The black plotted line in each graph indicates the synthetic output which was averaged of seven hall-effect-type sensors. According to the increasing the angle of incidence, these synthetic responses gradually became larger. These responses qualitatively agreed with the results in static measurements. These results suggest the hall-effect-type sensors is useful for detecting the rapid increasing the angle of attack which cause the stall. If the peak response just before the stall can be utilized (hatched area in Figs. 3.14 and 3.15), it may be possible to control the angle of incidence and maintain an appropriate angle of attack before the wing stalls.

3.3.3 Discussion

In this study, hall-effect-type airflow sensors were fabricated and evaluated in wind tunnel experiments. These sensors resulted in the detection of dynamic changes in angle of attack and improved aerodynamic performance. These findings have great importance from the viewpoint of clarifying the effectiveness of information obtained from the deforming feather-like flexible structures that are exposed to unsteady airflows, both for birds and flying robots. In this subsection, the findings of this study on feather-based airflow sensor are discussed along with related previous studies.

Improving passive robustness in aerodynamic performance

The results of aerodynamic measurement in our study showed a slight improvement in aerodynamic performance with respect to stall characteristics, as well as in the studies targeting rain coverings and their normative structures (Allemand and Altman, (2016); Wang and Schlüter, 2012). Although it is known that adding structures based on covert feathers to artificial airfoils can help increase the maximum lift coefficient, the same improvement was not found in this study (Bechert, et al., 2000; Schlüter, 2009). This is possibly because the wing used in this study is a finite wing with a three-dimensional effect, and the effect of the lift coefficient improvement is limited (Wang and Schlüter,

2012). Another study that investigated the aerodynamic role of the fluttering artificial covert feathers on flow control showed artificial coverts with parameters in the chord position are useful in suppressing wake turbulence regardless of installation position (Ma, X., et al., 2022), which is analogous to the present study.

Considering that the arrangement of the sensors in the current study was not aerodynamically optimized, it may be possible to further enhance the aerodynamic performance by studying the optimal arrangement of the sensors. In this work, the geometries and arrangement of the sensors were determined to be suitable for gaining information of their deflections. Nevertheless, the result of improved aerodynamic performance, even though slightly, supports the usefulness of the artificial covert feather. Since the effect of the optimized arrangement of the artificial covert feathers on stall characteristics have been studied (Allemand and Altman, 2016; Wang and Schlüter, 2012), the design that can maximize collecting airflow information and improving aerodynamic performance should be pursued in the future study.

Airflow sensing by hall-effect-type flexible structures

Another advantage of this hall-effect-type sensors proposed in this study is that the stall could possibly be predicted from the sensor response at a time earlier than the wing fully stalls. The IMU can measure changes in lift due to disturbance factors, but it can only detect a stall, a sudden drop in lift, after the stall has occurred. Actually, our experiments showed that the sensors responded before lift stall that measured by the force sensor (Figs.3.14 and 3.15). Although feedback control of the angle of attack was not the subject of this study, the time lag between the sensor response and the wing stall is considered to be sufficient to afford a margin considering the flight control intervals.

Interestingly, hall-effect-type sensors that began to vibrate before the stall apparently amplified a slight fluctuation in the flow along the wing surface and detected it due to a flutter-like phenomenon. Although flutter phenomena in aircraft and structures should be avoided because they can lead to destructive vibrations, this does not necessarily seem to be the case in animals with flexible structures. Flutter may be used effectively in birds, as a study suggested that hummingbirds use the feather flutter in their courtship behavior (Clark et al., 2013). Another example, the study of the falcon diving flight has proposed the hypothesis that the flow induced flutter-like vibration of their dorsal feathers provide

a sensory input that helps them maintain a safe diving angle (Brücker, et al., 2016). From the viewpoint of fluid dynamics, the unsteady boundary layer behaves complexly at low Reynolds numbers, and reverse flow has been observed in the case where the flow is not completely separated from the upper surface of a pitching wing in a uniform flow (Kim et al., 2010). In this study, the vibration of the hall-effect-type sensors is thought to have reflected the flow variation that begins to occur in the gradual increasing of the angle of attack. The frequency of flow fluctuations measured by the hot-wire anemometer was equal to the sensor vibration frequency of about 5 Hz, which also suggests that the sensors' vibrations were induced by the unsteady airflow fluctuations (Figs. 3.17(A) and 3.17(B)).

Another advantage is that multiple sensors over the span-wise of the wing are redundant and provide airflow information robustly. It is known about wing redundancy in birds that they can fly with damaged or missing feathers, paying the cost but adjusting their flight behavior and body size (Chai, 1997; Swaddle and Witter, 1997). In contrast to this high adaptability of birds in terms of locomotion and physiology that has been investigated, however, the cost of feather missing to the airflow sensing function is still unclear. Intuitively, the missing a few feathers should not result in a total loss of the function for airflow sensing. For example, previous study using a small fixed-wing aircraft with four pressure sensors dispersed along the chord length demonstrated that even if one of the sensors failed, sufficient airflow information could still be collected (Araujo-Estrad et al., 2017). The integration of redundant multi-sensor information is also considered to be a method to improve system accuracy and reliability in a variety of research topics, not only for flying robots, but also for other research topics in robotics (Guo et al., 2018; Ren et al., 2002). This hall-effect-type sensor with light-weight and low-cost makes it easy to add airflow sensing capability to a bird-size fixed-wing MAV with minimal mass increase, and it can easily realize the advantage of redundancy by installing them at multiple points.

Applicability of the airflow sensor to a flying robot

Additional function of sensing airflow information around the flying robot would enhance the control stability in unpredictable wind conditions. Like haptic feedback technology in robotic hands, airflow information given by the hall-effect-type sensors, which act as aerodynamic force receptors, can be useful in predicting and preventing stall that endanger stable flight of flying robots. In addition, payload cost required for a flying robot will be low, even if many sensors are installed because they are

lightweight like feathers. Although there is an issue of how sensor fusion should be performed, the integration of information from inertial sensors and hall-effect-type sensors provides advantages for the control of flying robots. For example, redundant sensors may contribute to increased reliability of flight controllers because they can compensate each other even if some of them fail.

This feather-based airflow sensor has potential applications in controlling flying robots as already mentioned. However, since this research was limited to evaluating sensor characteristics under the assumption of horizontal flight, further validation in more realistic conditions or flight experiments will be required in future study. If a flying robot can achieve stable flight under disturbed flow by using the hall-effect-type airflow sensors, it may be able to acquire highly stable flight technique such as wind-hovering, as is performed by a kestrel (Videler et al., 1983).

References

Allemand, G., and Altman, A. (2016) Post-stall performance improvement through bio-inspired passive covert feathers. *54th AIAA Aerospace Sciences Meeting*, AIAA-2016-2042, doi: 10.2514/6.2016-2042.

Araujo-Estrada, S. A., Salama, F., Greatwood, C., Wood, K., Richardson, T., and Windsor, S. P. (2017) Bio-inspired distributed strain and airflow sensing for small unmanned air vehicle flight control. *AIAA Guidance, Navigation, and Control Conference*, AIAA-2017-1487, doi: 10.2514/6.2017-1487.

Bechert, D.W., Bruse, M., Hage, W., and Meyer, R. (2000) Fluid mechanics of biological surfaces and their technological application. *Naturwissenschaften* **87**, 157-171, doi: 10.1007/s001140050696.

Brown, R. E., and Fedde, M. R. (1993) Airflow sensors in the avian wing. *J. exp. Biol.* **179**, 13-30.

Brücker, C., Schlegel, D., and Triep, M. (2016) Feather vibration as a stimulus for sensing incipient separation in falcon diving flight. *Natural Resources* **7**, 411-422, doi: 10.4236/nr.2016.77036.

Carruthers, A. C., Thomas, A. L. R., and Taylor, G. K. (2007) Automatic aeroelastic devices in the wings of a steppe eagle Aquila nipalensis. J. Exp. Biol. **210**, 4136-4149, doi: 10.1242/jeb.011197.

Chai, P. (1997) Hummingbird hovering energetics during moult of primary flight feathers. *J. exp. Biol.* **200**, 1527-1536, doi: 10.1242/jeb.200.10.1527.

Chang, E., Matloff, L. Y., Stowers, A. K., and Lentink, D. (2020) Soft biohybrid morphing wings with feathers underactuated by wrist and finger motion. *Sci. Robot.* **5**, eaay1246, doi: 10.1126/scirobotics.aay1246.

Cheney, J. A., Stevenson, J. P. J., Durston, N. E., Song, J., Usherwood, J. R., Bomphrey, R. J., and Windsor, S. P. (2020) Bird wings act as a suspension system that rejects gusts. *Proc. R. Soc. B* **287**, 20201748, doi: 10.1098/rspb.2020.1748.

Chin, D. D., Matloff, L. Y., Stowers, A. K., Tucci E. R., and Lentink D. (2017) Inspiration for wing design: how forelimb specialization enables active flight in modern vertebrates. *J. R. Soc. Interface* **14**, 20170240, doi: 10.1098/rsif.2017.0240.

Clark, C. J., Elias, D. O., and Prum, R. O. (2013) Hummingbird feather sounds are produced by aeroelastic flutter, not vortex-induced vibration. *J. exp. Biol.* **216**, 3395-3403, doi: 10.1242/jeb.080317.

Guo, D., Zhong, M., and Zhou, D. (2018) Multisensor data-fusion-based approach to airspeed measurement fault detection for unmanned aerial vehicles. *IEEE Trans. Instrum. Meas.* **67**, 317-327, doi: 10.1109/TIM.2017.2735663.

Ikeda, T., Ueda, T., Nakata, T., Noda, R., Tanaka, H., Fujii, T., and Liu, H. (2018) Morphology effects of leading-edge serrations on aerodynamic force production: an integrated study using PIV and force measurements. *J. Bionic Eng.* **15**, 661-672, doi: 10.1007/s42235-018-0054-4.

Kim, D.-H., and Chang, J.-W. (2010) Unsteady boundary layer for a pitching airfoil at low Reynolds numbers. *J. Mech. Sci. Technol.* **24**, 429-440, doi: 10.1007/s12206-009-1105-x.

Kim, S., Nam, T., and Park, S. (2004) Measurement of flow direction and velocity using a micromachined flow sensor. *Sens. Actuator A-Phys.* **114**, 312-318, doi: 10.1016/j.sna.2003.12.019.

Klaassen, v. O. B., Choroszucha, R., and Tobalske, B. W. (2020) Passive aeroelastic deflection of avian primary feathers. *Bioinspir. Biomim.* **15**, 056008, doi: 10.1088/1748-3190/ab97fd.

Lee, S.-i., Kim, J., Park, H., Jabłoński, P. G., and Choi, H. (2015) The function of the alula in avian flight. *Sci. Rep.* **5**, 9914, doi:10.1038/srep09914.

Luo, R. C., Yih, C.-C., and Su, K. L. (2002) Multisensor fusion and integration: approaches, applications, and future research directions. *IEEE Sens. J.* **2**, 107-119, doi: 10.1109/JSEN.2002.1000251.

Ma, X., Gong, X., Tang, Z., and Jiang, N. (2022) Control of leading-edge separation on bioinspired airfoil with fluttering coverts. *Phys. Rev. E* **105**, 025107, doi: 10.1103/PhysRevE.105.025107.

Mohamed, A., Watkins, S., Clothier, R., and Abdulrahim, M. (2014) Influence of turbulence on MAV roll perturbations. *Int. J. Micro Air Veh.* **6**, 175-190, doi: 10.1260/1756-8293.6.3.175.

Reynolds, K. V., Thomas, A. L. R., and Taylor, G. K. (2014) Wing tucks are a response to atmospheric turbulence in the soaring flight of the steppe eagle *Aquila nipalensis*. J. R. Soc. Interface **11**, 20140645, doi:10.1098/rsif.2014.0645.

Rosti, M. E., Kamps, L., Bruecker, C., Omidyeganeh, M., and Pinelli, A. (2017) The PELskin project-part V: towards the control of the flow around aerofoils at high angle of attack using a self-activated deployable flap. *Meccanica* **52**, 1811-1824, doi: 10.1007/s11012-016-0524-x.

Schlüter, J. U. (2009) Lift enhancement at low Reynolds numbers using pop-up feathers. *39th AIAA Fluid Dynamics Conference*, AIAA-2009-4195, doi: 10.2514/6.2009-4195.

Sterbing-D'Angelo, S.,Chadha, M., Chiu, C., Falk, B., Xian, W., Barcelo, J., Zook, J. M., and Moss, C. F. (2011) Bat wing sensors support flight control. *Proc. Natl. Acad. Sci.* **108**, 11291-11296, doi: 10.1073/pnas.1018740108.

Sullivan, T. N., Wang, B., Espinosa, H. D., and Meyers, M. A. (2017) Extreme lightwight structures: avian feathers and bones. *Mater. Today* **20**, 377-391, doi: 10.1016/j.mattod.2017.02.004.

Swaddle, J. P. and Witter, M. S. (1997) The effects of molt on the flight performance, body mass, and behavior of European starlings (Sturnus vulgaris): An experimental approach. *Can. J. Zool.* **75**, 1135-1146, doi: 10.1139/z97-136.

Takahashi, H., Dung, Nguyen M., Matsumoto, K., and Shimoyama, I. (2012) Differential pressure sensor using a piezoresistive cantilever. *J. Micromech. Microeng.* **22**, 055015, doi: 10.1088/0960-1317/22/5/055015.

Tucker, V. A. (1995) Drag reduction by wing tip slots in a gliding Harris' hawk, *Parabuteo unicinctus*. *J. Exp. Biol.* **198**, 775-781, doi: 10.1242/jeb.198.3.775.

Videler, J. J., Weihs, D, and Daan, S. (1983) Intermittent gliding in hunting flight of the Kestrel, *Falco tinnunculus* L. *J. exp. Biol.* **102**, 1-12, , doi: 10.1242/jeb.102.1.1.

Wang, C. H. J. and Schlüter, J. (2012) Stall control with feathers: Self-activated flaps on finite wings at low Reynolds numbers. *C. R. Mec.* **340**, 57-66, doi: 10.1016/j.crme.2011.11.001.

Watkins, S., Burry, J., Mohamed, A., Marino, M., Prudden, S., Fisher, A., Kloet, N., Jakobi, T., and Clothier, R. (2020) Ten questions concerning the use of drones in urban environments. *Build. Environ.***167**, 106458, doi: 10.1016/j.buildenv.2019.106458.

Xu, X., Zhou, Z., Dudley, R., MacKem, S., Chuong, C. M., Erickson, G. M., and Varricchio, D. J. (2014) An integrative approach to understanding bird origins. *Science* **346**, 1253293, doi: 10.1126/science.1253293.

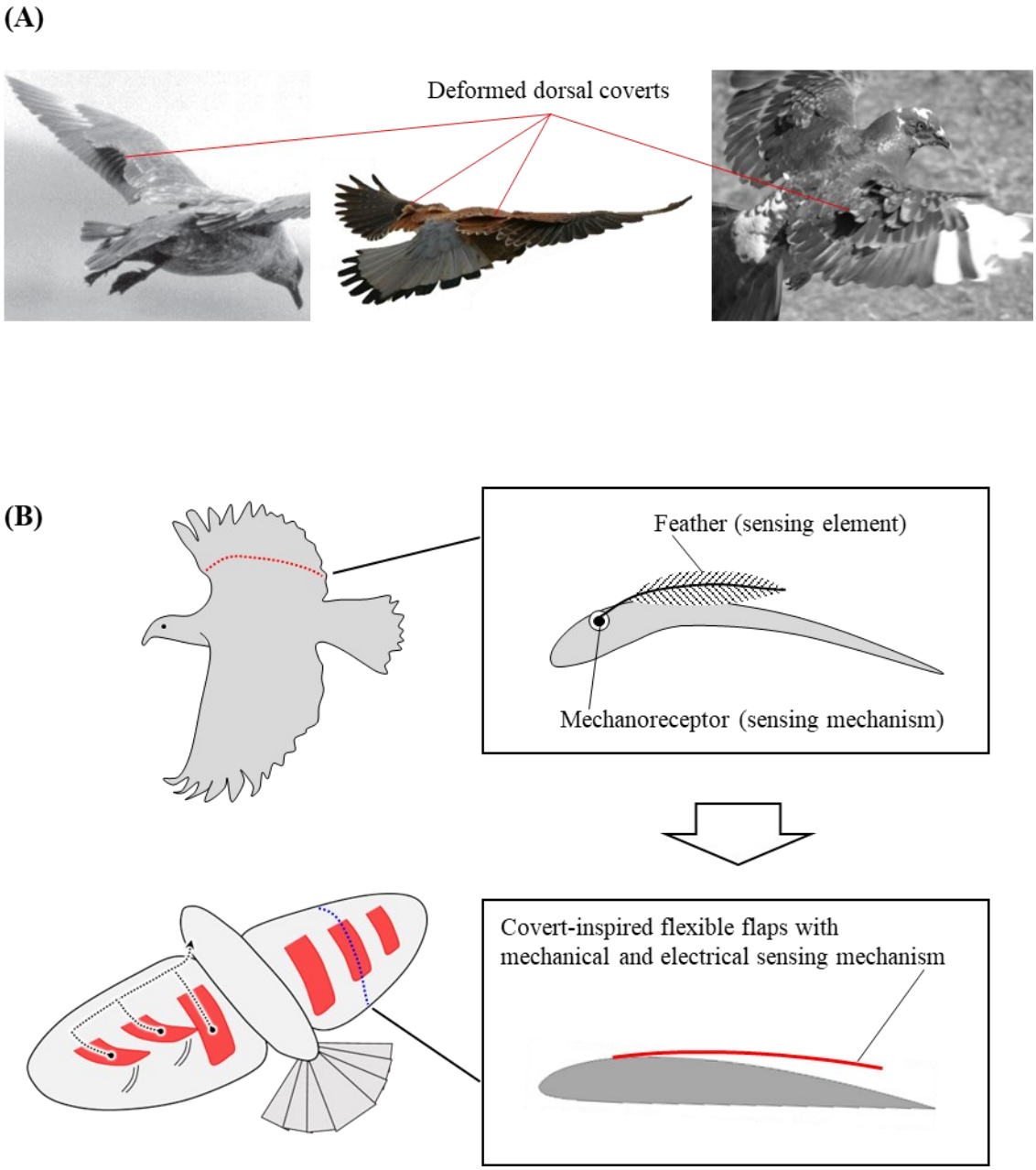

Fig. 3.1 (A) Deformed dorsal coverts in response to the winds. (left) Skua in landing approach (from Lindhe Norberg, 2002). (middle) Kestrel in wind-hovering (from Mohamed et al., 2014). (right) Pigeons in landing approach. (B) (top) Schematic diagram of a mechanoreceptor and feather in a bird wing (from Mohamed et al., 2014). (bottom) Conceptional drawing of an artificial feather-based flexible sensor for a flying robot.

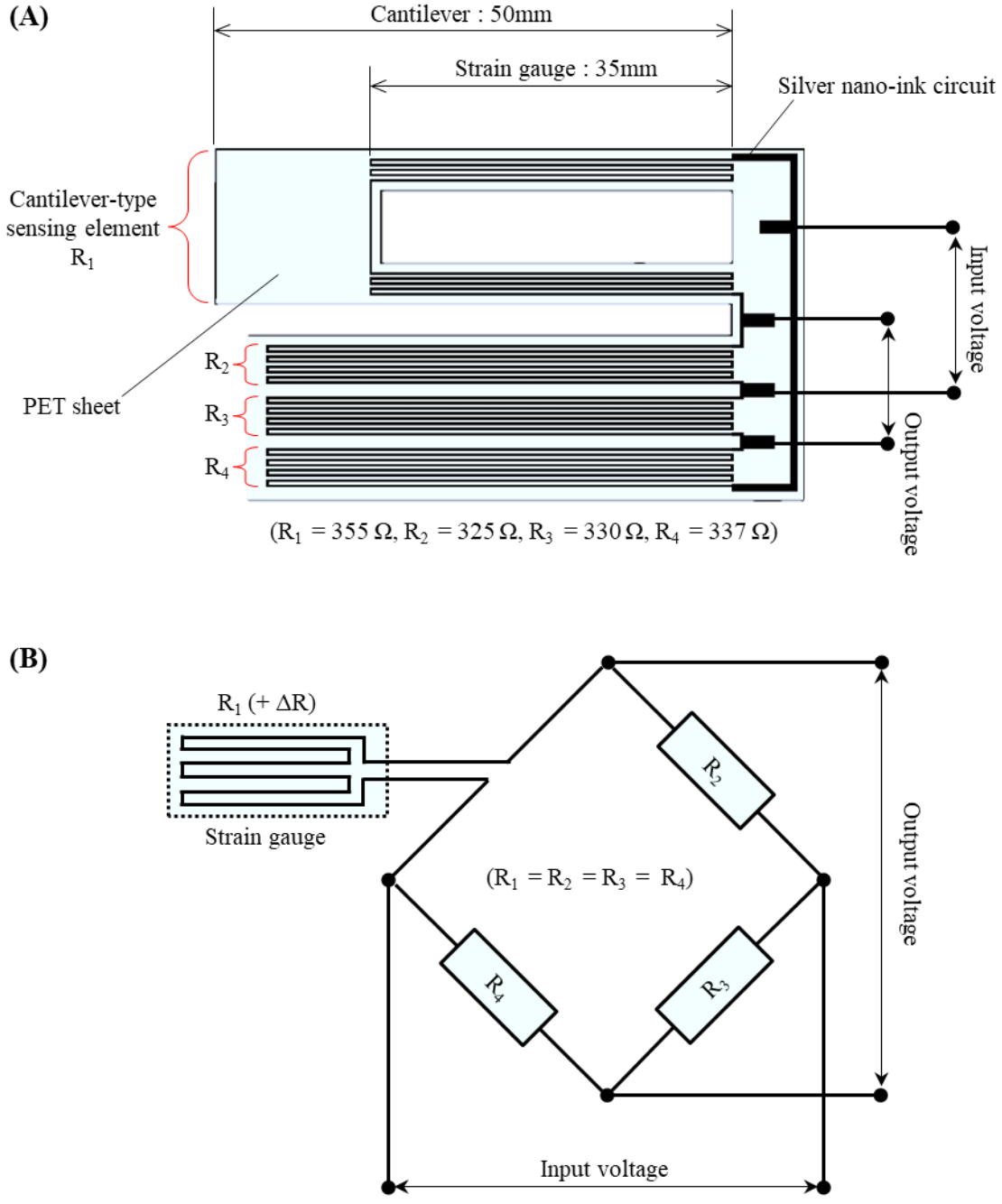

Fig. 3.2 (A) Schematic diagram of strain-gauge-type airflow sensor fabricated by silver nano-ink printing. (B) Quarter bridge circuit for strain gauge sensor.

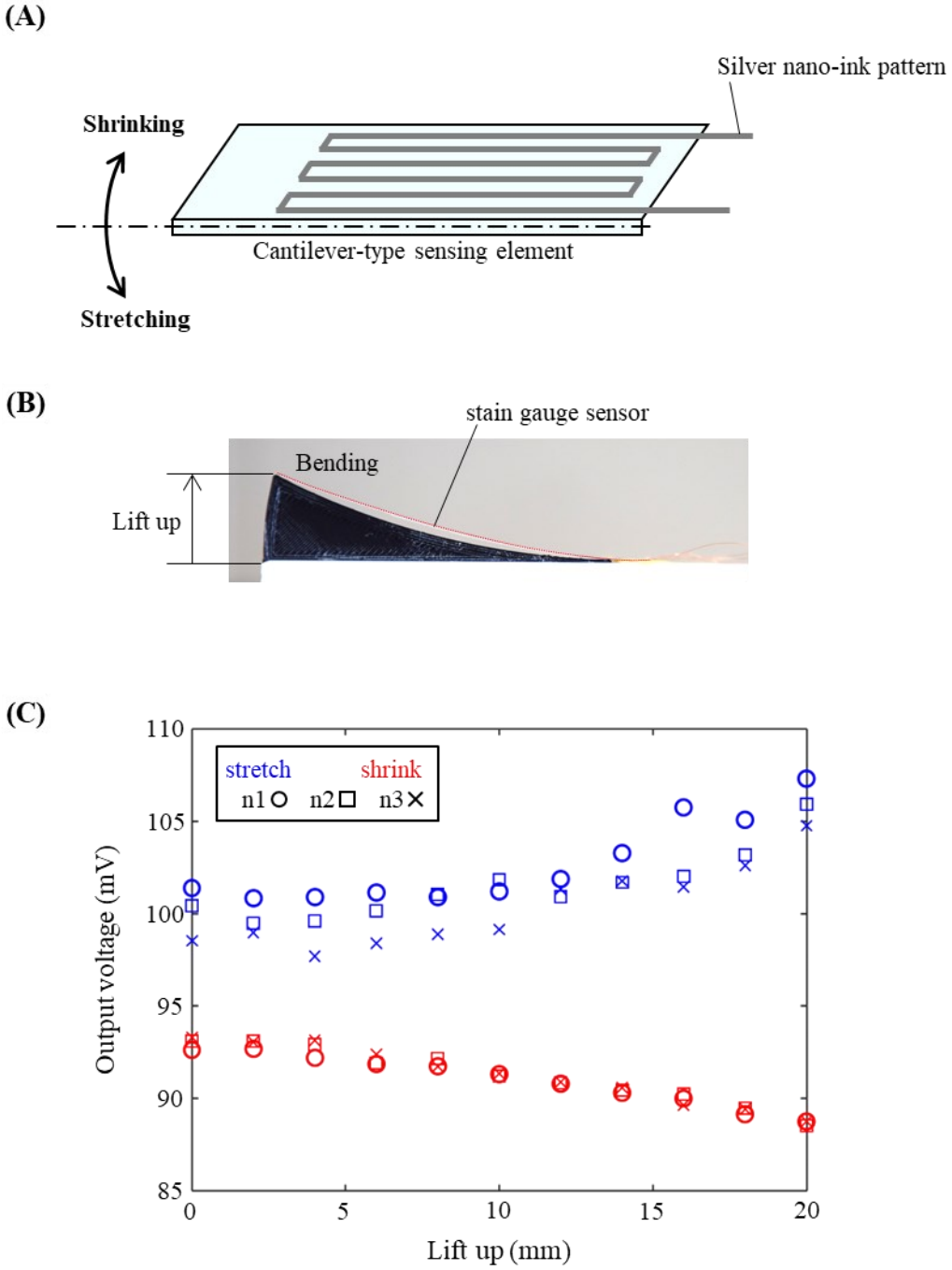

Fig. 3.3 (A) Schematic diagram of bending direction of the strain-gauge-type sensor with silver nano-ink pattern. (B) Bending test of the strain-gauge-type sensor. (C) Comparison of sensor output voltages for bending directions in stretching and shrinking.

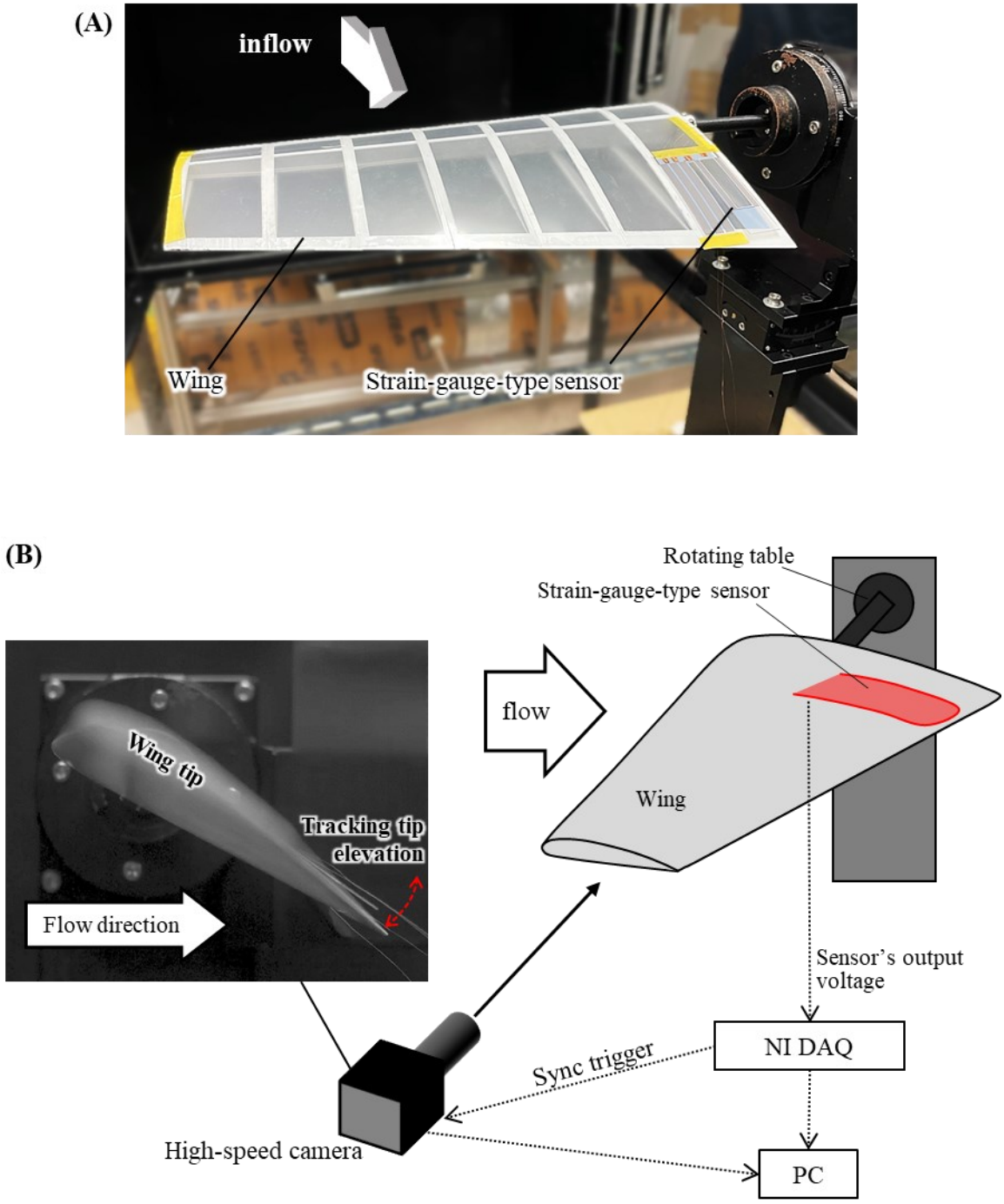

Fig. 3.4 Setups for wind tunnel experiments that test the characteristics of strain-gauge-type airflow sensor. (A) Appearance of experimental wing on which sensors were attached, viewed from diagonal-backward-left angle. (B) Schematic diagram of experimental equipment and an example of high-speed camera image for tracking the deformation of the sensor.

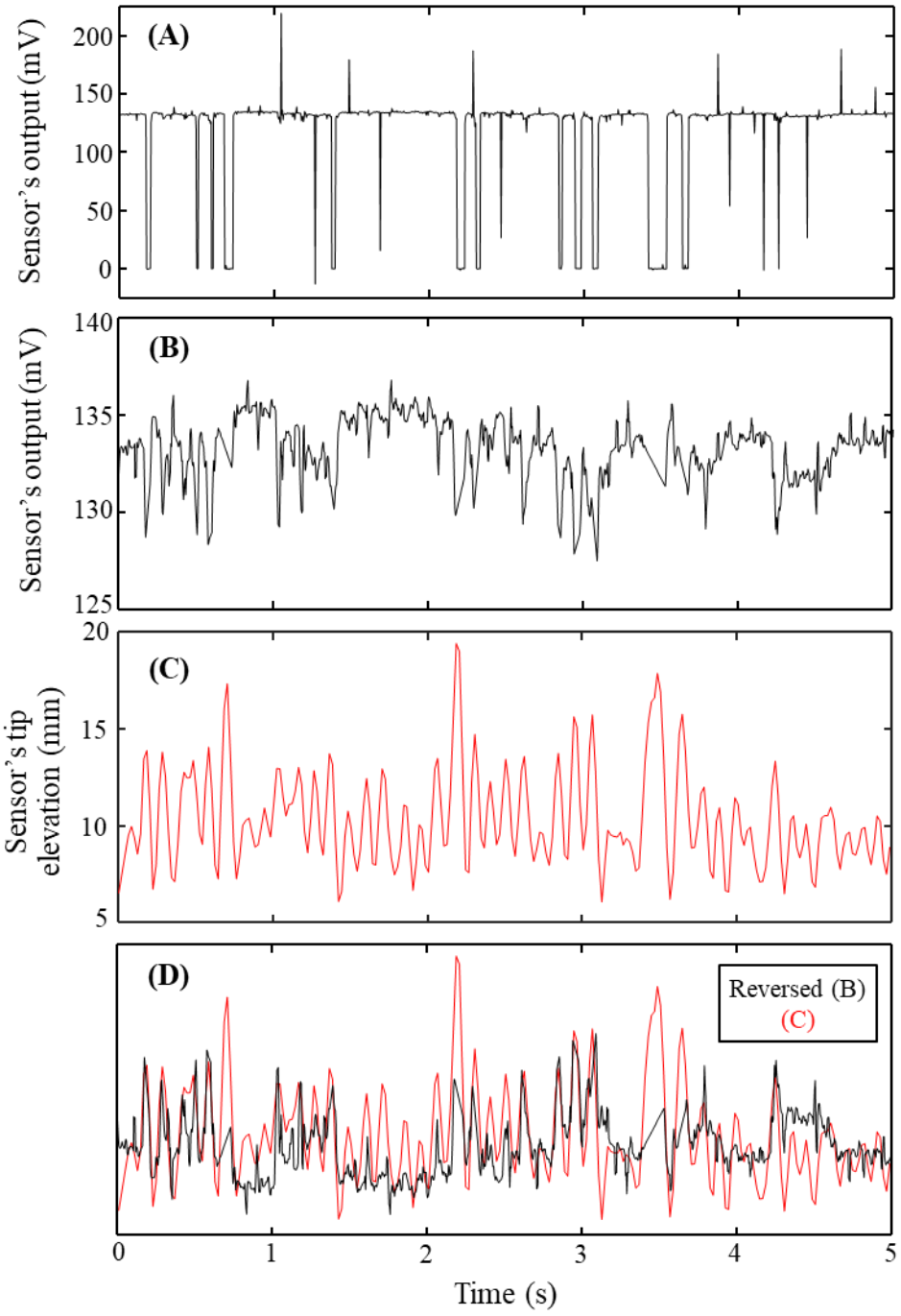

Fig. 3.5 Comparison of measured data of strain-gauge-type sensor's output voltage and tracking data of sensor's tip elevation at a wind speed of 10 ms^{-1} with wing's angle of incidence of 30 °. (A) Raw data including measurement error such as noise. (B) Post-processed data excluding outliers due to noise. (C) Sensor's tip tracking data obtained high-speed camera images. (D) Overlapping plot of (C) and vertically inverted (B).

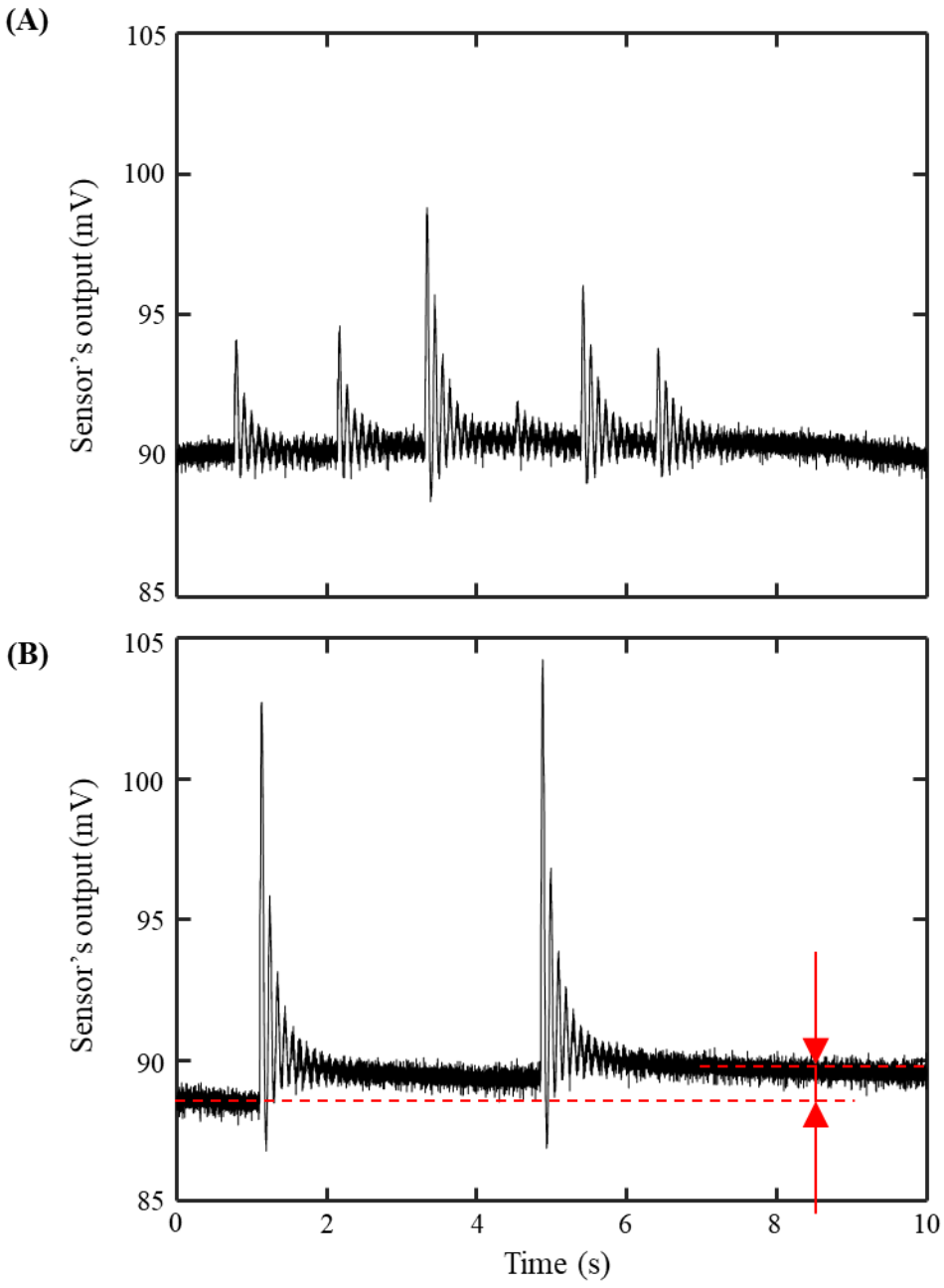

Fig. 3.6 Vibration response of strain-gauge-type sensor flicked by a finger (A) weekly and (B) strongly.

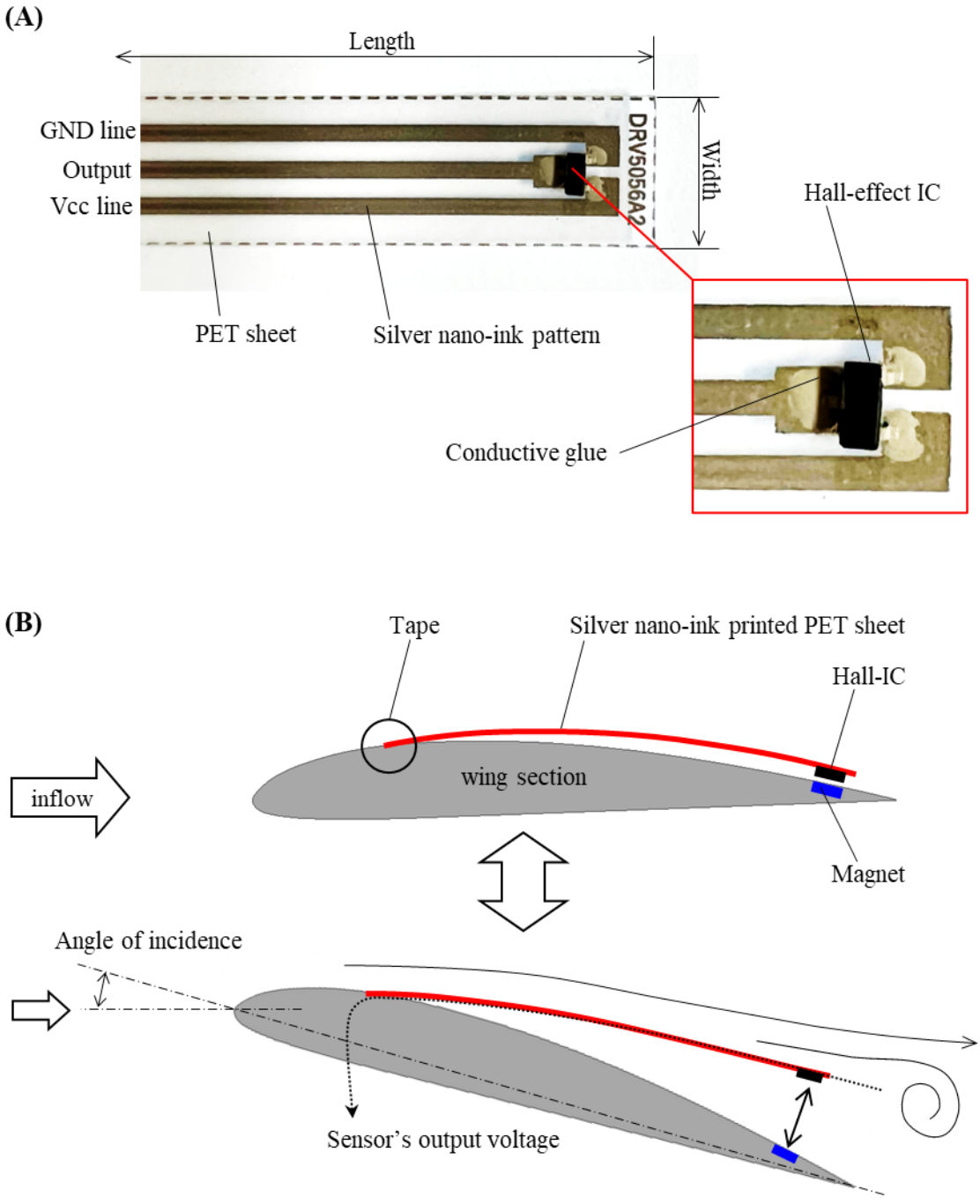

Fig. 3.7 (A) Images of hall-effect-type sensor that was made of a hall-effect IC and PET sheet printed with silver nano-ink circuit. (B) Schematic diagram of the behavior of hall-effect-type sensor attached to the wing.

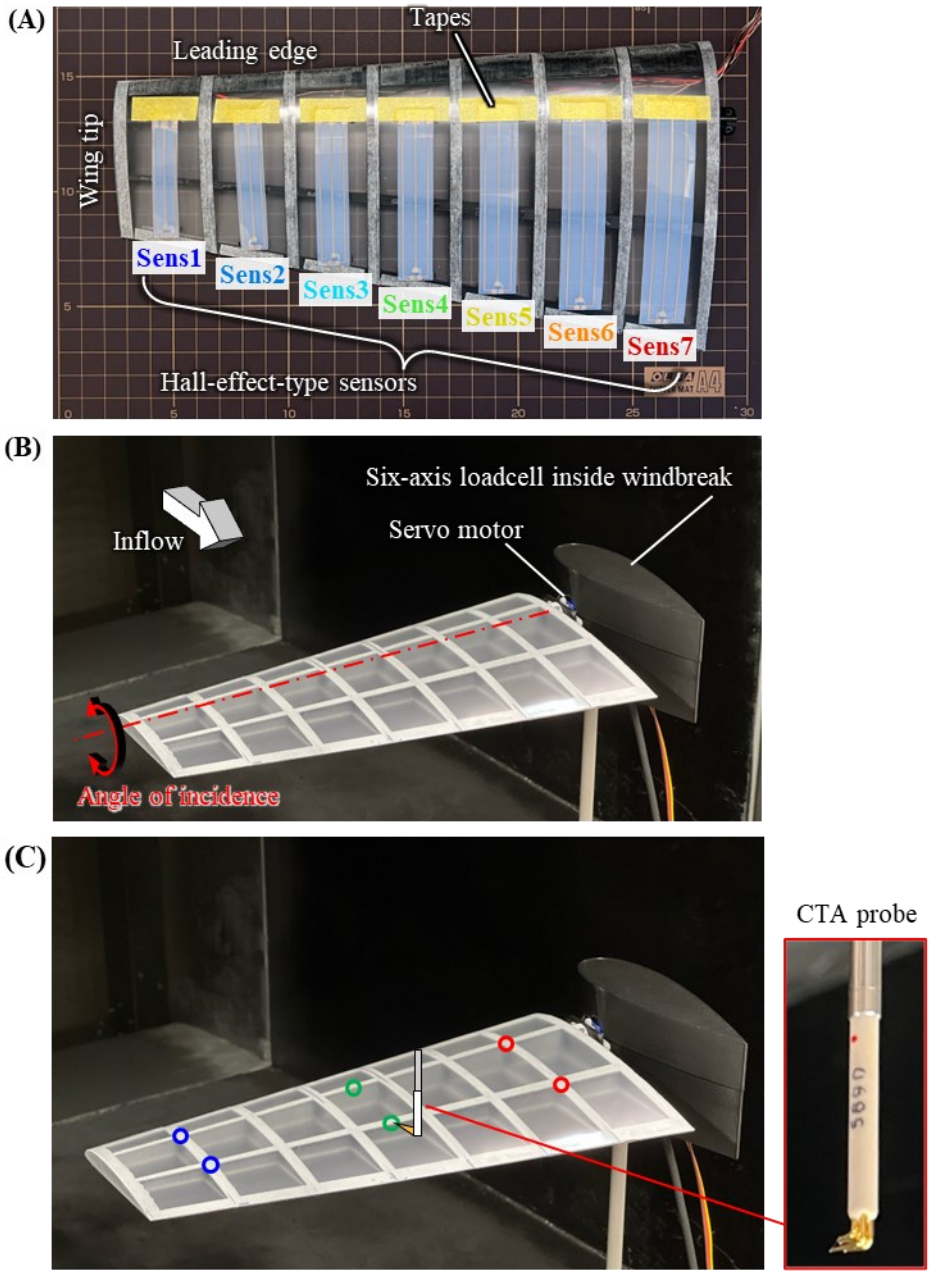

Fig. 3.8 (A) Top view of the model wing with the aspect ratio of 5 and taper ratio of 0.5 for wind tunnel experiments. Feather-inspired flexible sensors were taped at 25% chord position from leading edge and their rear tips were freely movable. The sensors were sequentially numbered 1 to 7 from the distal to proximal side of the wing. (B) Set up of wind tunnel experiments. The angle of incidence of the wing was controlled by a servomotor. Wing's aerodynamic forces were measured by a six-axis force sensor. The servo motor and force sensor were covered by a windbreak in the shape of NACA airfoil. (C) Inserted position of hot-wire probe. The probe tip was fixed a few millimeters above the wing surface at the position illustrated by the blue, green, and red circle.

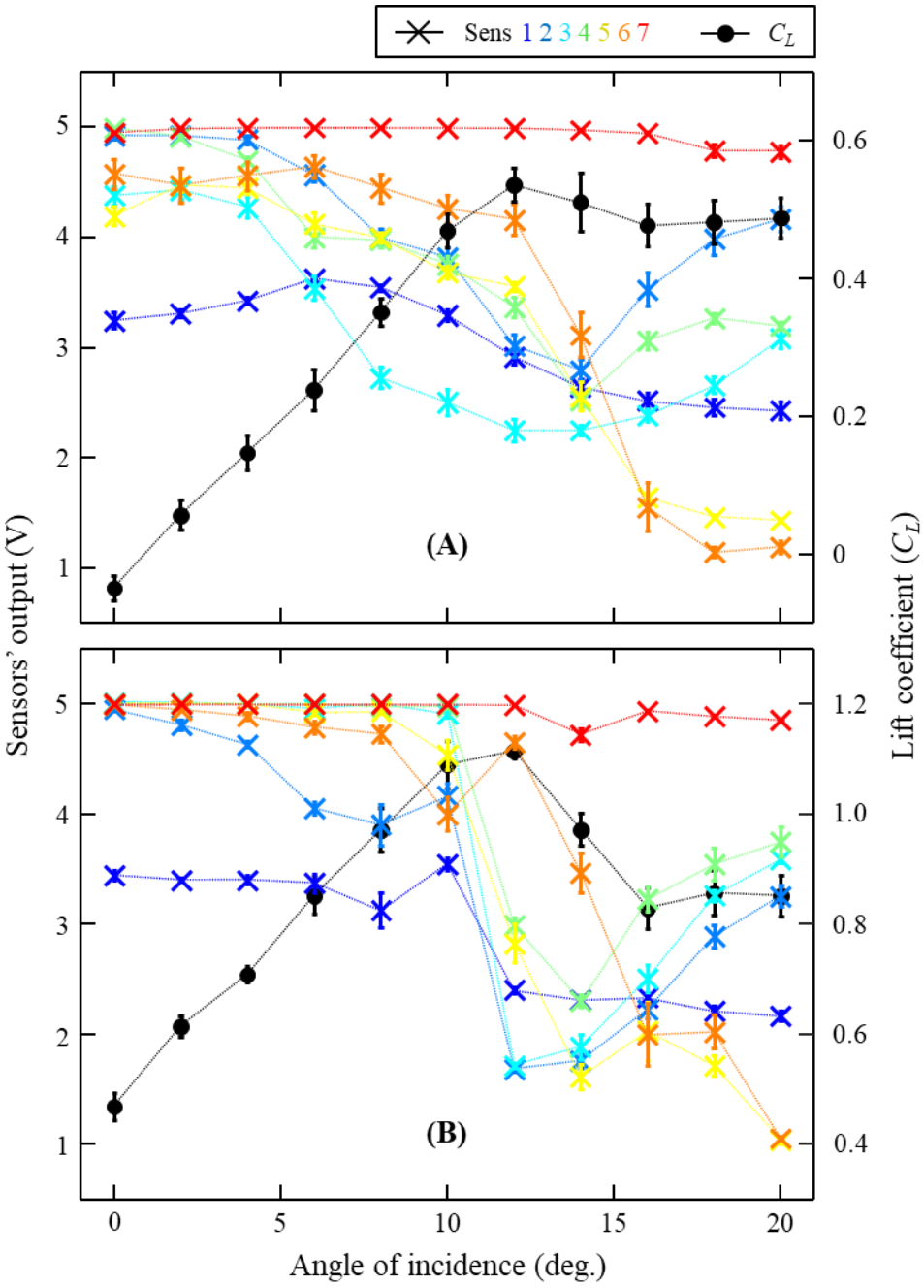

Fig. 3.9 Hall-effect-type sensors' response and lift coefficient corresponding to the change of angle of incidence of the wing in (A) 8 ms^{-1} and (B) 10 ms^{-1}. The sensors output 5V when they are close to the wing surface and 0V as they rise upward.

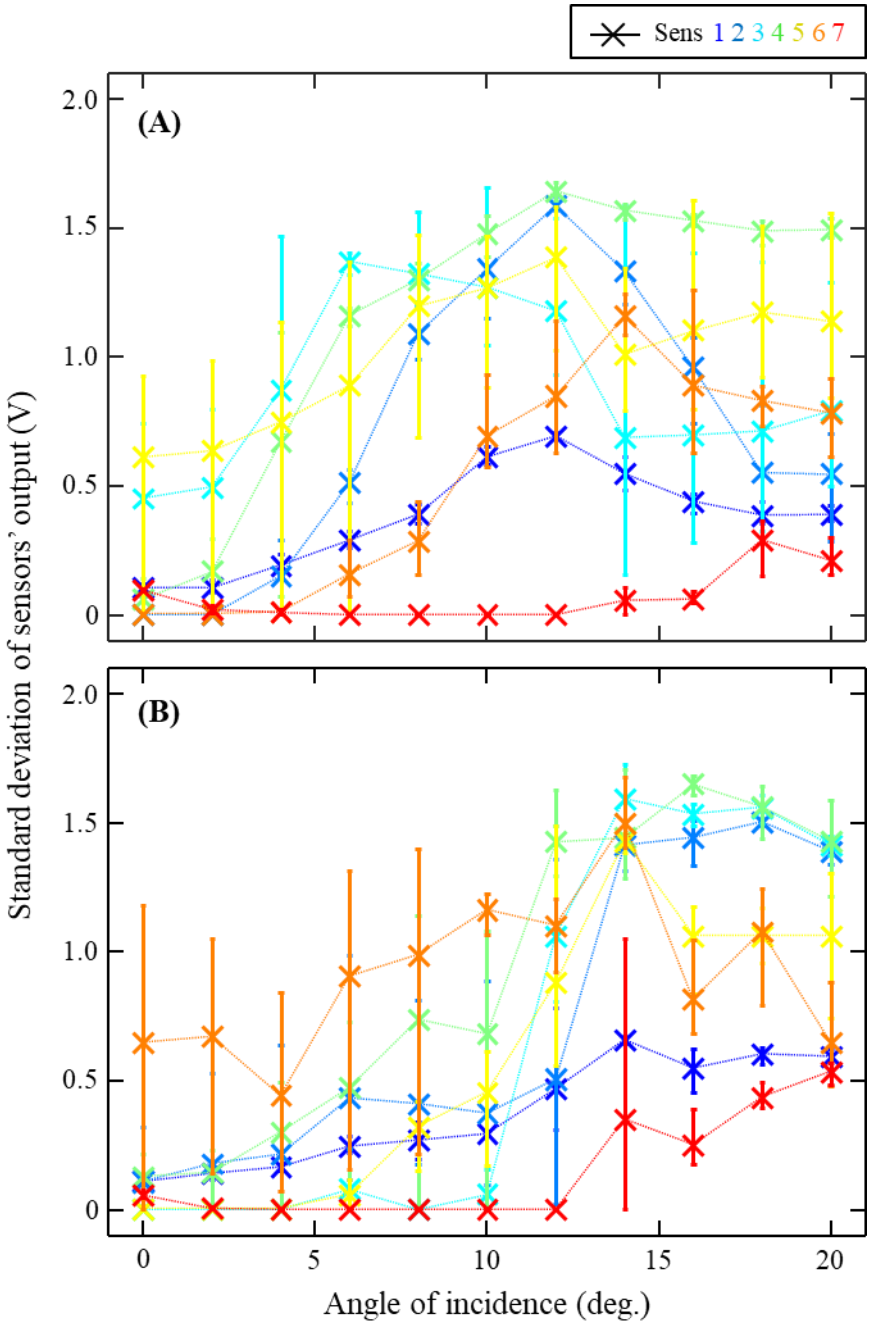

Fig. 3.10 Standard deviation of hall-effect-type sensors' outputs corresponding to the change of angle of incidence of the wing in (A) 8 ms^{-1} and (B) 10 ms^{-1}.

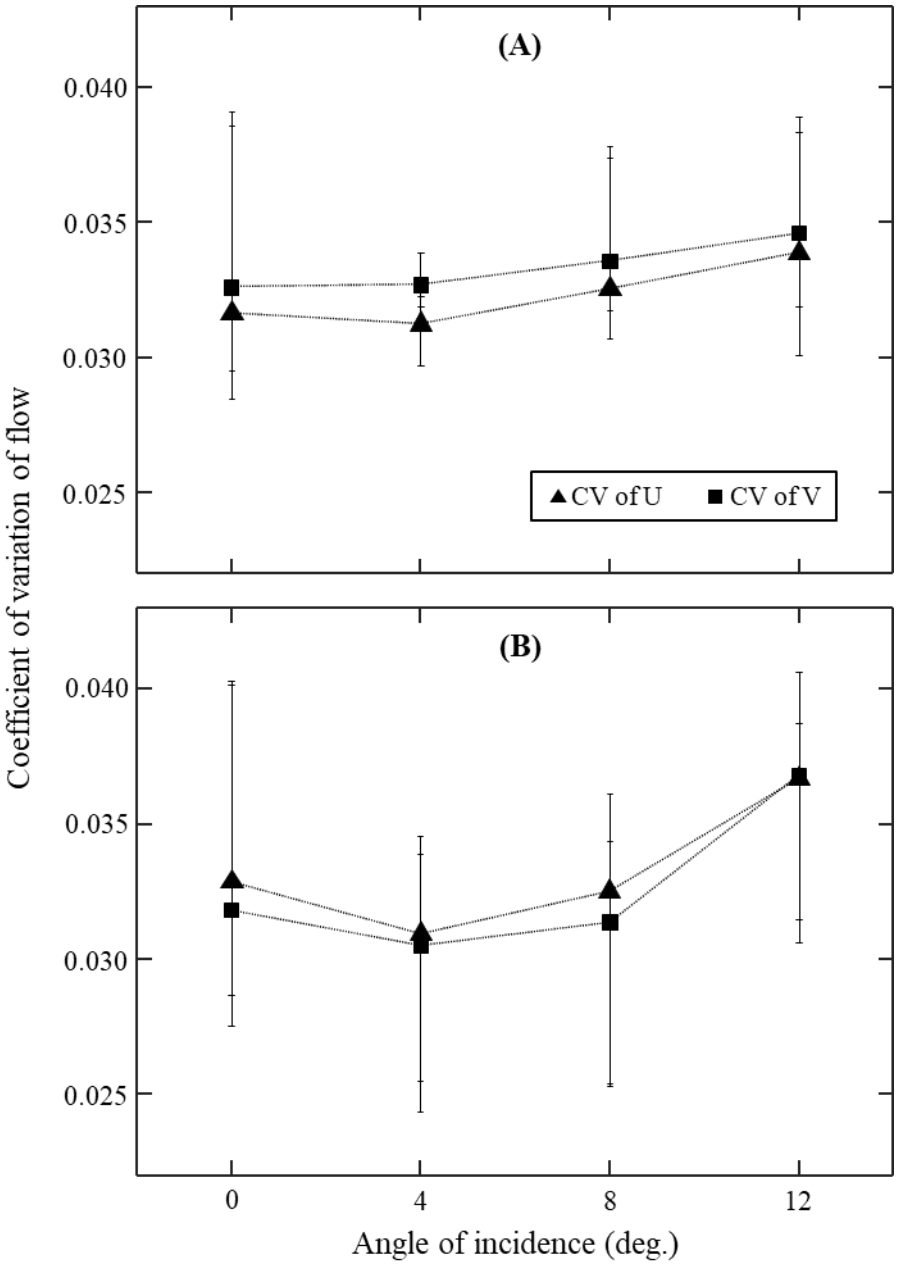

Fig. 3.11 Coefficient of variation of the flow near the upper wing surface corresponding to the change of angle of incidence of the wing in (A) 8 ms^{-1} and (B) 10 ms^{-1}.

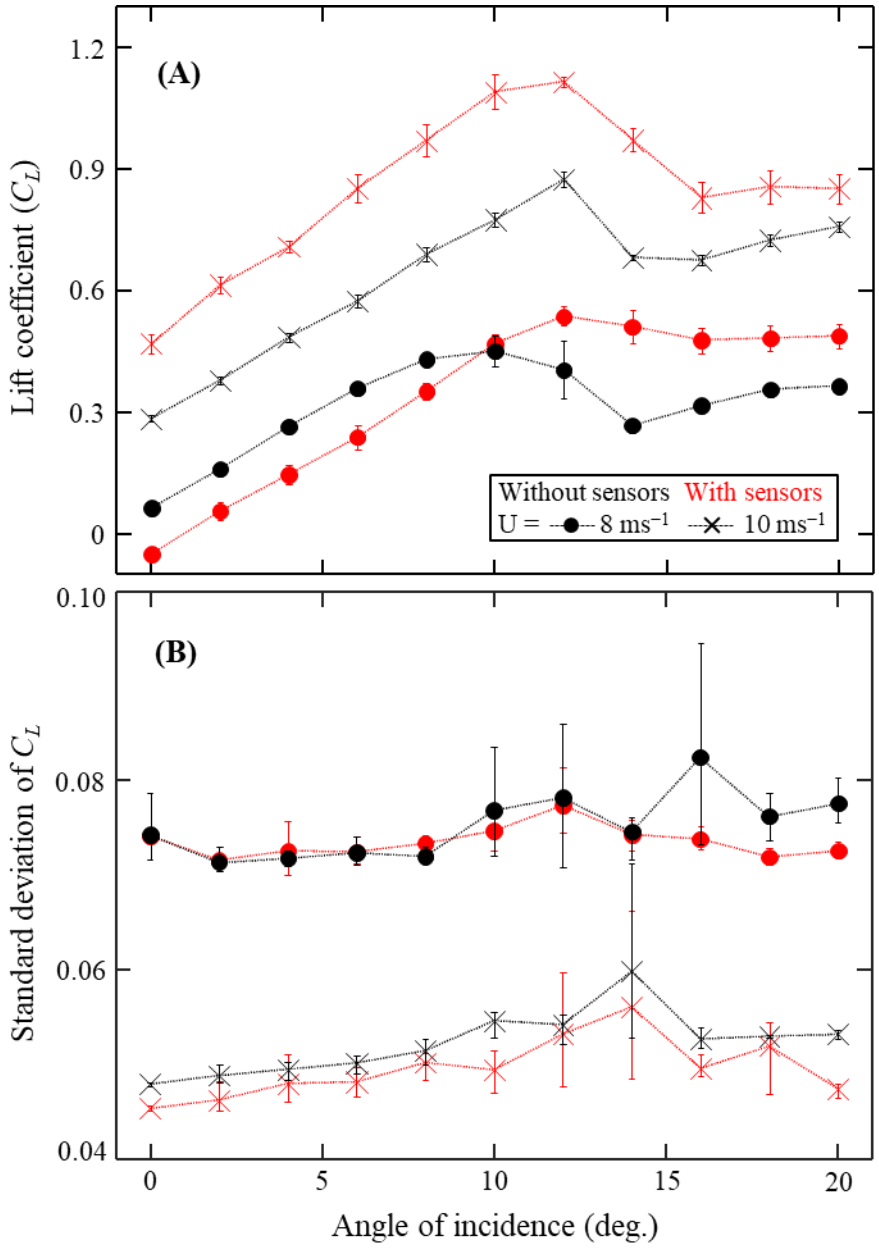

Fig. 3.12 Comparison of aerodynamic performance between a plane wing without the sensors and a wing with the sensors. (A) Lift coefficient and (B) standard deviation of lift coefficient corresponding to the change of angle of incidence of the wing.

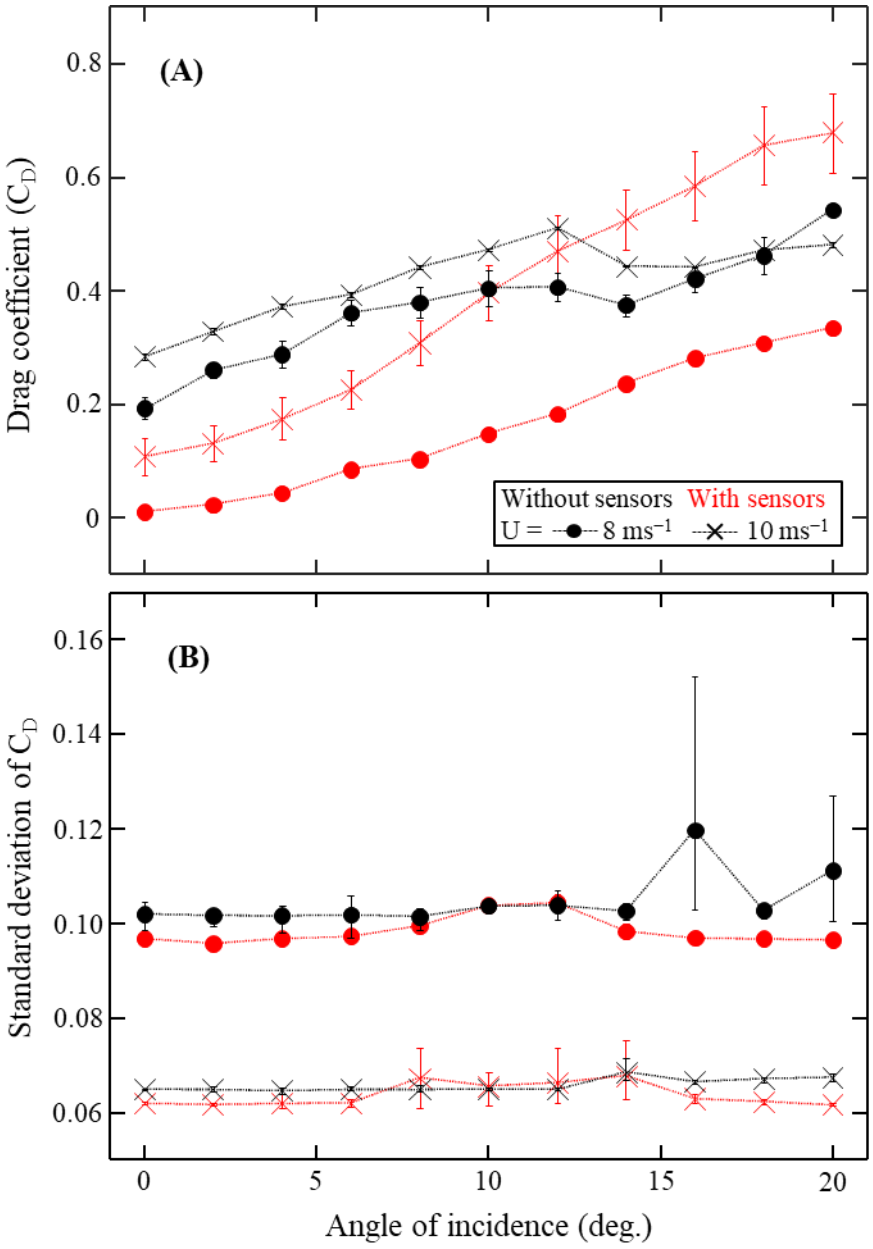

Fig. 3.13 Comparison of aerodynamic performance between a plane wing without the sensors and a wing with the sensors. (A) Drag coefficient and (B) standard deviation of drag coefficient corresponding to the change of angle of incidence of the wing.

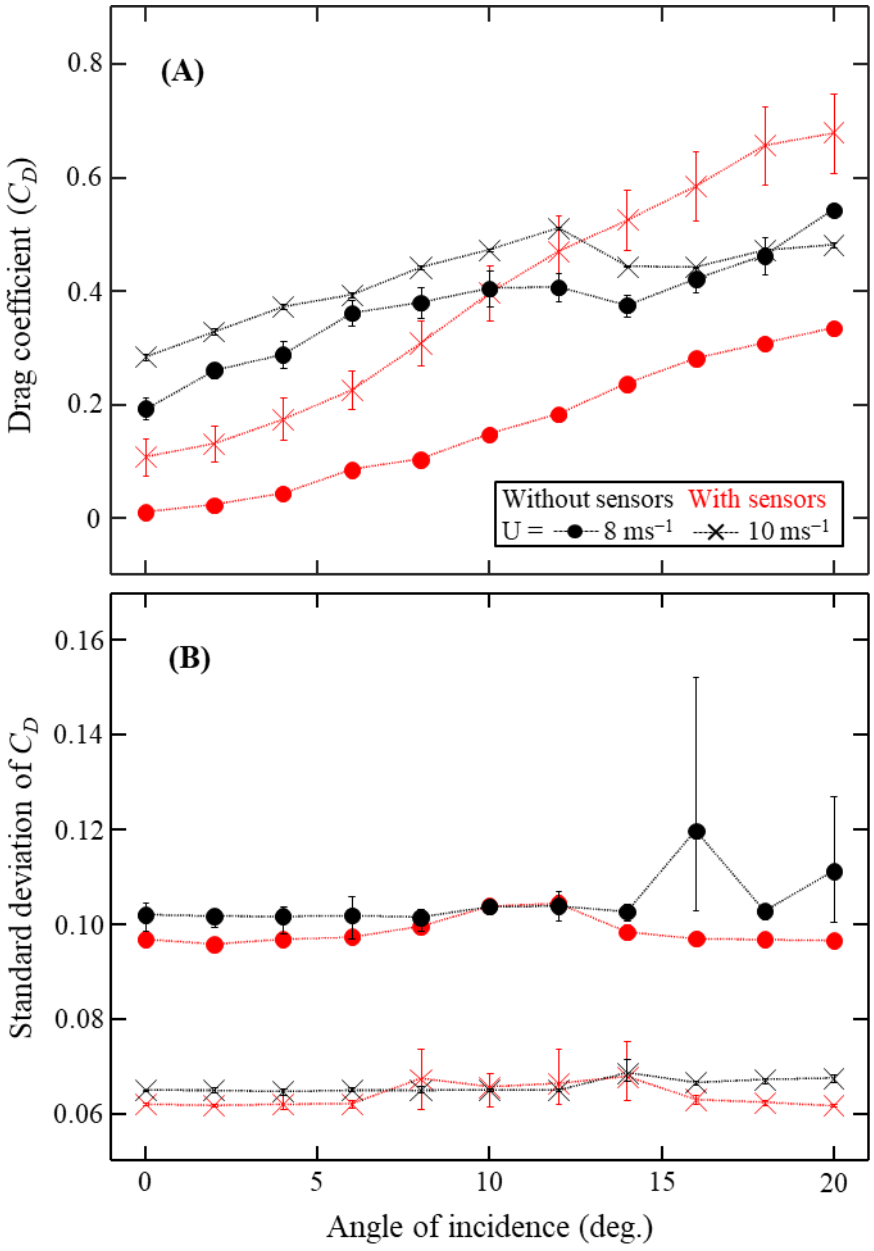

Fig. 3.14 Dynamic responses of hall-effect-type sensors along time series in (A) 8 ms^{-1} and (B) 10 ms^{-1}. The angle of incidence of the wing was varied from −10 °to 20 ° in 1.5 seconds. Synthetic sensor value represents the average of the seven hall-effect-type sensors.

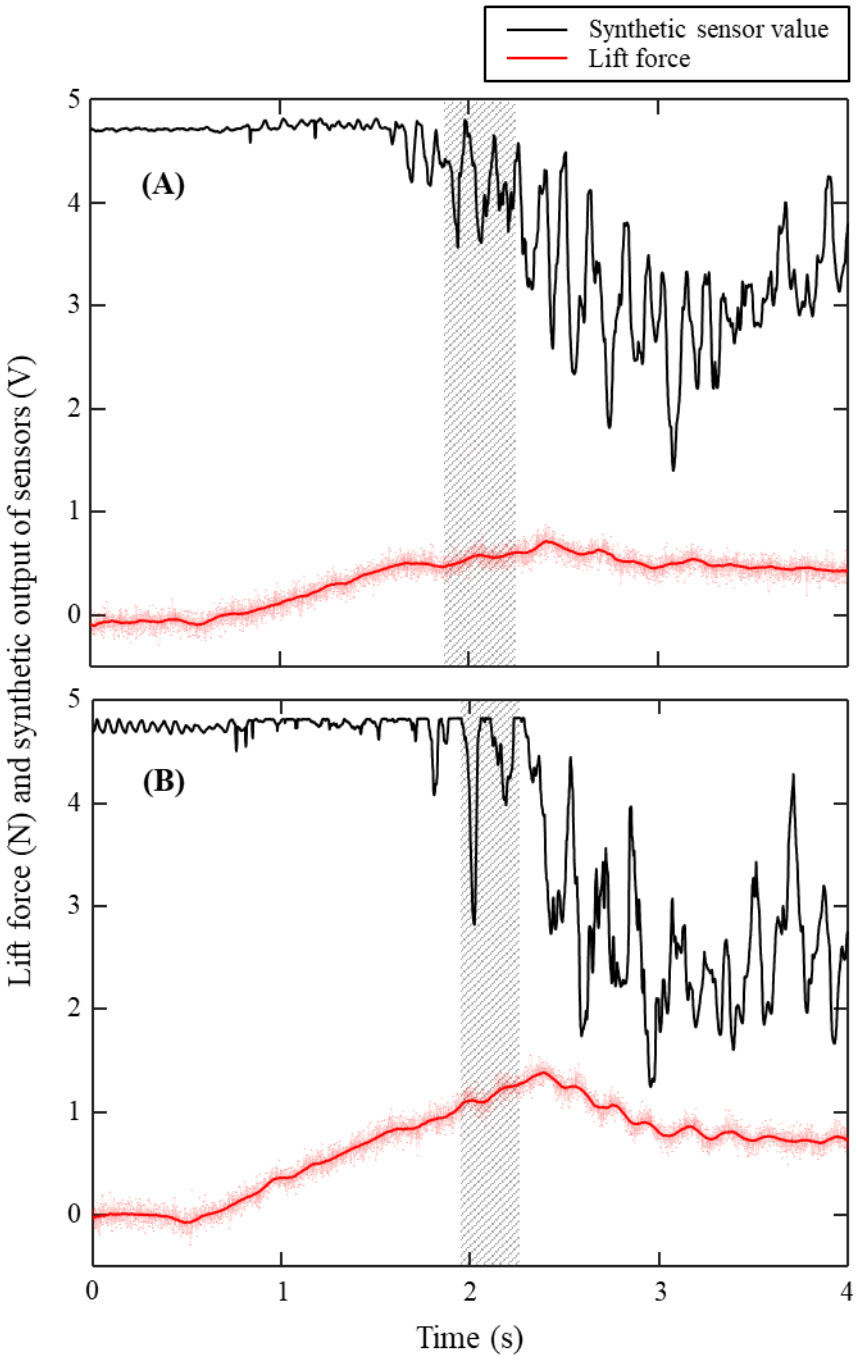

Fig. 3.15 Dynamic responses of hall-effect-type sensors along time series in (A) 8 ms^{-1} and (B) 10 ms^{-1}. The angle of incidence of the wing was varied from −10 °to 20 ° in 3.0 seconds. Synthetic sensor value represents the average of the seven hall-effect-type sensors.

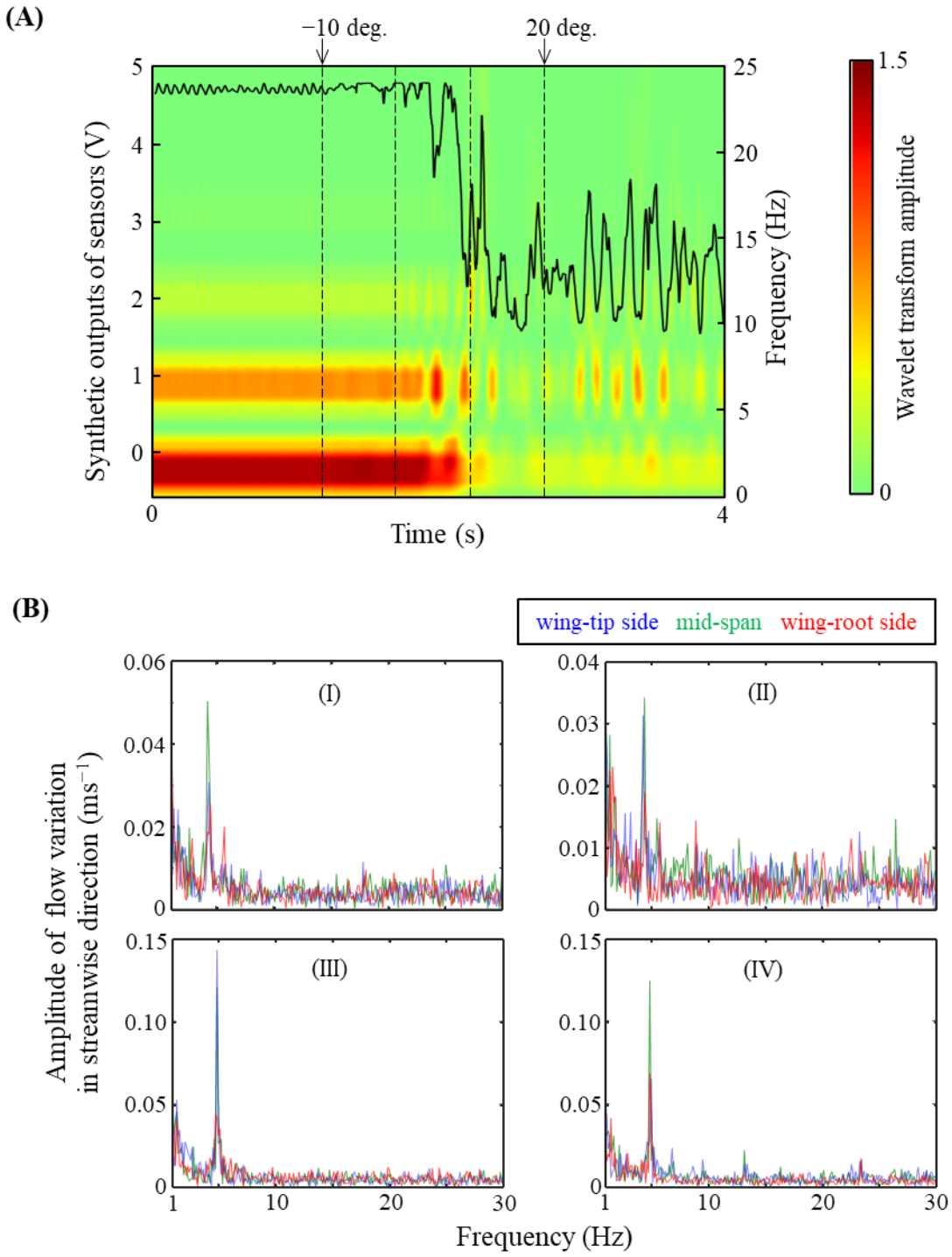

Fig. 3.16 Wavelet transform of the dynamic responses of the hall-effect-type sensors presented in Fig. 3.14(B). (B) FFT analysis of flow vibration in the streamwise direction measured by hot-wire anemometer (I) at 25 % chord from leading edge in 8 ms^{-1}, (II) at 60 % chord in 8 ms^{-1}, (III) at 25 % chord in 10 ms^{-1}, and (IV) at 60 % chord in 10 ms^{-1}. Color of the legends means the position of the hot-wire probe (see Fig. 3.8(C)).

Table 3.1 Specifications of hall-effect-type sensors

Sensor names	Length (mm)	Width (mm)
Sens1	50	10
Sens2	57	11
Sens3	64	13
Sens4	70	14
Sens5	77	15
Sens6	84	17
Sens7	90	18

Chapter 4

Design and fabrication of a bird-inspired flying robot

4.1 Introduction

The ability of birds to transform their bodies, called morphing, is considered to play an important role in their exceptional flight capabilities. Unpredictable winds originating from atmospheric boundary layer affect the stability of flying objects, such as birds and drones (Watkins et al., 2020). Active morphing of bird can be useful for enhancement of maneuverable flight such as rapid turn and dive, while morphing may also work well in situations in which a flying robot try to overcome the effects of disturbances such as gust wind through active attitude changes. As exemplified by the wind-hovering of the common kestrel observed by Videler et al. (1983), it is suggested that birds can fine-tune their body transformation to parry wind forces that cause them to lose their posture.

There are some examples of bird-based flying robots that were developed inspired by morphing in previous studies. As introduced in Subsection 1.3.1, some types of morphing wing MAVs were developed by Ajanic et al. (2020), Chang et al. (2020), and Luca et al. (2017). Their studies have highlighted that the wing morphing can improve the flying robot's maneuverability like a bird. However, these previous studies have mainly focused on improving active maneuverability, while there are few studies on improving flight stability through fine morphing control, such as the forementioned birds parry the effects of the wind.

In this study, a bird-inspired flying robot with multiple degrees of freedom in wing and tail was designed and fabricated. The robot' wing was designed to be equipped with the feather-based airflow

sensors developed in Chapter 3. In this chapter, the details of the design and fabrication of the robot are introduced.

4.2 Materials and methods

4.2.1 Overview of the robot design and configurations

A bird-inspired flying robot (Fig. 4.1(A)) was fabricated. Basic design parameters such as size and weight of the robot was determined with reference to the common kestrel (*Falco tinnunculus*) (Videler, 2006). Specifications of the robot are summarized in Table 4.1. This robot was composed of three main parts: central body, flapping wings, and morphing tail. There were eight servo motors in total that actuate wings and tail (Fig. 4.1(B)). Main frame of the central body mounted five servo motors (Fig. 4.1(C)). Four of them were used for control left and right wings. The other one was base of tail parts and actuated its tilt motions. Main frame and servo motors were covered by external shells to form smooth body surface.

Position of the robot's center of gravity was shown in (Fig. 4.2). located between the wings and tail along anteroposterior direction. Center of gravity was located at midway between the wing and tail (Fig. 4.2(A)), and at approximately middle of the lateral and dorsoventral directions (Figs. 4.2(B) and 4.2(C)).

4.2.2 Wing mechanism

Wing design (Figs. 4.3(A), 4.3(B), 4.3(C), and 4.3(D)) were determined by estimating the required lift force that can support a weight of 100 g per single wing, referring to the shape and size of the kestrel. Single wing had Clark-Y airfoil, half spanwise length of 250 mm, and mean chordwise length of 100 mm, resulting in the half wing area was 25,000 mm^2. Total wingspan length was 600 mm and the aspect ratio was approximately 5. The wing's tapered ratio was 0.5, the sweep angle was 0 °, and the twist angle in the spanwise direction was also 0 °. The wing was attached to the feathering-control servo motor by wing root joint at 25 % from the leading edge.

The wing was made of two primary materials: 3D-printed polylactide (PLA) plastic and thin polypropylene (PP) plastic sheets. In order to make the robot lighter, the wing was composed of spanwise beams and chordwise spars while the interior of the wing was hollowed out. External frames

were printed by 3D-printer (Ultimaker 3 Extended, Ultimake BV) with XY positioning accuracy of 12.5 μm and Z positioning accuracy of 2.5 μm. In order to form a smooth wing surface, thin and flexible PP sheets were cut into seven strips and were taped to cover the hollow wing (Fig. 4.3(A)).

Each wing was actuated by two servo motors and had two degrees of freedom based on the positional and feathering motions (Figs. 4.4(A) and 4.4(B)). Positional angles were changed by a servomotor (HS-81, Hitec Multiplex Japan Inc.) shown as yellow parts in Figs. 4.1(C), and feathering angles were changed by another servomotor (SG-90, Umemoto LLC) shown as gray parts in Figs. 4.1(C). The control mechanism of positional angle and feathering angle was illustrated in Fig. 4.5. Positional-control servo motor was mounted on the central frame. Feathering-control servo motor and wing were jointed to the positional-control servo motor.

4.2.3 Tail mechanism

Tail was designed with reference to the kestrel's parameter (Videler, 2006) and flying robots with morphing tail previously developed (Ajanic et al., 2020; Chang and Lentink, 2020; Nickols and Lin, 2017; Parga et al., 2007). Tail had the three degrees of freedom based on the tilt, elevation, and rudder angle relative to the body (Figs. 4.6(A), 4.6(B), and 4.6(C)). There were four servo motors (HS-40, Hitec Multiplex Japan Inc.) that actuate the morphing tail. Servo motors operating the tilt, elevation, and rudder angles were arranged in series and connected by joint parts ($J_{t\text{-}e}$ and $J_{e\text{-}r}$ in Fig. 4.7(A)). Among the four servo motors, one was used for tilt control, another for elevation control, and the other two for rudder control. The dimensions of the tail and servo motors arrangement are shown in the Fig. 4.7(B). The distance between the tilt-control servo motor and the elevation-control servo motor was 29 mm, and the distance between the elevation-control servo motor and the rudder-control servo motors was 35 mm. Tail feathers with 100 mm length were actuated independently by two servo motors. The tail feathers were grouped into three parts: the left and right movable parts and the central fixed part (Fig. 4.7(C)). Tail feathers and joint parts were also printed by the 3D-printer. As shown in Fig. 4.7(C), tail feathers with only frames were covered with polyamide sheets to form a membrane.

The morphing tail assembly, consisted of three major compartments, is described in detail here. Tilt-control servo motor (red parts in Fig. 4.8(A)) was root of the morphing tail and was mounted to the central body frame. A joint component ($J_{t\text{-}e}$) was connected to the tilt-control servo motor. Elevation-

control servo motor was mounted to the $J_{t\text{-}e}$, and another joint component ($J_{e\text{-}r}$) was connected to the elevation-control servo motor (blue parts in Fig. 4.8(B)). Two rudder-control servo motors were mounted to the $J_{e\text{-}r}$, and an outer side tail feather was connected to the rudder-control servo motor (green parts in Fig. 4.8(C)). The movable tail feathers, including the central fixed feather, had layered storage design and cloud be tucked or spread them.

4.3 Discussion

Bird-inspired robot, which has two degrees of freedom in wing for feathering and positional control and three degrees of freedom in tail for tilt, elevation, and rudder control, was designed and fabricated. It was achieved that the size and weight of the robot were approximately the same as those of the kestrel used for reference. However, because a simple wing was preferred for mounting the feather-based airflow sensor developed in Chapter 3, the mechanism for changing the wing area, such as a sweep motion, as seen in real birds and morphing wing robots ever developed (e. g., Ajanic et al., 2020; Luca et al., 2017), was omitted.

For example, experimentally emulating kestrel's wind-hovering flight observed by Videler et al. (1983) requires an upward inclined flow, which will be realized in the robot by the balance between gravity and the aerodynamic forces on the wings, tail, and body (Fig. 4.9(A)). The robot with multi degrees of freedom in controlling aerodynamic forces actively fine-tune aerodynamic moments (Figs. 4.9(B), 4.9(C), and 4.9(D)) in response to wind variation data obtained from airflow sensors, and it may be able to achieve highly stable attitude control. In particular, the morphing tail is a mechanism for redundancy and fine-tunable aerodynamic control (Harvey et al., 2022), and it must play a significant role in maintaining a stable attitude. Experimental study on the effect of the morphing tail on aerodynamic performance is presented in detail in the following Chapter 5.

References

Ajanic, E., Feroskhan, M., Mintchev, S., Noca, F. and Floreano, D. (2020) Bioinspired wing and tail morphing extends drone flight capabilities. *Sci. Robot.* **5**, eabc2897, doi: 10.1126/scirobotics.abc2897.

Chang, E., Matloff, L. Y., Stowers, A. K., and Lentink, D. (2020) Soft biohybrid morphing wings with feathers underactuated by wrist and finger motion. *Sci. Robot.* **5**, eaay1246, doi: 10.1126/scirobotics.aay1246.

Harvey, C., Gamble, L. L., Bolander, C. R., Hunsaker, D. F., Joo, J. J. and Inman, D. J. (2022) A review of avian-inspired morphing for UAV flight control. *Prog. Aeosp. Sci.* **132**, 100825, doi: 10.1016/j.paerosci.2022.100825.

Luca, M. D., Mintchev, S., Heitz, G., Noca, F., and Floreano, D. (2017) Bioinspired morphing wings for extended flight envelope and roll control of small drones. *Interface Focus* **7**, 20160092, doi: 10.1098/rsfs.2016.0092.

Nickols, F. and Lin, Y. J. (2017) Feathered tail and pygostyle for the flying control of a bio-mimicking eagle bird robot. *Proceedings of 2017 IEEE 8th International Conference on Cybernetics and Intelligent Systems and Robotics, Automation and Mechatronics*, 556-561, doi: 10.1109/ICCIS.2017.8274837.

Videler, J. J. (2006) *Avian flight*, Oxford scholarship online, doi: 10.1093/acprof:oso/9780199299928.001.0001.

Videler, J. J., Weihs, D. and Daan, S. (1983) Intermittent gliding in hunting flight of the Kestrel, *Falco tinnunculus* L. *J. Exp. Biol.* **102**, 1-12, doi: 10.1242/jeb.102.1.1.

Watkins, S., Burry, J., Mohamed, A., Marino, M., Prudden, S., Fisher, A., Kloet, N., Jakobi, T., and Clothier, R. (2020) Ten questions concerning the use of drones in urban environments. *Build. Environ.***167**, 106458, doi: 10.1016/j.buildenv.2019.106458.

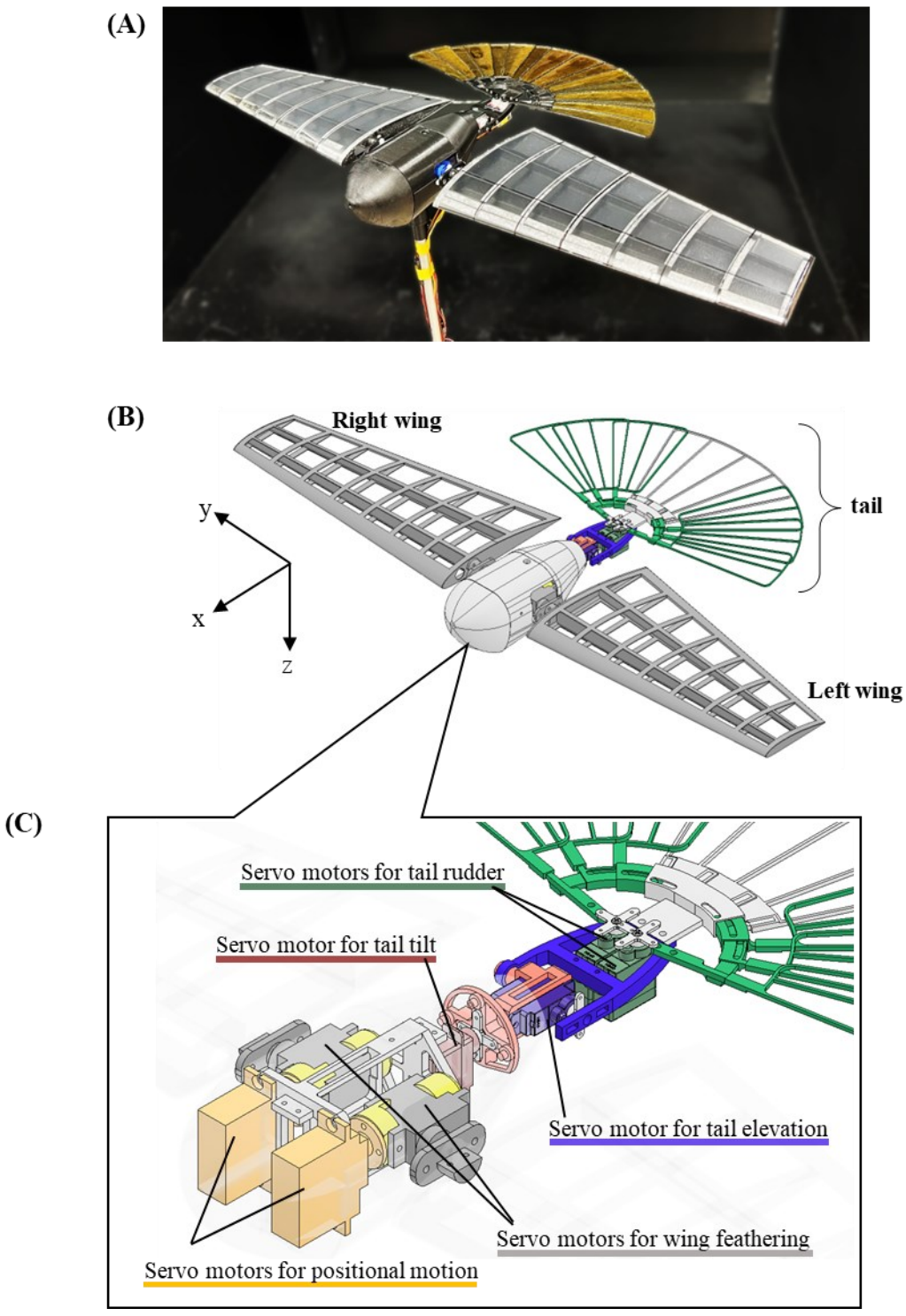

Fig. 4.1 (A) Appearance of the manufactured bird-inspired robot. (B) 3D-CAD design of the robot viewed from the diagonal-forward-left angle. (C) Arrangements of servo motors to actuate the wings and tail in the external covers.

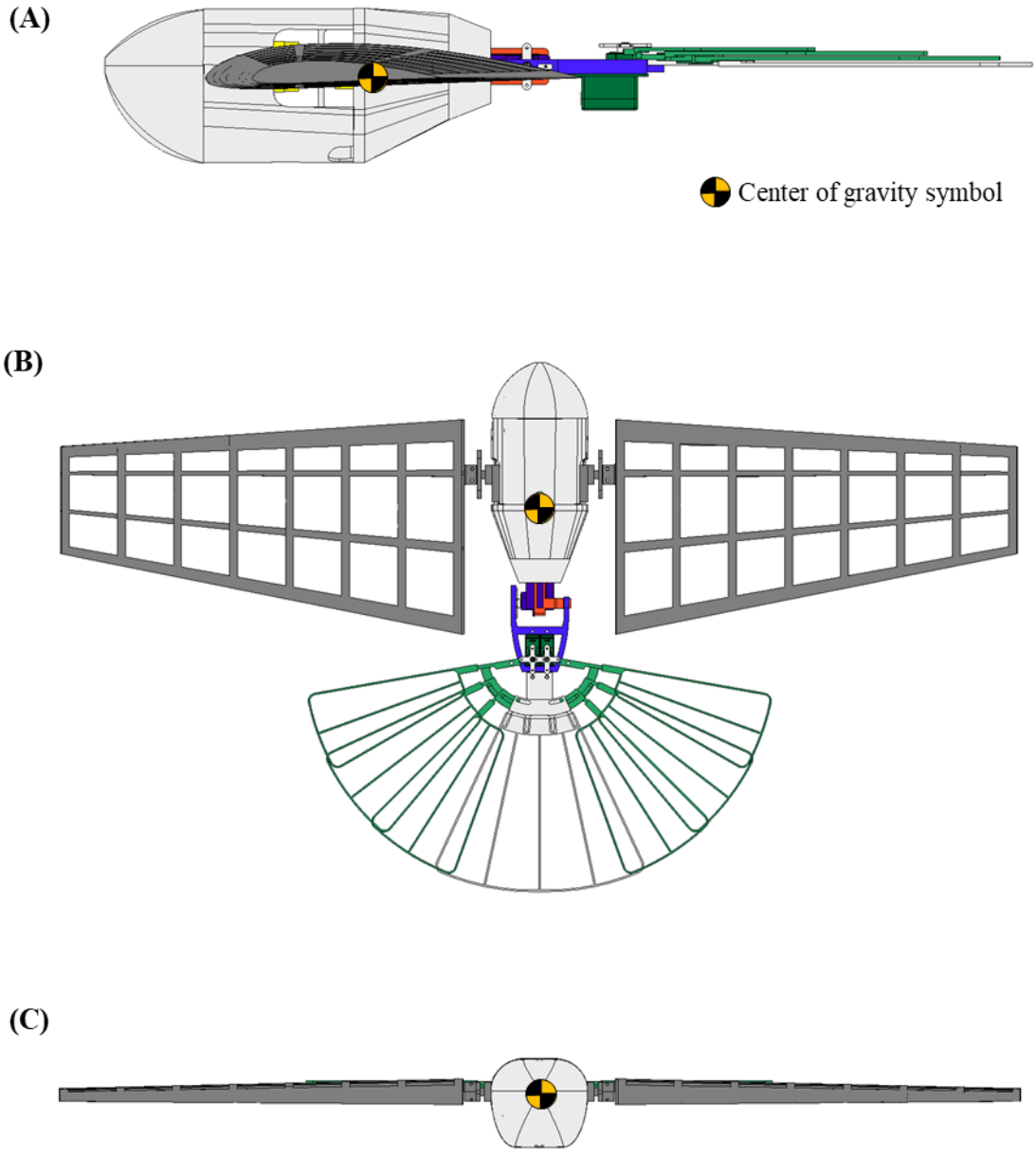

Fig. 4.2 Position of the robot's center of gravity viewed from (A) left side angle, (B) dorsal angle, and (C) front angle.

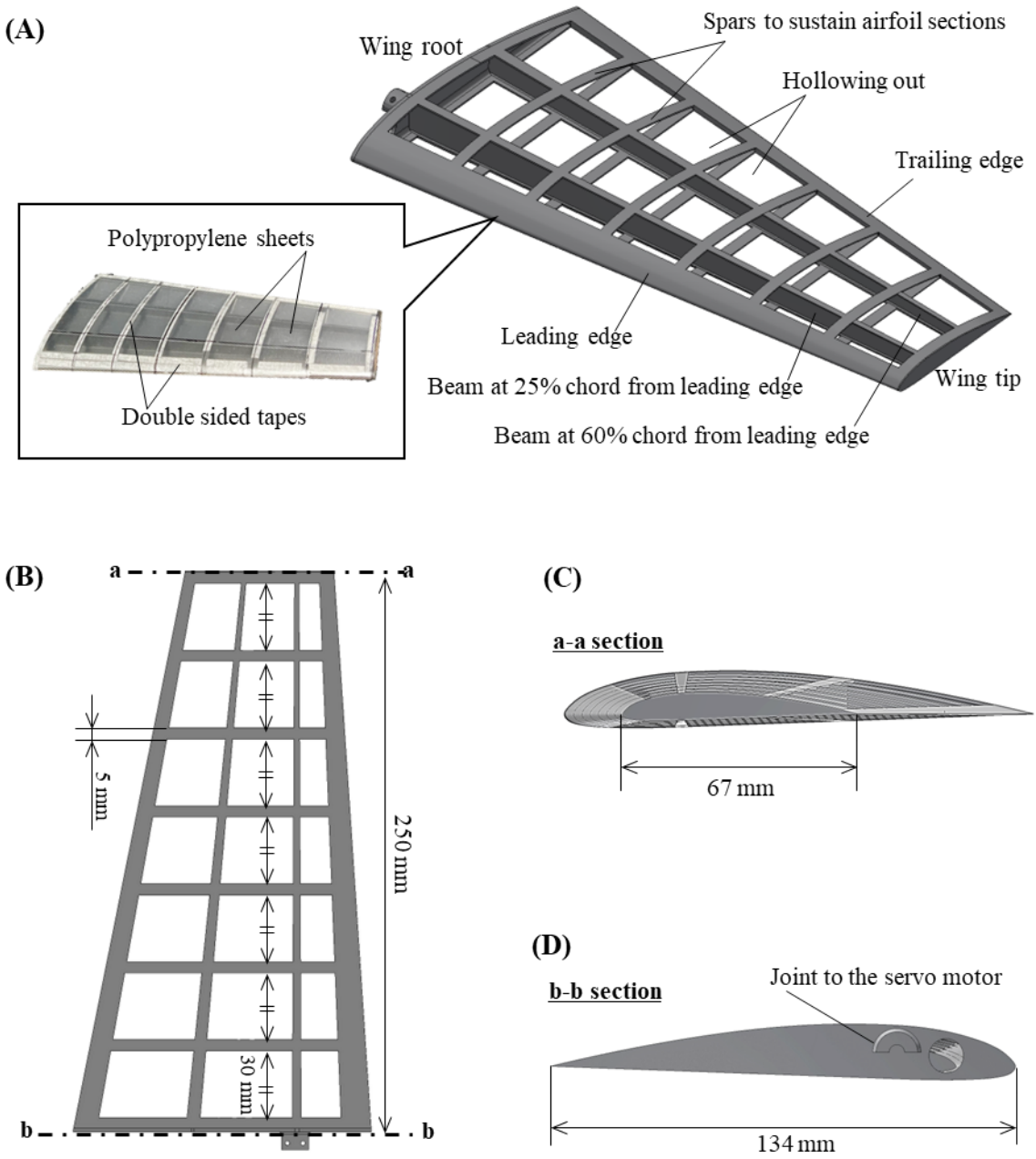

Fig. 4.3 Schematic diagram of left wing viewed from (A) the diagonal-forward-left angle, (B) the dorsal angle, (C) the distal side angle, and (D) proximal side angle.

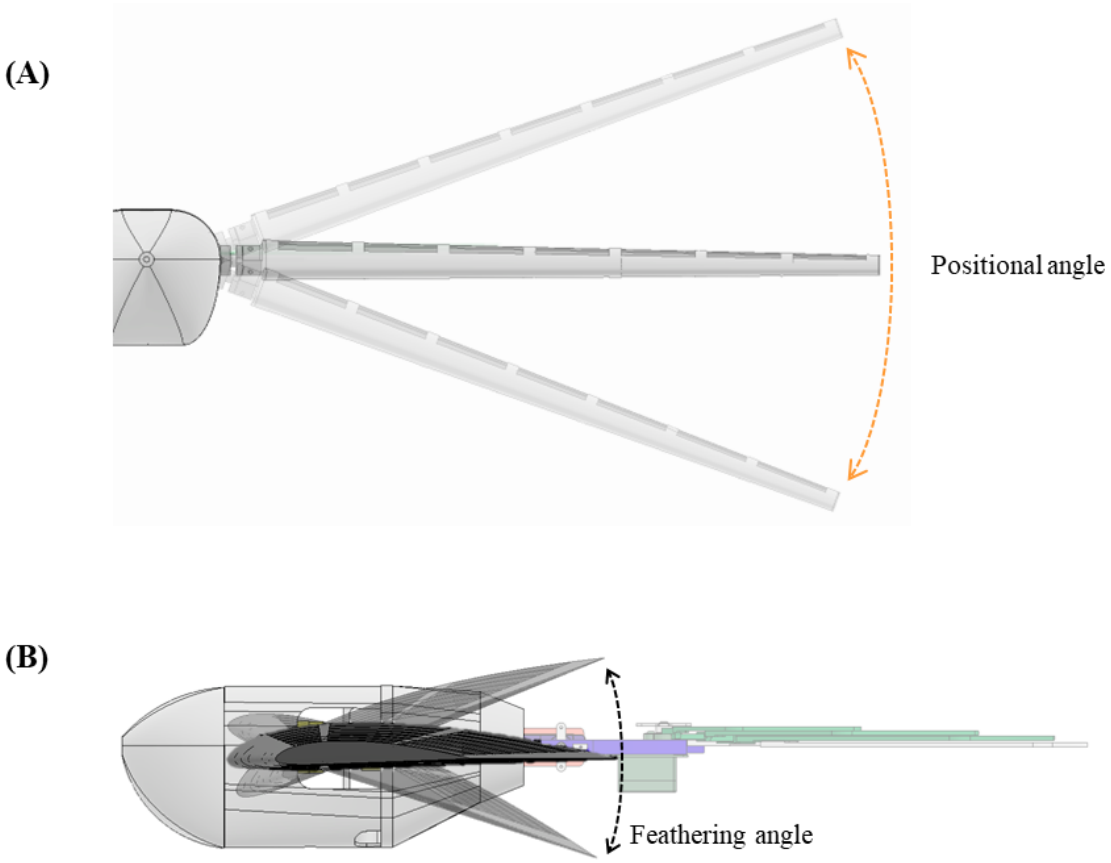

Fig. 4.4 Schematic diagram of wing motions. (A) Changes in positional angle (flapping motion) viewed from the front angle. (B) Changes in feathering angle viewed from the side angle.

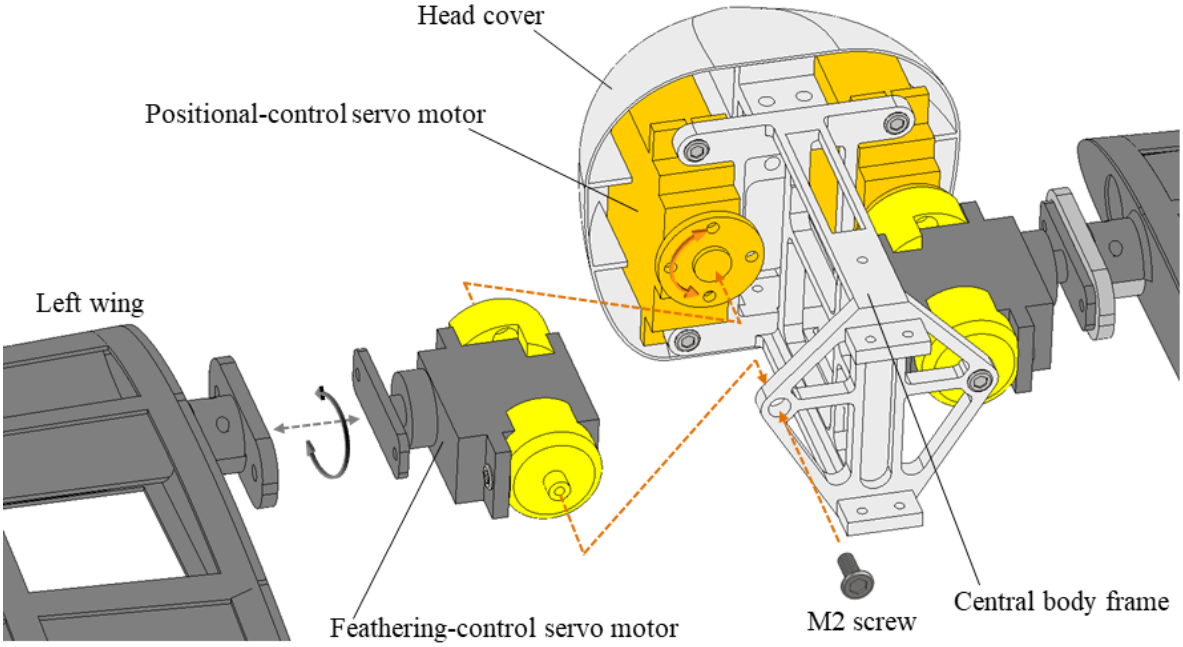

Fig. 4.5 Schematic diagram of the wing actuation mechanism assembly.

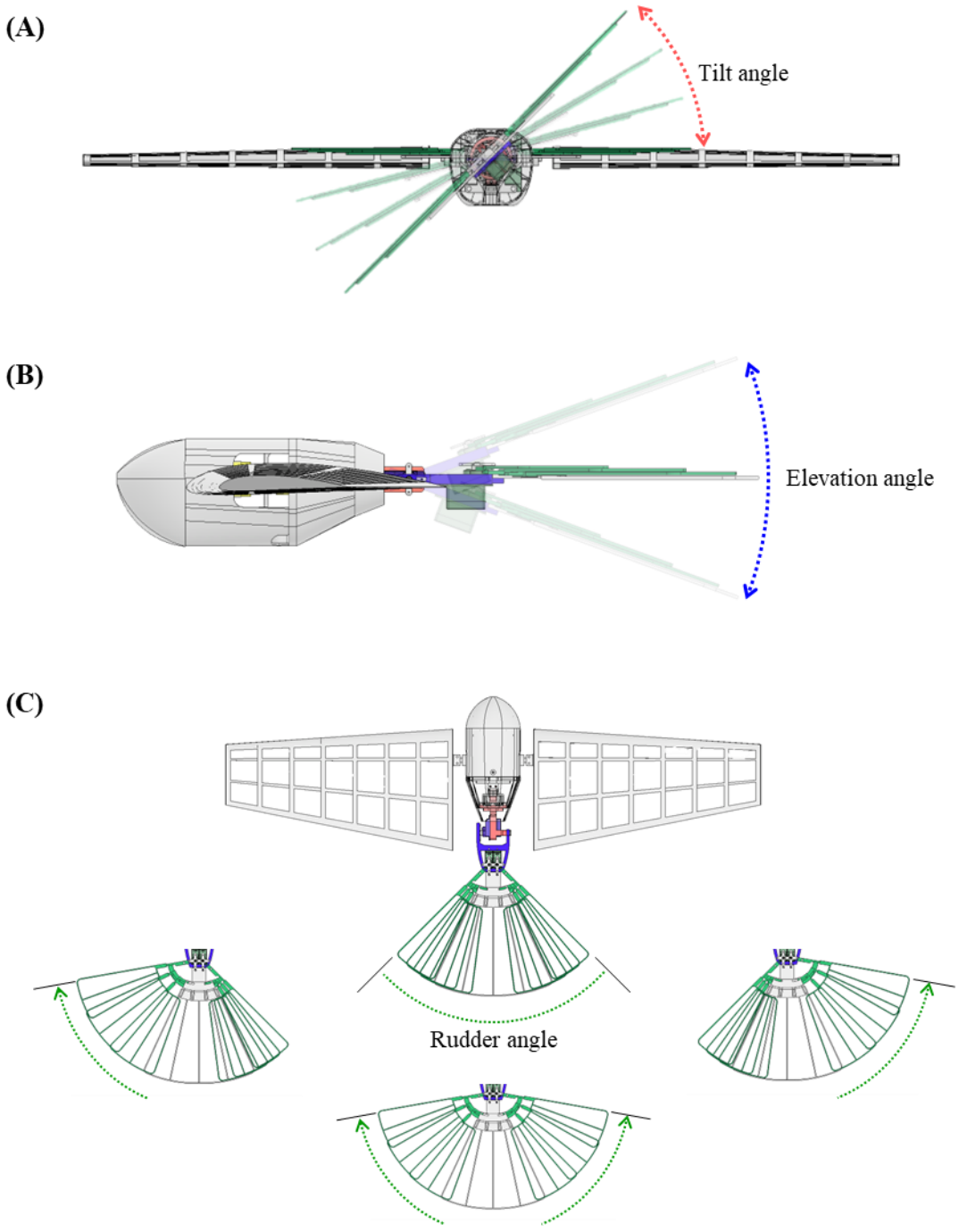

Fig. 4.6 Schematic diagram of the tail motions. (A) Tilt motions viewed from the behind angle. (B) Elevating motions viewed from the side angle. (C) Rudder motions viewed from the dorsal angle.

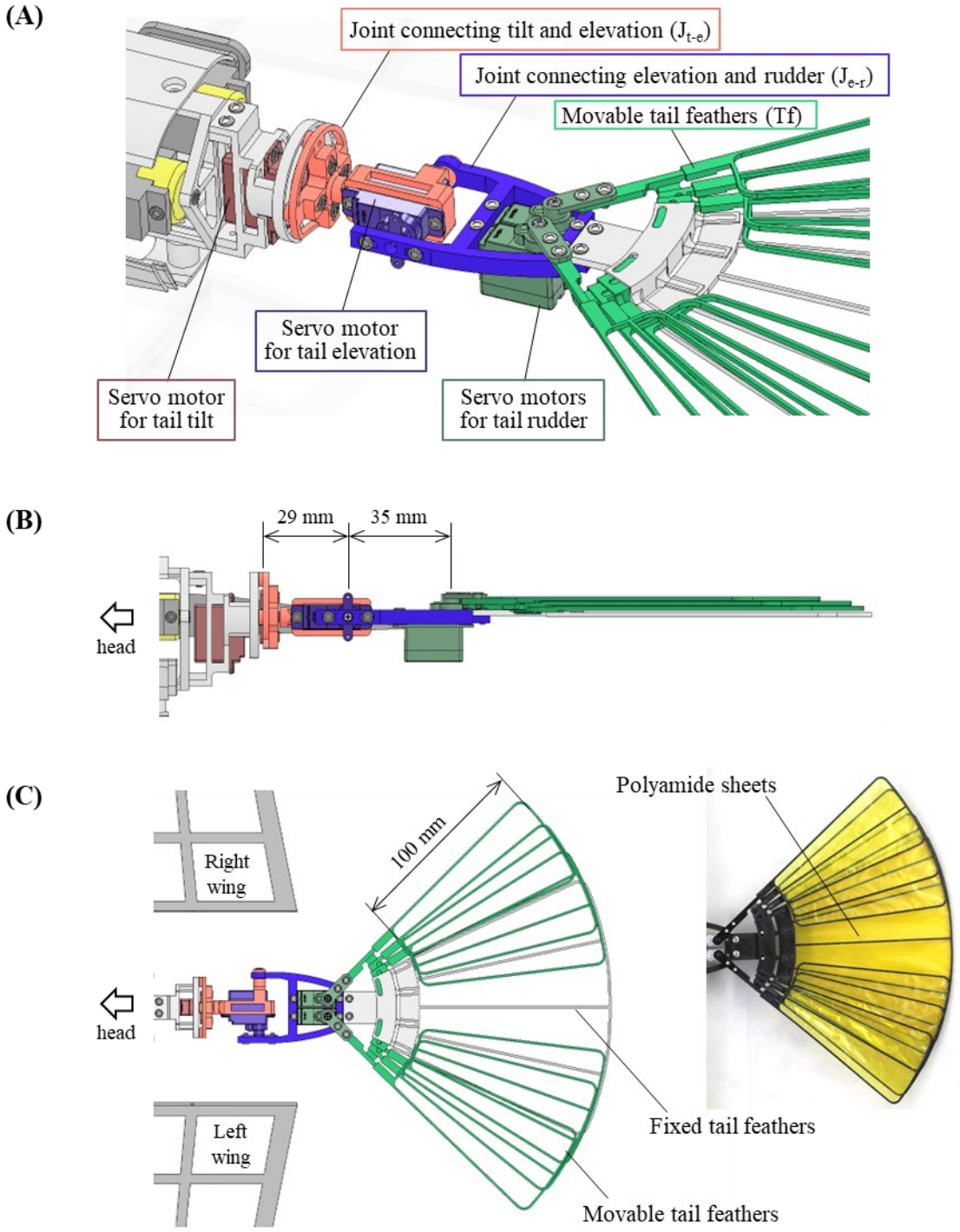

Fig. 4.7 Schematic diagram of the morphing tail. (A) Arrangement of actuators and joint parts that change the tail postures viewed from (A) the diagonal-backward-left angle, (B) the side angle, and (C) the dorsal angle.

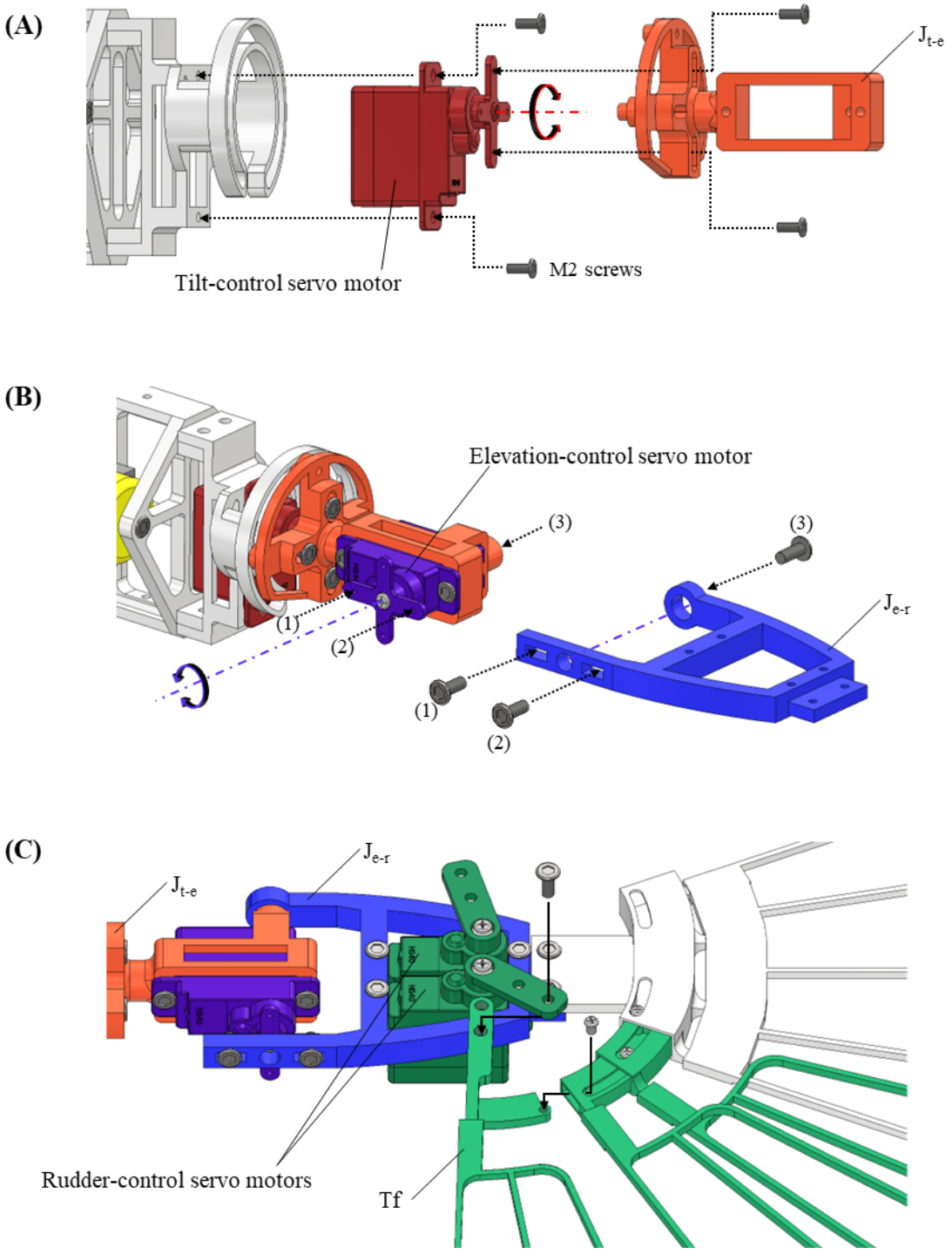

Fig. 4.8 Schematic diagram of the morphing tail mechanism assembly. (A) Tilt, (B) elevation, and (C) rudder mechanisms viewed from the left angle.

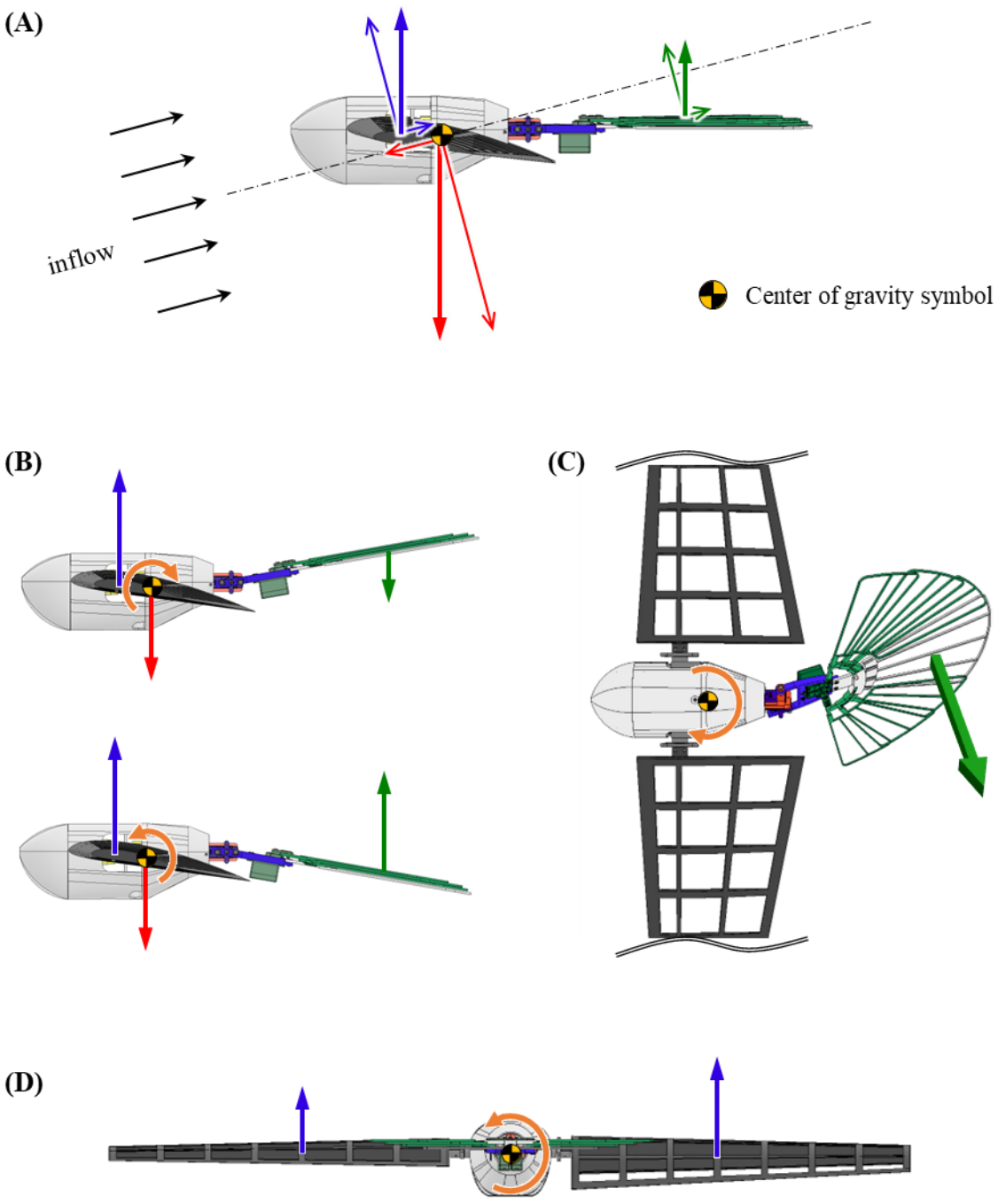

Fig. 4.9 Schematic diagram of aerodynamic forces and moments on the bird-inspired robot. (A) Force balancing in an upward inclined flow. Adjustment of (B) pitch moment, (C) yaw moment, and (D) roll moment by attitude changes in wings and tail.

Table 4.1 Specifications of the bird-inspired robot

Dimensions	Symbol	Units	Value
Wing airfoil	–	–	Clark-Y
Wingspan (half)	b_h	m	0.25
Wingspan (total)	b	m	0.60
Projected wing area (total)	S_w	m^2	0.05
Mean wing chord	c	m	0.10
Wing aspect ratio	AR	-	5
Wing taper ratio	TR	-	0.5
Wing sweep angle	–	°	0
Wing twist angle	–	°	0
Total mass of the robot	m	g	198
Moment of inertia around x-axis at center of gravity	I_x	$g \cdot mm^2$	1.24×10^6
Moment of inertia around y-axis at center of gravity	I_y	$g \cdot mm^2$	0.57×10^6
Moment of inertia around z-axis at center of gravity	I_z	$g \cdot mm^2$	1.78×10^6

Chapter 5

Aerodynamic performance of a bird-inspired morphing tail

5.1 Introduction

Flyers such as birds and drones are affected by unpredictable winds originating from the atmospheric boundary layer (Watkins et al., 2020). Wind disturbances pose a challenging problem for drones. In contrast, birds are equipped with functions to achieve stable flight in unpredictable winds based on long-term evolution. They have enriched sensory organs called mechanoreceptors in their bodies and are able to detect changes in wind speed and pressure using these organs to react to disturbances (Brown and Fedde, 1993; Xu et al., 2014). For example, Altshuler et al. (2014) described the function of mechanoreceptors that slowly adapting receptors like Merkel cells and Ruffini endings sense the forces that sustain the deformation of feathers and skin, such as wind speed and stall (Necker 1985), whereas vibration receptors like Herbst corpuscles function to discriminate the high-frequency elements of flow disturbances (Hörster 1990). Besides, it has been observed that a common kestrel can hover at a point in strong wind, called wind-hovering, by adjusting the attitude of its wings and tail (Videler et al., 1983). In addition to their superior vision and equilibrium organs, such birds' advanced flight techniques seem to be aided by their sensory organs that are sensitive to the airflow variations. Remarkable flight capabilities such as wind-hovering and long-distance migration can inspire the design of drones that can fly more efficiently.

Birds have a variety of flight modes that are used in different scenarios, including flapping, gliding, and soaring. Flapping is common among all birds and the flapping motion generates the thrust and lift

forces required for flight by moving the wings up and down while properly adjusting the lead-lag, feathering angle, and stroke plane angle (Videler, 2006). Larger species are more likely to perform gliding and soaring flights more frequently because their heavier weights require a large amount of energy for flapping (Williams et al., 2020). Gliding flight is a method for efficiently traveling long distances by converting the sinking velocity gained with altitude loss into forward speed and lift force. Soaring flight is a type of gliding performed by capturing updraft wind, which makes it possible to fly for a long time or gain altitude without flapping. Not limited to updrafts, some sea birds show another soaring technique, called dynamic soaring, in which they can continue to fly by gaining energy from horizontal winds, such as shear winds above the sea surface (Sachs, 2005). It is thought that birds fly by appropriately switching between these flight modes and adjusting the balance between efficiency and maneuverability. To flap their wings and maintain balance while flying in complex winds, birds have the ability to transform their body shapes, which is known as morphing. The avian body is covered by a large number of feathers that form smooth body surfaces during morphing. It has been reported that the morphing function of avian wings is crucial to their aerodynamic performance (Harvey et al., 2022).

The tail and its morphing mechanism, in conjunction with the morphing of wings, are unique features of birds. The tail is actuated independently of the main wings (Gatesy and Dial, 1993). It is thought to provide benefits in terms of the aerodynamic efficiency, controllability, and stability during flight (Balmford, 1993; Sachs, 2007; Thomas, 1993a, 1993b, 1996a, 1996b). It has been observed that a large soaring bird constantly uses the movement of its tail for turning maneuvers (Gillies et al., 2011). The remarkable mechanism of bird morphing has inspired ideas that facilitate the development and improvement of artificial flyers. Various types of flying robots modeled based on birds have been developed in previous studies (Folkertsma et al., 2017; Gerdes et al., 2014; Yang et al., 2018). For example, adding a morphing function to the wings of a bird-inspired aerial robot has been studied to improve maneuverability in terms of turning performance by asymmetrically changing the area of left and right wings to create an imbalance in lift force. (Luca et al., 2017). A micro air vehicle with a limited two-degree-of-freedom tail mechanism has also been proposed (Parga et al., 2007). However, examples of models developed with morphing tail mechanisms are limited (Ajanic et al., 2020; Chang and Lentink, 2019; Nickols and Lin, 2017) and knowledge of how well a morphing tail extends the envelope of an actual flight robot has not yet been acquired.

In this study, mainly aiming to elucidate the mechanism of attitude control by birds using the tail, we investigated the role of tail attitude in the flight performance of a bird-inspired aerial robot by fabricating a morphing tail inspired by avian tail feathers and evaluating its aerodynamic characteristics. The three components of the aerodynamic forces and moments along each axis were measured using a six-axes force sensor in a wind tunnel while the attitude of the tail was varied in terms of the tilt, elevation, and rudder angles relative to the body.

5.2 Materials and methods

5.2.1 Morphing tail mechanism for a bird-inspired robot

A tail mechanism inspired by avian tail feathers was fabricated for a bird-inspired flying robot, as presented in Subsection 4.2.3. The tail mechanism has three degrees of freedom based on the tilt, elevation, and rudder angle relative to the body (Fig. 5.1). Each tail angle is independently actuated using a micro servo motor (HS-40, Hitec Multiplex Japan Inc.) with a driving controller (Arduino Uno). A tilt-control servo motor is mounted on the rear side of the main body (red parts in Fig. 5.1(B)), behind which the servo motor for elevation-control is connected (blue parts in Fig. 5.1(B)). The two servo motors that control the rudder of the tail feathers are located at the rear end (green parts in Fig. 5.1(B)). This rudder-control mechanism replicates the yaw shift of a bird's tail by independently spreading or narrowing both sides of the feathers proximally. The artificial tail feathers were designed to spread in a fan form, where each feather consisted of a 3D-printed PLA frame and polyamide membrane. Each tail feather overlaps, forming a complete tail with a spread angle of 160 ° when fully spread and 80 ° when minimally furled. The specifications of the morphing tail mechanism, which were determined by referring to the size of a kestrel (Videler, 2006), are listed in Table 5.1.

5.2.2 Wind tunnel experiments

The aerodynamic forces of the robot were measured by a six-axis force sensor (PFS020YA500G6, Leptrino Inc.) in a wind tunnel to evaluate its aerodynamic performance (Figs. 5.2(A) and 5.2(B)). The voltage values of the force sensor were amplified and logged by a PC through an A/D converter (NI-

9205, National Instruments Corp.). Measurements were performed twice for 5 s at a sampling rate of 1,000 Hz.

These experiments were conducted in a closed-loop wind tunnel at Chiba University (Ikeda et al., 2018), which has a test volume of $1.0 \times 1.0 \times 2.0$ m. The robot was placed in the center behind the opening of the wind tunnel (Figs. 5.2(A) and 5.2(B)). The nose of the robot faced the direction of the inflow and the body was oriented horizontally. To generate a lift force sufficient to support the weight of the robot (198 g), the angle of incidence of the main wings was set to 7 ° and the wind speed (U) was set to 9 ms^{-1}. Measurements were conducted with the main wings passively deflected upward by the lift force with the dihedral of an approximately 6 ° (Fig. 5.3(B)).

The effects of the tail attitude on the aerodynamic performance for several different attitudes were studied (Table 5.2). The actual angle of the deflected tail in the flow was measured using a camera (D5300, Nikon Corp.). The motion ranges listed in Table 5.2 are the results of considering the limits of the actuating performance of the servo motor under aerodynamic forces. Actual views of changes in the elevation, tilt, and rudder angle of the tail during the experiments are presented in Figs. 5.3(A), 5.3(B), and 5.3(C), respectively.

The forces and moments measured by the sensor were converted into aerodynamic forces (lift, drag, and lateral forces) and moments (pitch, roll, and yaw moments), respectively, based on the axes defined in Fig. 5.1(A). The positive direction of drag force is along the flow, and the positive direction of lift force is perpendicular to the drag force and upward of the robot. The positive direction of the lateral force is toward the right when the robot is viewed from the rear. The dimensionless coefficients were then calculated using Eqs. (1), (2), and (3), where, ρ is the air density and S_w is the total area of the main wings. The mean chord length of the wing c was used as the reference length to calculate the pitch moment coefficients in Eq. (4), and spanwise length of the wing b was used as the reference length to calculate the roll and yaw moment coefficient in Eqs. (5) and (6). Additionally, the lift/drag ratio (L/D), which is related to efficiency, was calculated from the lift and drag forces.

$$\text{Lift coefficient} = \frac{2\ \text{Lift}}{\rho U^2 S_w} \tag{5.1}$$

$$\text{Drag coefficient} = \frac{2\ \text{Drag}}{\rho U^2 S_w} \tag{5.2}$$

$$\text{Lateral coefficient} = \frac{2\ \text{Lateral}}{\rho U^2 S_w} \tag{5.3}$$

$$\text{Pitch moment coefficient} = \frac{2\ \text{Pitch}}{\rho U^2 S_w c} \tag{5.4}$$

$$\text{Roll moment coefficient} = \frac{2\ \text{Roll}}{\rho U^2 S_w b} \tag{5.5}$$

$$\text{Yaw moment coefficient} = \frac{2\ \text{Yaw}}{\rho U^2 S_w b} \tag{5.6}$$

5.3 Result

5.3.1 Aerodynamic force and efficiency

It was found that the L/D, i.e., the flight efficiency of the robot, was adjusted by controlling the elevation angle of the tail (Figs. 5.4(A) and 5.4(B)). Moving the tail downward increased the L/D as a result of increased lift force (Fig. 5.5(A)). In contrast, moving the tail upward resulted in smaller lift and greater drag, resulting in lower efficiency (Figs. 5.5(A) and 5.6(A)). A similar trend was observed when the area of the tail was changed or when the tail feathers were shifted to the right side (Figs. 5.4(B), 5.5(B), and 5.6(B)). However, efficiency began to decrease above a certain elevation angle (Figs. 5.4(A) and 5.4(B)) because the rate of increase in drag exceeded the rate of lift (Figs. 5.5(A), 5.5(B), 5.6(A), and 5.6(B)).

It was also observed that changes in the tilt angle of the tail while maintaining a downward elevation could generate a lateral force in the yaw direction while maintaining a high L/D (Fig. 5.4(C)). Conversely, L/D remained consistently low for upward elevation of the tail, regardless of changes in the tilt angle. In both cases of up and down tail elevation, the changes in efficiency with the variation of the tilt angle were marginal. This is because the lift and drag forces do not change with a change in the tilt angle (Figs. 5.5(C) and 5.6(C)). However, the absolute values of the lateral force increase linearly according to changes in the tilt angle (Fig. 5.7(C)). This means that changing the tilt angle can control yawing without affecting efficiency.

Some curves of the aerodynamic forces according to changes in the elevation and tilt angles exhibited

asymmetry with respect to the reference angle of 0 ° (e.g., Figs. 5.5(A), 5.6(B), and 5.7(C)), which can be attributed to the influence of the wake generated by the supporting column to fix the robot with the force sensor, as shown in Fig. 5.3(A). Additionally, because the tail is affected by the downwash of the wings (Fig. 5.3(B)), the interaction between the wings and tail may have affected the aerodynamic performance of the robot.

5.3.2 Aerodynamic moments

Pitch moment

The elevation of the tail controls the pitch moment relative to the vertical direction of the head of the robot. When the elevation angle of the tail is between −5° and 0° (slightly upward or nearly horizontal), the pitch moment is small (Fig. 5.8(A)). Bending the tail downward outside this range causes a monotonic increase in the negative pitch moment, which induces the head to move downward. Conversely, bending the tail upward increases the positive pitch moment due to the large negative lift generated by the tail behind the body, which causes the head to move upward. The effect of the tail on the pitch moment is more evident for a larger tail area (Fig. 5.8(A)). For example, if a wind disturbance such as a gust increases the lift produced by the wings and increases the positive pitch moment, which may cause a stalling due to head-up, the negative pitch moment obtained by manipulating the elevation angle of the tail can help to recover the attitude.

It was also found that the pitch moment does not change significantly with respect to the change in tilt angle (Fig. 5.8(B)). Tilting the tail generates a lateral force, but the changes in the lift acting on the pitch moment are small. Even for changes in the rudder angle of the tail with the same tail area, the pitch moment curves exhibit a similar trend. This indicates that rudder control does not contribute to generating the pitch moment.

Roll moment

The roll moment is generated either by attitude changes with a combination of rudder and elevation or by a combination of tilt and elevation. The variation rate of the roll moment with changes in the elevation angle increases when the bias of the tail rudder angle is greater (Fig. 5.9(A)). It was also

confirmed that the roll moment was changed with the tilt of the tail (Fig. 5.9(B)). However, the amount of roll moment generated by the tail is limited compared to the pitch moment because the length of roll moment arm around roll axis from the tail is expected to be shorter than that of pitch moment arm around pitch axis.

These results are similar to those of the Rudder-R60L60 with the maximum and minimum tail areas. Changing the tail area does not affect the roll moment curve with respect to the elevation change. Therefore, the results of Rudder-R80L80 and R40L40 are omitted from Fig. 5.9(A). The roll moment is not equal to zero at an elevation angle of 0 ° possibly due to the slight difference in the angle of attack between the left and right wings. Therefore, it should be considered that the effect of the tail on the roll moment (Fig. 5.9) includes a slight positive offset.

Yaw moment

One approach to change the yaw moment is to change the rudder angle of the tail with a bias to the right or left. It was determined that the yaw moment changes when the rudder angle of the tail is gradually deflected to the right side while maintaining the same wing area of the tail (Fig. 5.10(A)). Despite having the same tail area, the yaw moment almost doubles when the tail is biased by 10 ° to the right (Rudder-R70L50 to R80L40) with the tail pointing 15 ° downward. A yaw moment is obtained only when the elevation angle of the tail is either downward or upward. When the tail feathers are approximately horizontal, the tail area projected on the plane which is perpendicular to the inflow is small, thus a lateral and drag force which generate yaw moment are not obtained.

Another approach to control the yaw moment is to change the tilt angle of the tail. It was determined that a greater lateral force and yaw moment can be obtained by increasing the tilt angle, rather than biasing the tail rudder (Figs. 5.10(A) and 5.10(B)). For instance, a slight tilt angle of approximately 10 ° provides a yaw moment equivalent to that when the rudder angle of the tail is fully shifted to the right. However, the tilt movement of the tail also generates roll and pitch moments simultaneously, even though the rate of change is low (Figs. 5.8(B), 5.9(B), and 5.10(B)).

Just as in the case of the roll moment, changing the tail area has little effect on the yaw moment with respect to the elevation change. The results for Rudder-R80L80 and R40L40 are similar to the yaw moment curve for Rudder-R60L60. Therefore, they are omitted from Fig. 5.10(A).

5.4 Discussion

In this study, the aerodynamic forces on a bird-inspired robot were measured to evaluate the role of attitude changes in the tail during flight. It was experimentally confirmed that flight efficiency and controllability can be improved by changing the attitude of the tail. It was also determined that there is redundancy in how the tail generates aerodynamic moments associated with roll, pitch, and yaw control. Here, discussion of the applicability of the proposed tail to a flying robot are presented with references to previous studies.

First, differences between the morphing of a real bird tail and the artificial tail fabricated in this study should be considered. Real birds change their tail shape by spreading or narrowing tail feathers. The number of tail feathers varies between species. For example, pigeons and kestrels have 12 tail feathers, whereas turkeys have 18 (Gatesy and Dial, 1996). The two central feathers are directly connected to the pygostyle and the other feathers on each side are spread or narrowed (Gatesy and Dial, 1996). These tail components are controlled by muscles and are functionally decoupled from the rest of the trunk and hind limbs (Gatesy and Dial, 1993). Our morphing tail mechanism was fabricated by imitating the fixed central feather and moving feathers on both sides of a bird tail. This mechanism can change the shape of the tail in a fan shape with only six feathers, that are fewer than the tail feathers of a real bird. Unlike the complex musculoskeletal actuation of birds' tail, our tail mechanism is directly driven by four micro servo motors to reproduce the three-degrees-of-freedom posture changes of the tail similar to that of a bird. However, our current mechanism cannot furl the tail feathers into a smaller shape as seen in real birds, and improving the design to achieve this is a task to be tackled in the future study.

It was demonstrated that a combination of an adequate elevation angle of the tail and its area results in greater efficiency. Variable lift and drag forces based on tail elevation, which affect efficiency, were confirmed in this study, and noted in a previous study (Ajanic et al., 2020, Parga et al., 2007). Greater tail elevation angles do not necessarily lead to higher efficiencies because the elevation angles must remain within an appropriate range. Therefore, our experimental findings indicate that it is not necessary to vary the elevation angle of the tail significantly to enhance efficiency. The L/D with the tail fully spread was also relatively low based on a decrease in lift (Figs. 5.4(A) and 5.5(A)). Based on a study using a simple aerodynamic model, it was estimated that the power required for flight could be reduced

when flying at low speeds with the tail spread or at higher speeds with the tail narrowed (Thomas, 1996a). Following this logic, our experimental wind speed was relatively high and the L/D with the spread tail was worse than that with the furled tail, which is qualitatively consistent with the conclusion that it is more efficient to furl the tail. Our experimental L/D curves exhibited gaps between when the tail was fully spread and narrowed (hatched area in Fig. 5.4(A)), indicating that the tail has redundancy in terms of efficiency adjustment. Control of the tail area may be helpful when passing through narrow spaces, where it is difficult to elevate the tail significantly. Conversely, when L/D adjustment based on tail area control is weakened by damaged tail feathers, adjustment based on the elevation angle may be able to compensate for this effect. Therefore, redundancy in the function of adjusting flight efficiency by tail wing can help improve the reliability of flyers.

It was determined that the attitude change of the tail elevation angle is the most useful method for controlling the pitch movement of the bird-like robot, rather than changes in the tail shape (Fig. 5.8(A)). However, this result does not deny the potential benefits of pitch control based on changes in tail area, which is frequently performed by birds (Gillies et al., 2011). When switching the perspective to a robot configuration and considering the costs associated with tail movements, the moment of inertia must be considered because the actuation power of a small actuator that can be mounted on a bird-size robot is limited. The moment of inertia about the elevation axis of the tail is greater than that about the rudder axis (Table 5.1). Additionally, the elevating motion with a widely spread tail incurs additional costs based on fluid resistance. Controlling the rudder angle, which varies the tail area with a smaller moment of inertia at a given elevation angle, is thought to be a superior option for fine-tuning the pitch moment at a smaller cost.

In comparison to the pitch moment controlled by tail elevation, the roll moments controlled by the tail rudder and tilt movements were relatively minor (Figs. 5.9(A) and 5.9(B)). Considering the geometric arrangement of a bird's body, these results are reasonable because the roll moment can be controlled based on the lift difference between the right and left wings (Gillies et al., 2011, Parga et al., 2007). Birds generate lift differences by varying the twisting angles (i.e., angles of attack) or wing areas between the left and right wings. Even in the case of a flying robot, it is intuitive that the primary control of the roll moment is performed by the main wings. For example, Lishawk succeeded in generating a difference in the lift and roll moment by tucking wings asymmetrically (Ajanic et al., 2020). Aircraft

use ailerons to generate a difference in lift and morphing mechanisms have been designed specifically for small aerial robots (e. g., Luca et al., 2017, Stanford et al., 2007). Our results indicate that the benefits of the roll moment generated by the tail are limited to supporting subtler control, rather than agile maneuvers (Harvey et al., 2022).

The yaw moment is clearly controllable by rudder and tilt changes in the tail. In particular, it was quantitatively determined that the yaw moment was greater when the tail was tilted than when the rudder angle was biased. It is also apparent from our study that tilting the tail is an effective method for obtaining a yaw moment because tail tilt does not significantly change the lift-drag ratio or other aerodynamic moments (Figs. 5.4(C), 5.8(B), 5.8(B), and 5.10(B)). In the real world, it is common for birds and aircraft to roll their bodies and make banked turns when they need to turn quickly (Gillies et al., 2011) and it is unlikely that the yaw moment of the tail will be able to produce such turns by itself. However, in cases such as aerial imaging, it is necessary to change direction slowly without banking. In aircraft, such yaw turns can be made with rudder, but in birds, it has been shown that such slow turns can also be made by tilting the tail wing. Additionally, it is considered that the tilt rotation of the tail functions to actively improve the yaw stability as an alternative to the vertical tail of an aircraft (Thomas, 1993a). However, if stability is a priority, the use of a vertical tail, that improve yaw stability of aircraft, could be more effective. On the other hand, if turning performance is a priority, it may be effective to reduce the stability by utilizing a morphing tail wing.

The results of this study show that each angle of a tail affects the forces/moments of several axes simultaneously. When the tail is applied to an aerial robot, it may be more desirable from the perspective of simplification of design and control if the moments around each axis can be controlled separately at each angle of the tail. Therefore, this complexity should be taken into account when using tails for attitude control of flying robots.

References

Ajanic, E., Feroskhan, M., Mintchev, S., Noca, F., and Floreano, D. (2020) Bioinspired wing and tail morphing extends drone flight capabilities. *Sci. Robot.* **5**, eabc2897, doi: 10.1126/scirobotics.abc2897.

Balmford, A., Jones, I. L., and Thomas, A. L. R. (1993) On avian asymmetry: evidence of natural selection for symmetrical tails and wings in birds. *Proc. Biol. Sci.* **252**, 245–251, doi:10.1098/rspb.1993.0072.

Brown, R. E. and Fedde, M. R. (1993) Airflow sensors in the avian wing. *J. Exp. Biol.* **179**, 13-30.

Chang, E., Matloff, L. Y., Stowers, A. K., and Lentink, D. (2020) Soft biohybrid morphing wings with feathers underactuated by wrist and finger motion. *Sci. Robot.* **5**, eaay1246, doi: 10.1126/scirobotics.aay1246.

Folkertsma, G. A., Straatman, W., Nijenhuis, N., Venner, C. H., and Stramigioli, S. (2017) Robird: a robotic bird of prey. *IEEE Robot. Autom. Mag.* **24**, 22-29, doi: 10.1109/MRA.2016.2636368.

Gatesy, S. M. and Dial, K. P. (1996) From frond to fan: Archaeopteryx and the evolution of short-tailed birds. *Evolution* **50**, 2037-2048, doi: 10.1111/j.1558-5646.1996.tb03590.x.

Gatesy, S. M. and Dial, K. P. (1993) Tail muscle activity patterns in walking and flying pigeons (*Columba livia*). *J. Exp. Biol.* **176**, 55–76, doi: 10.1242/jeb.176.1.55.

Gerdes, J., Holness, A., Perez-Rosado, A., Roberts, L., Greisinger, A., Barnett, E., Kempny, J., Lingam, D., Yeh, C. H., Bruck, H. A., and Gupta, S. K. (2014) Robo Raven: A flapping-wing air vehicle with highly compliant and independently controlled wings. *Soft Robot.* **1**, 275-288, doi: 10.1089/soro.2014.0019.

Gillies, J. A., Thomas, A. L. R., and Taylor, G. K. (2011) Soaring and manoeuvring flight of a steppe eagle *Aquila nipalensis*. *J. Avian Biol.* **42**,.377-386, doi: 10.1111/j.1600-048X.2011.05105.x.

Harvey, C., Gamble, L. L., Bolander, C. R., Hunsaker, D. F., Joo, J. J., and Inman, D. J. (2022) A review of avian-inspired morphing for UAV flight control. *Prog. Aeosp. Sci.* **132**, 100825, doi: 10.1016/j.paerosci.2022.100825.

Liu H. (2020) Simulation-based insect-inspired flight systems. *Curr. Opin. Insect Sci.* **42**, 105-109, doi: 10.1016/j.cois.2020.10.001.

Luca, M. D., Mintchev, S., Heitz, G., Noca, F., and Floreano, D. (2017) Bioinspired morphing wings for extended flight envelope and roll control of small drones. *Interface Focus.* **7**, 20160092, doi: 10.1098/rsfs.2016.0092.

Maybury, W. J., Rayner, J. M.V., and Couldrick, L. B. (2001) Lift generation by the avian tail. *Proc. R. Soc. Lond. B* **268**, 1443-1448, doi: 10.1098/rspb.2001.1666.

Nickols, F. and Lin, Y. J. (2017) Feathered tail and pygostyle for the flying control of a bio-mimicking eagle bird robot. *Proceedings of 2017 IEEE 8th International Conference on Cybernetics and Intelligent Systems and Robotics, Automation and Mechatronics*, 556-561, doi: 10.1109/ICCIS.2017.8274837.

Parga, J. R., Reeder, M. F., Leveron, T., and Blackburn, K. (2007) Experimental study of a micro air vehicle with a rotatable tail. *J. of Aircr.* **44**, 1761-1768, doi: 10.2514/1.24192.

Sachs G. (2007) Tail effect on yaw stability in birds. *J. Theor. Biol.* **249**, 464-472, doi: 10.1016/j.jtbi.2007.07.014.

Stanford, B., Abdulrahim, M., Lind, R., and Ifju, P. (2007) Investigation of membrane actuation for roll control of a micro air vehicle. *J. of Aircr.* **44**, 741-749, doi: 10.2514/1.25356.

Thomas A. L. R. (1993a) On the aerodynamics of birds' tails. *Phil. Trans. R. Soc. Lond. B* **340**, 361-380, doi: 10.1098/rstb.1993.0079.

Thomas A. L. R. (1993b) The aerodynamic costs of asymmetry in the wings and tail of birds: asymmetric birds can't fly round tight corners. *Proc. R. Soc. Lond. B* **254**, 181-189, doi: 10.1098/rspb.1993.0144.

Thomas A. L. R. (1996a) The Flight of Birds that have Wings and a Tail: Variable Geometry Expands the Envelope of Flight Performance. *J. Theor. Biol.* **183**, 237–245, doi:10.1006/jtbi.1996.0217.

Thomas A. L. R. (1996b) Why do Birds have Tails? The Tail as a Drag Reducing Flap, and Trim Control. *J. Theor. Biol.* **183**, 247-253, doi:10.1006/jtbi.1996.0218.

Videler, J. J., Weihs, D., and Daan, S. (1983) Intermittent gliding in hunting flight of the Kestrel, *Falco tinnunculus* L. *J. Exp. Biol.* **102**, 1-12, doi: 10.1242/jeb.102.1.1.

Videler, J. J. (2006) *Avian flight*, Oxford scholarship online, doi: 10.1093/acprof:oso/9780199299928.001.0001.

Watkins, S., Burry, J., Mohamed, A., Marino, M., Prudden, S., Fisher, A., Kloet, N., Jakobi, T., and Clothier, R. (2020) Ten questions concerning the use of drones in urban environments. *Build.*

*Environ.***167**, 106458, doi: 10.1016/j.buildenv.2019.106458.

Williams H. J., Shepard E. L. C., Holton M. D., Alarcon P. A. E., Wilson R. P., and Lambertucci S. A. (2020) Physical limits of flight performance in the heaviest soaring bird. *Proc. Natl. Acad. Sci. U. S. A.* **117**, 17884-17890, doi: 10.1073/pnas.1907360117.

Xu, X., Zhou, Z., Dudley, R., MacKem, S., Chuong, C. M., Erickson, G. M., and Varricchio, D. J. (2014) An integrative approach to understanding bird origins. *Science* **346**, 1253293, doi: 10.1126/science.1253293.

Yang, W., Wang, L., and Song, B. (2018) Dove: A biomimetic flapping-wing micro air vehicle. *Int. J. Micro Air Veh.* **10**, 70-84, doi: 10.1177/1756829317734837.

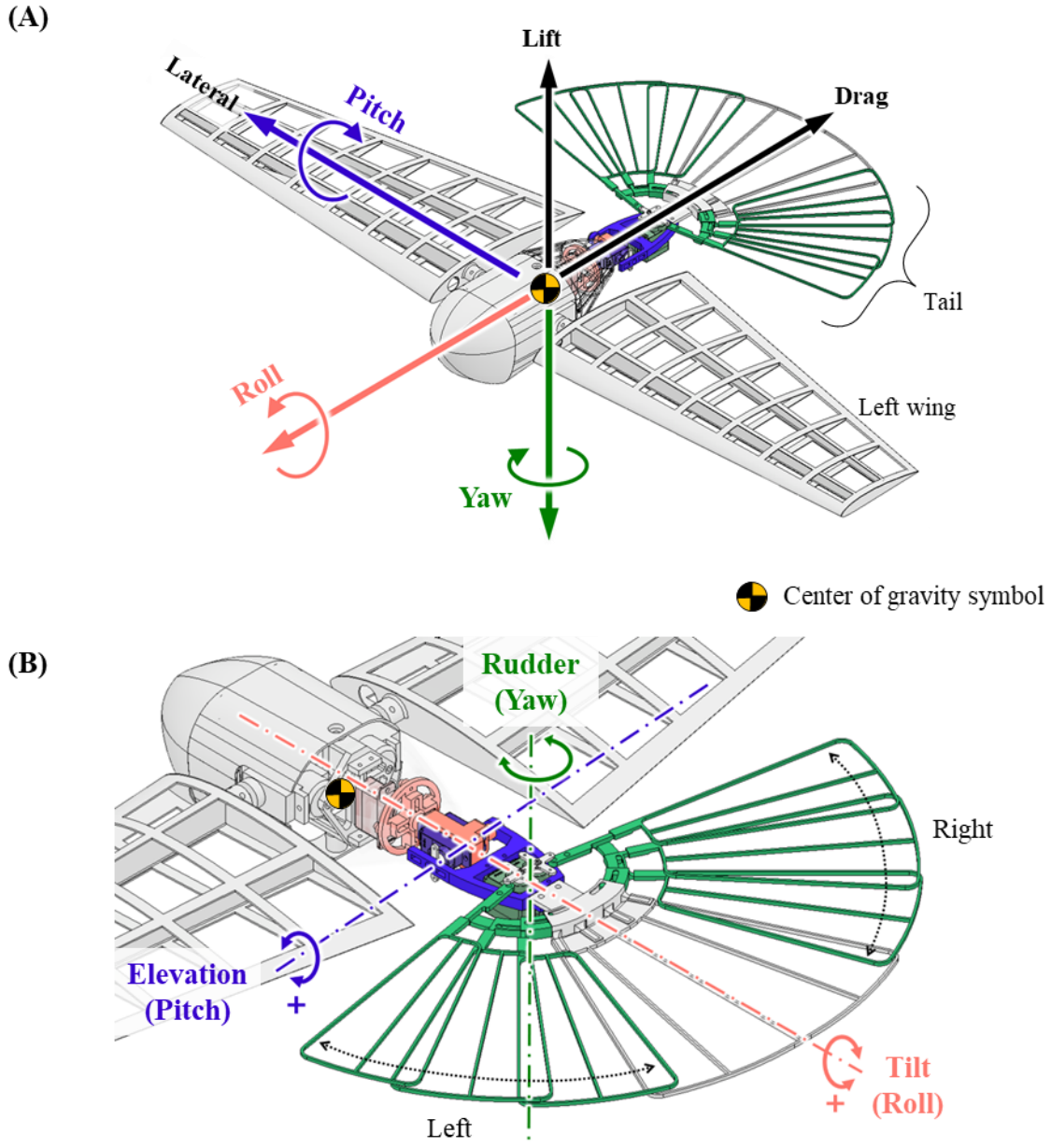

Fig. 5.1 Design of bird-inspired robot with a morphing tail mechanism. (A) Overview of the entire body from the diagonal-forward-left angle. (B) Overview of tail mechanism with tilt, elevation, and rudder motions from the diagonal-backward-left angle.

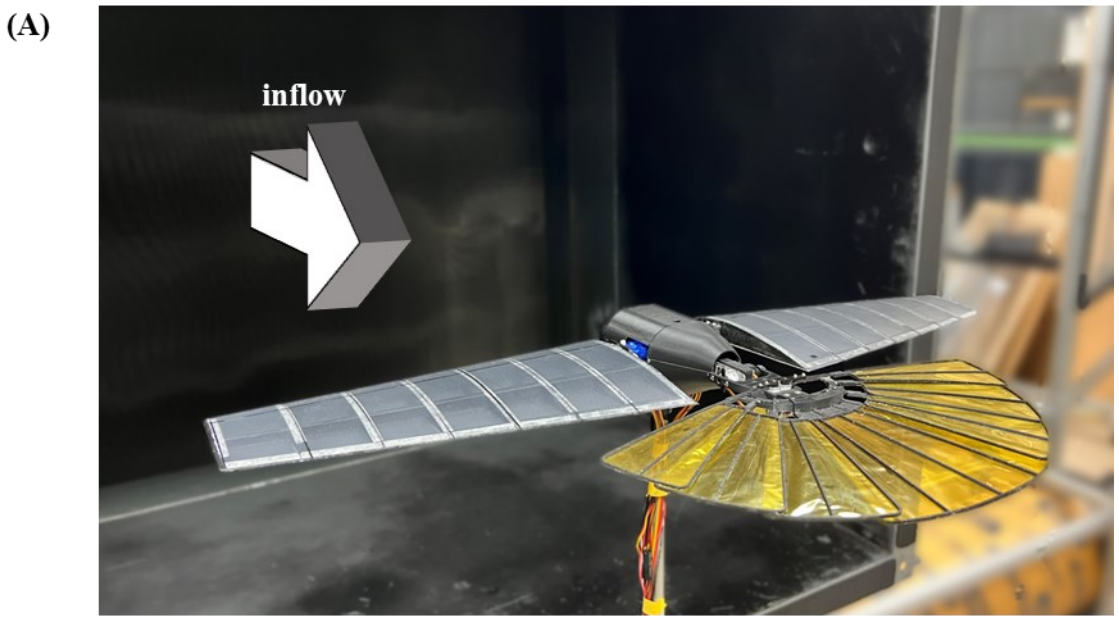

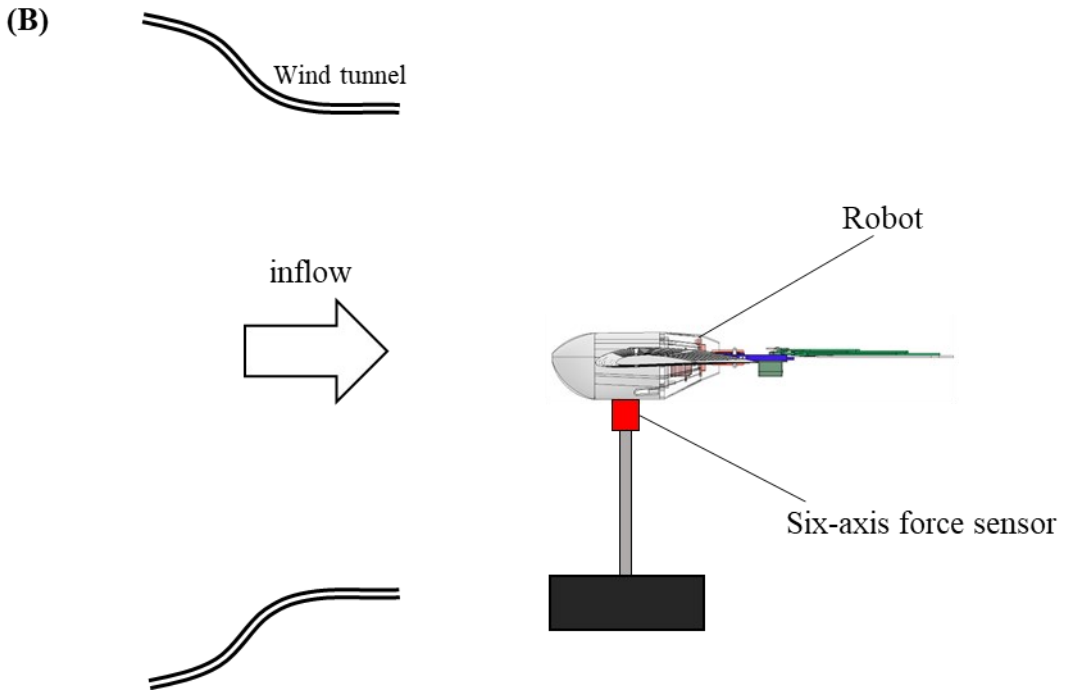

Fig. 5.2 Setup for wind tunnel experiments. (A) Viewpoint from the diagonal-backward-left angle. (B) Schematic diagram of the setup from the side view (not to scale).

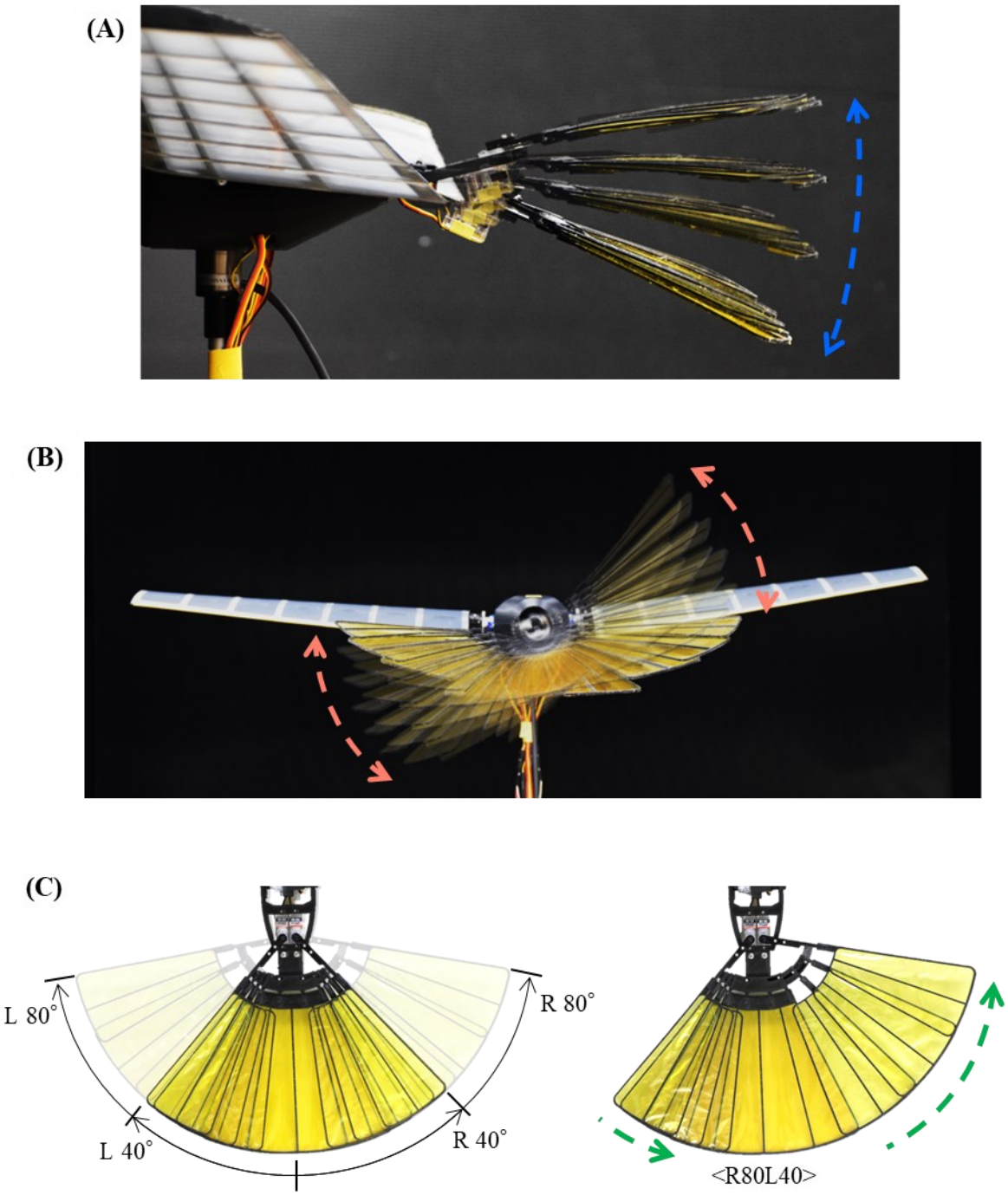

Fig. 5.3 Variations of tail postures. (A) Elevating movement of the tail feathers viewed from the side. (B) Tilting movement viewed from behind. (C) Rudder movement viewed from the top.

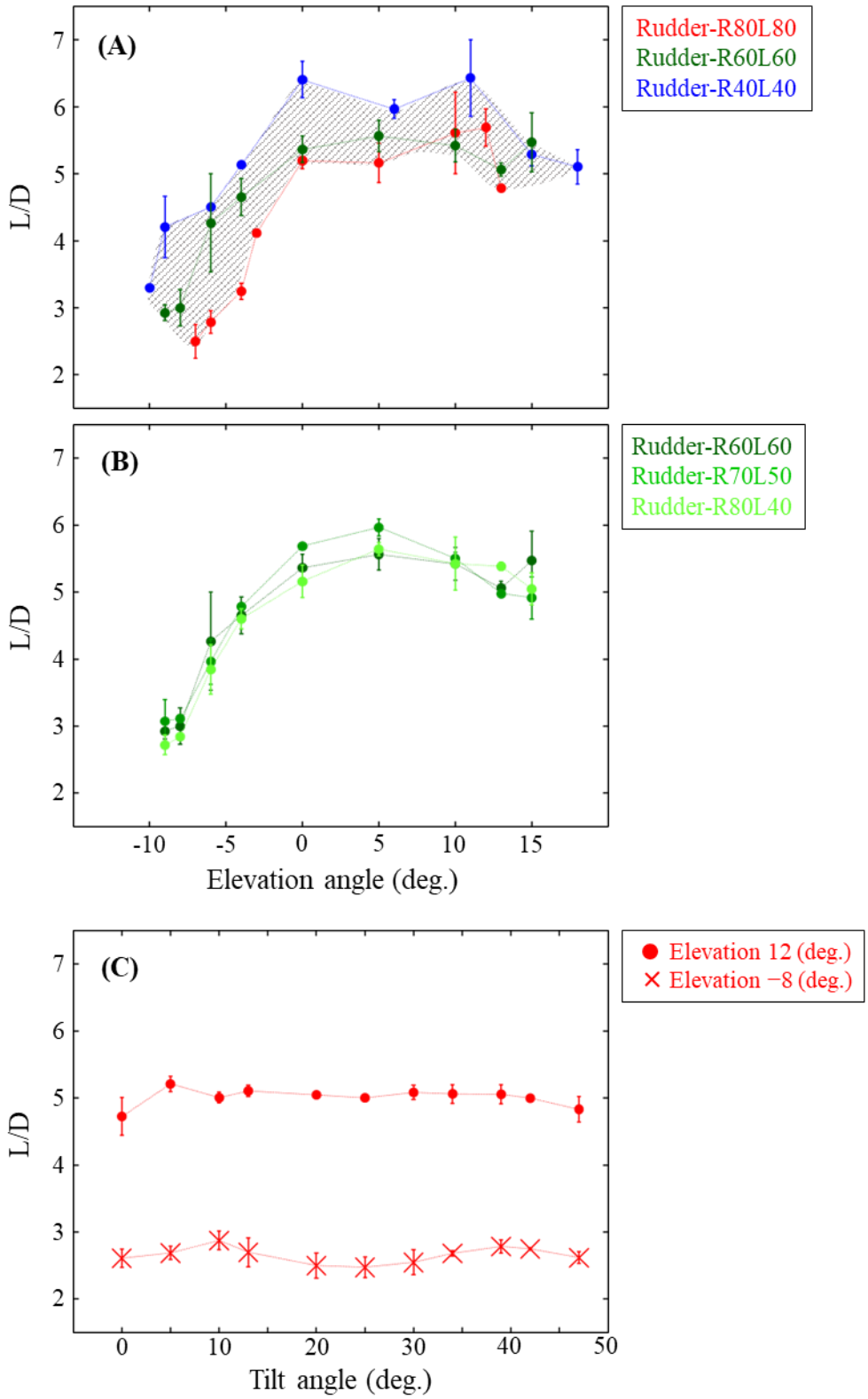

Fig. 5.4 Effects of elevation angle with (A) symmetric and (B) asymmetric tail and of (C) tilt angle on the lift/drag ratio.

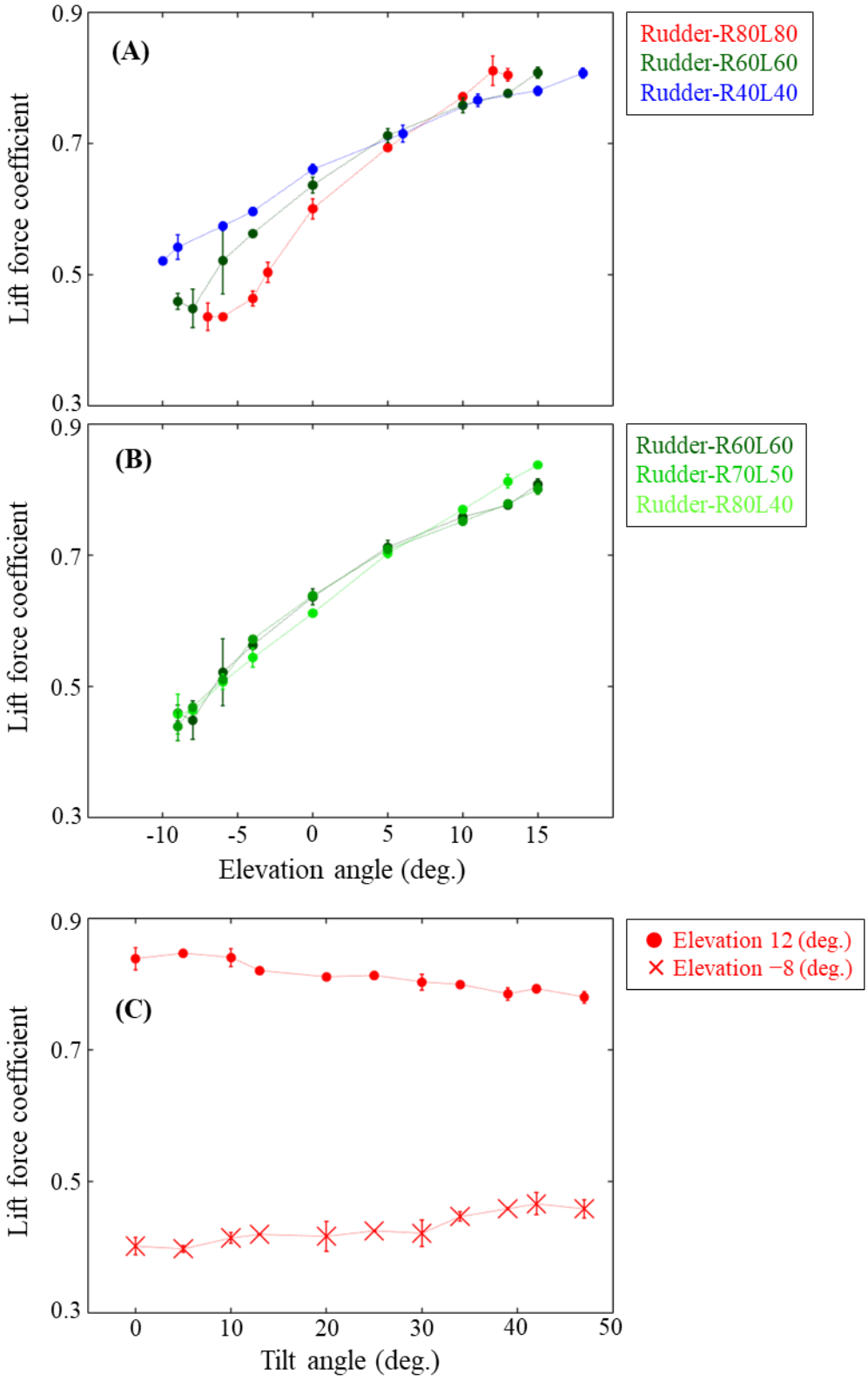

Fig. 5.5 Effects of elevation angle with (A) symmetric and (B) asymmetric tail and of (C) tilt angle on the lift force coefficient.

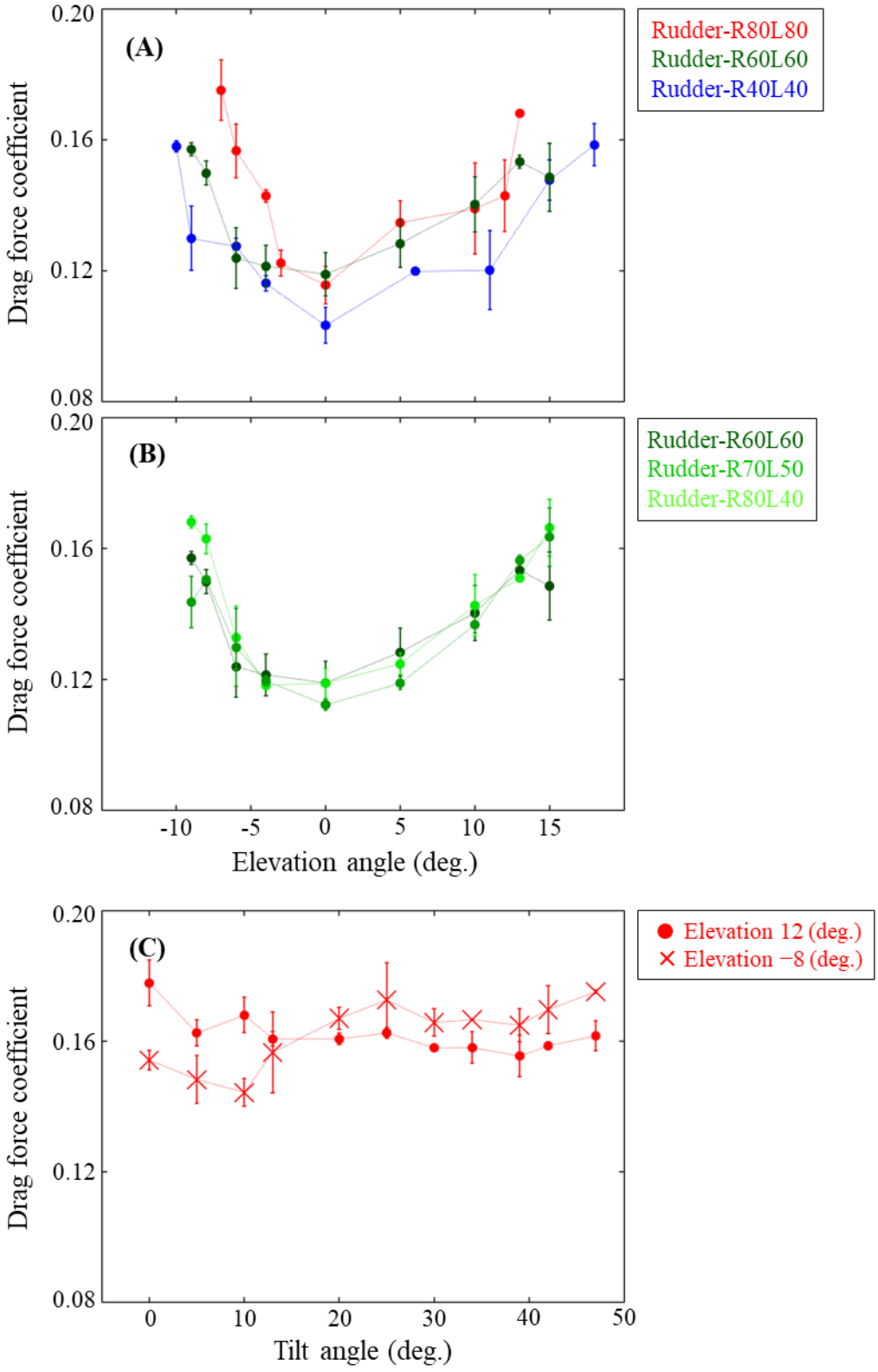

Fig. 5.6 Effects of elevation angle with (A) symmetric and with (B) asymmetric tail and of (C) tilt angle on the drag force coefficient.

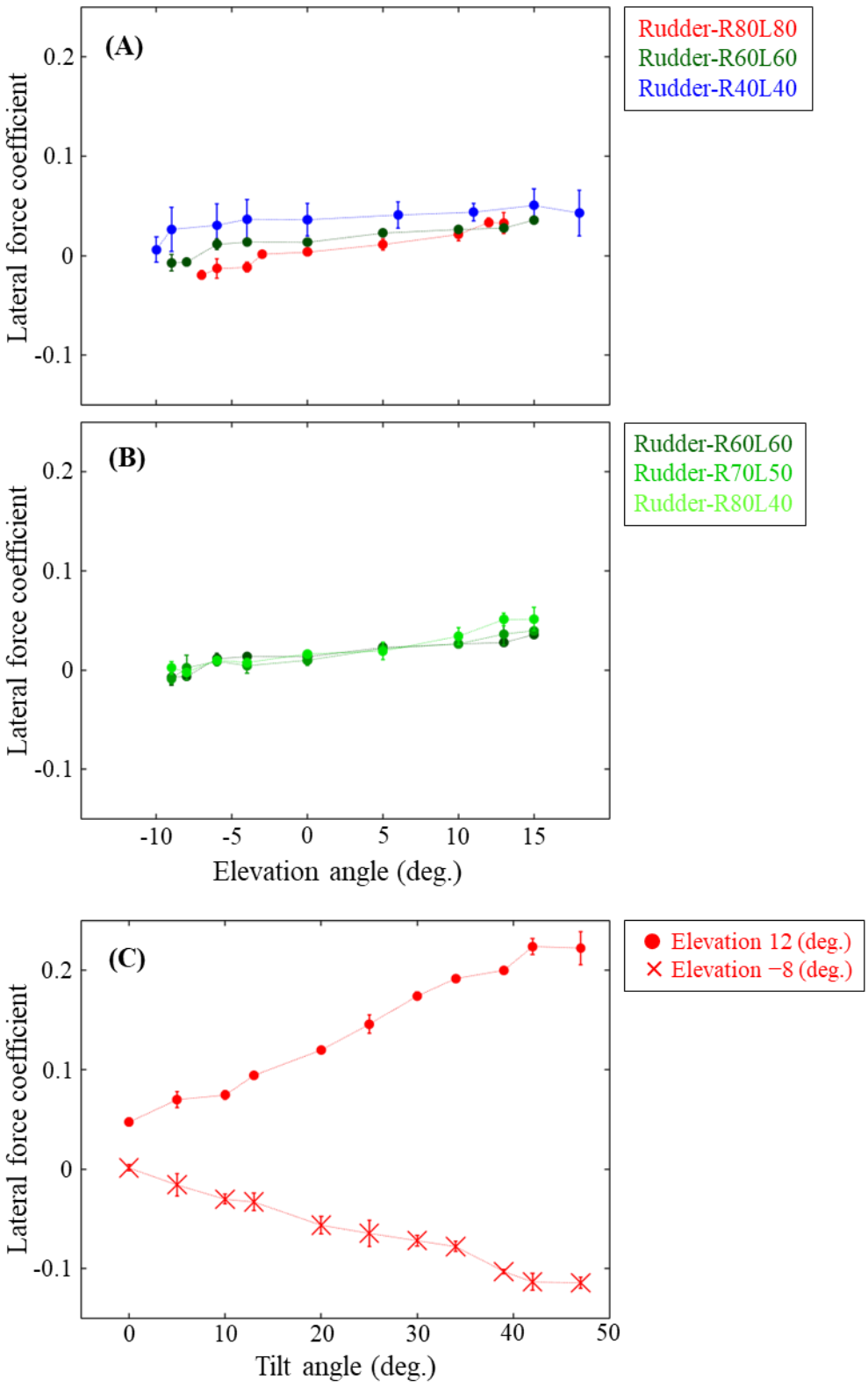

Fig. 5.7 Effects of elevation angle with (A) symmetric and with (B) asymmetric tail and of (C) tilt angle on the lateral force coefficient.

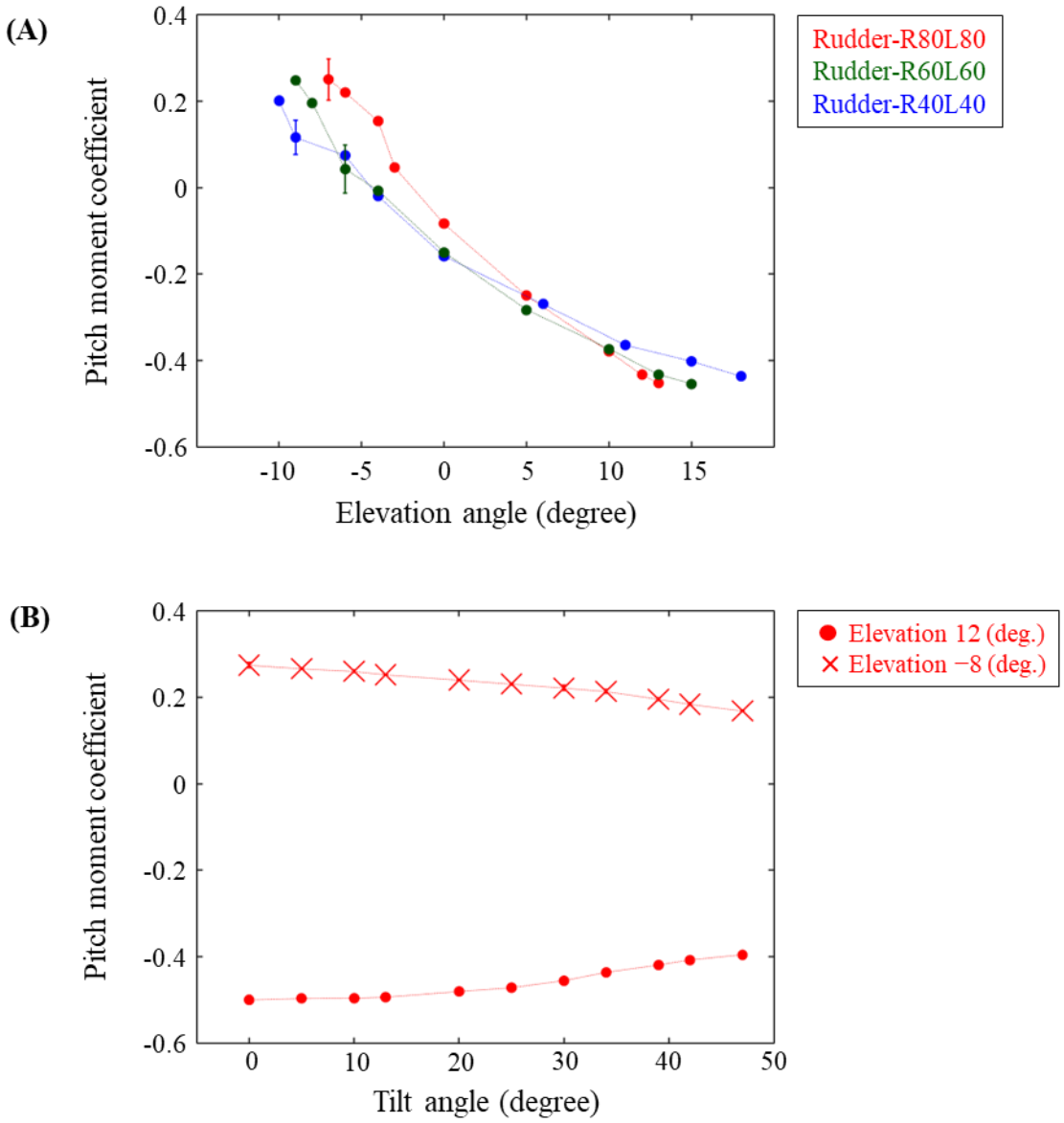

Fig. 5.8 Effects of (A) elevation angle and (B) tilt angle with symmetric tail on the pitch moment coefficient.

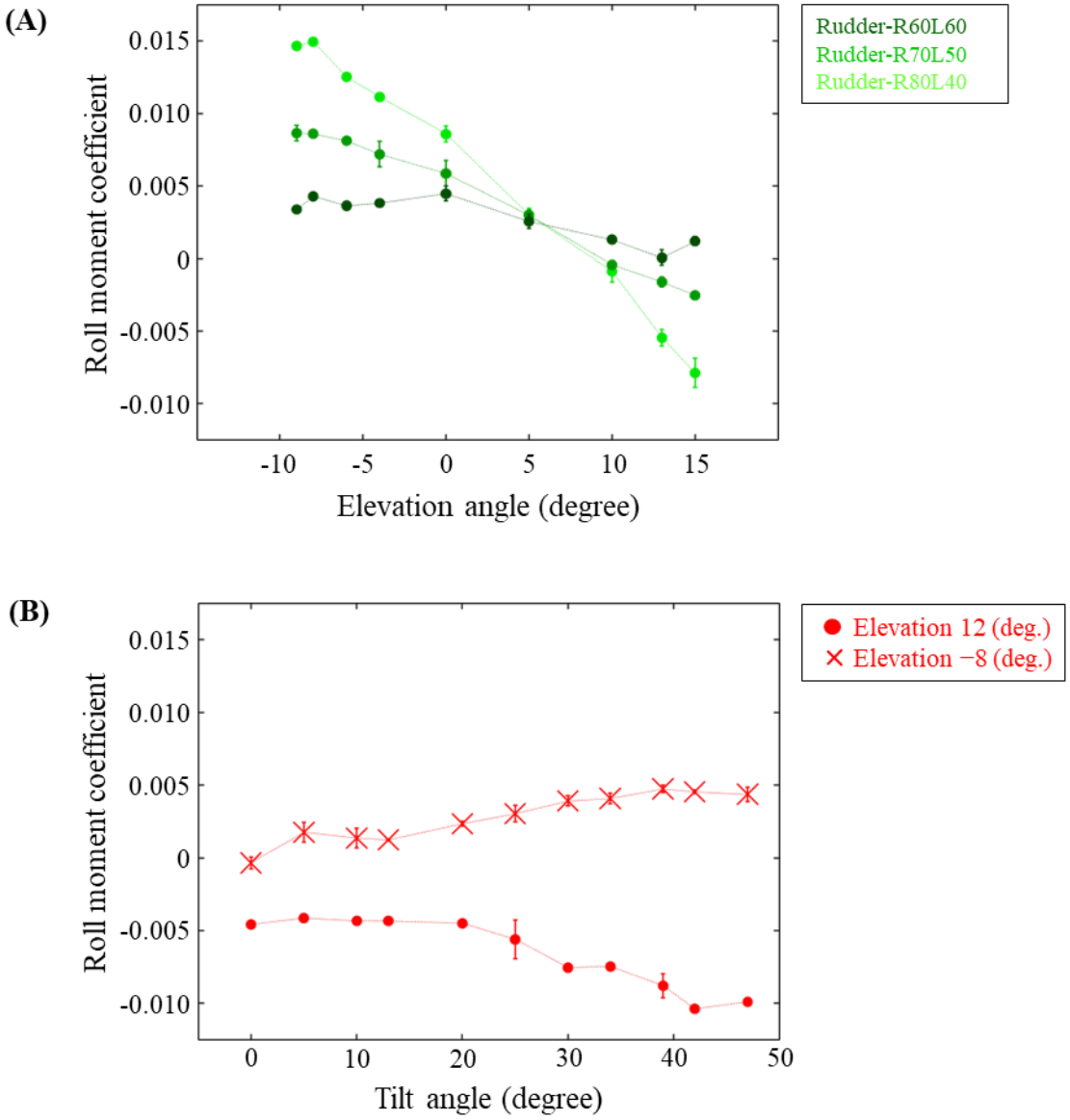

Fig. 5.9 Effects of (A) elevation angle with asymmetric tail and (B) tilt angle with symmetric tail on the roll moment coefficient.

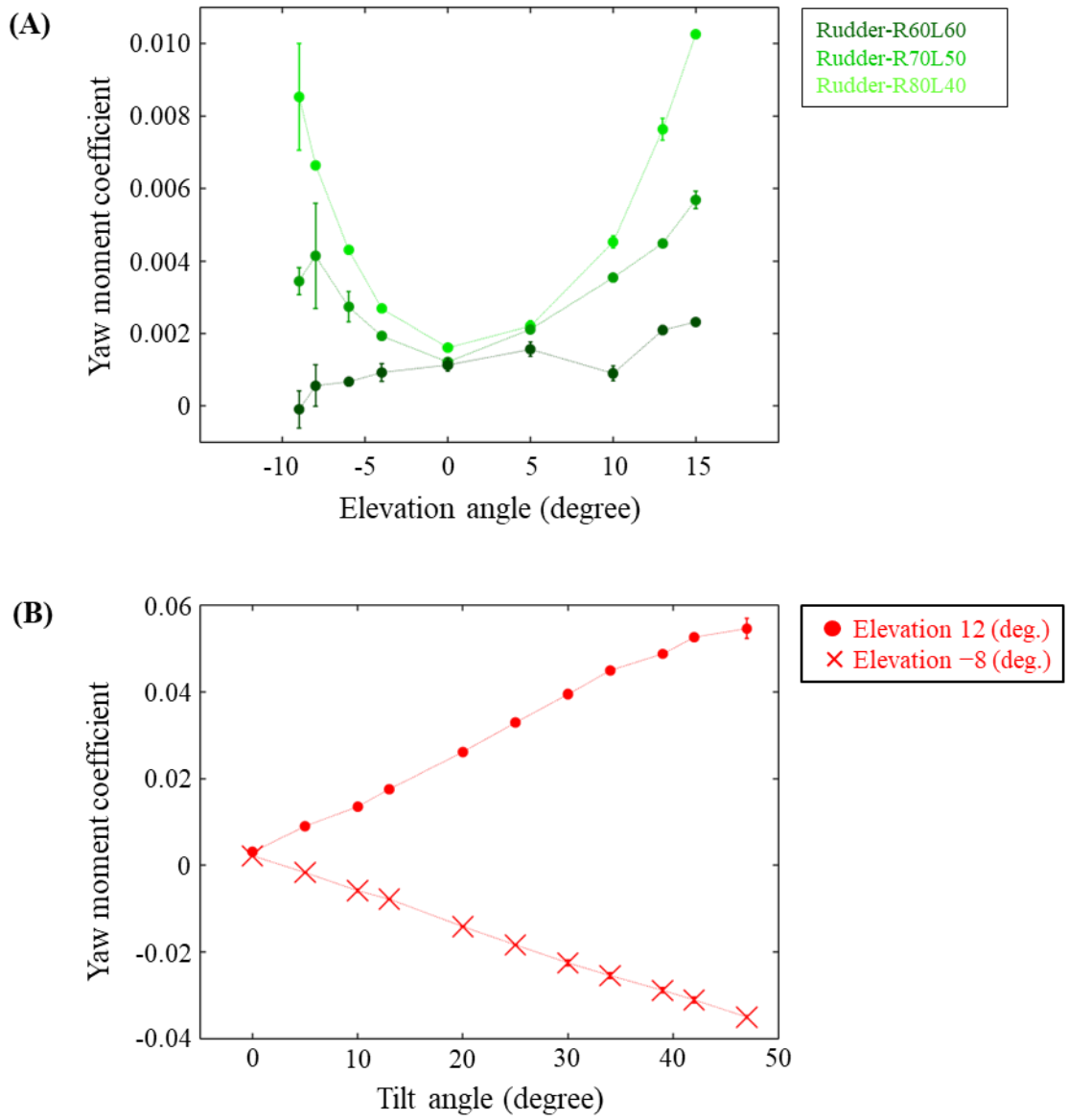

Fig. 5.10 Effects of (A) elevation angle with asymmetric tail and (B) tilt angle with symmetric tail on the yaw moment coefficient.

Table 5.1 Specifications of the bird-inspired morphing tail

Dimensions	Symbol	Units	Value
Tail feather length	l	m	0.1
Tail area (R40L40 / R60L60 / R80L80)	S_t	m^2	0.0069 / 0.010 / 0.014
Moment of inertia around tilt axis (R80L80)	I_t	$g \cdot mm^2$	32,000
Moment of inertia around elevation axis (R40L40 / R60L60 / R80L80)	I_e	$g \cdot mm^2$	115,000 / 106,000 / 89,000
Moment of inertia around rudder axis	I_r	$g \cdot mm^2$	62,000

Table 5.2 Attitudes of the morphing tail

Postures	Tilt (°)	Elevation (°)	Right Rudder (°)	Left Rudder (°)
Elevating with R80L80 (max spread)	0	−8 ~ 12	80	80
Elevating with R40L40 (min spread)	0	−10 ~ 18	40	40
Elevating with R60L60 (mid spread)	0	−9 ~ 15	60	60
Elevating with R70L50	0	−9 ~ 15	70	50
Elevating with R80L40	0	−9 ~ 15	80	40
Tilting with elevation down (max spread)	0 ~ 50	12	80	80
Tilting with elevation up (max spread)	0 ~ 50	−8	80	80

Chapter 6

Conclusions

6.1 Conclusions

In this thesis, several methods based on passive mechanisms for a flying robot to tackle the effects of wind disturbances were presented. Aiming at developing a highly robust flying robot against wind effects, fabrication of the bird-inspired robot, that has multi-degrees-of-freedom for attitude transformation and can be equipped with the airflow sensor developed in this thesis was also carried out.

The aerodynamic performance of a wing model with flexible flaps, inspired by covert feathers of birds, has been investigated experimentally with a specific focus on its robustness against disturbances. In the wind tunnel experiments, several wing models with covert-inspired flaps of different stiffness were tested. In order to evaluate the aerodynamic performance of wing models, aerodynamic force measurements by a force sensor and PIV measurements for visualizing the flow fields near the wing were conducted. The force measurements revealed that the wing model with flexible flaps could lead to significantly suppressing the fluctuations of aerodynamic forces in both uniform and disturbed flows, corresponding with a pronounced reduction in the magnitude of vorticity on the upper surface of the wing with flexible flaps. Such reduction in the variation of aerodynamic forces was further confirmed to be strongly dependent on the stiffness of the flaps, and thus, there likely exists an optimal stiffness of the flexible flaps capable of reducing the disturbance-induced fluctuations at some specific disturbance frequencies. these results indicate that the avian covert feathers near the leading-edge may work as a passive flow-control device to enhance the aerodynamic robustness under aerial disturbances. Given its simplicity, the feather-inspired attachment can be used as an effective method for improving the flight stability of small drones with fixed wing working in an environment with various disturbances.

Aiming at application for a flying robot, two types of flexible airflow sensor were designed and fabricated. Both types were designed to be shaped like cantilever, that are also inspired by covert feathers. One is strain-gauge-type sensor with flexible PET sheet printed by silver nano-ink circuit whose design was based on common strain gauge and quarter-bridge circuit. The other is hall-effect-type sensor configured from hall-effect IC, flexible PET sheet with silver nano-ink pattern, and magnet. These sensors were mounted on the wing model and tested in wind tunnel. It was found that both types of sensors shaped like cantilever mounted on the wing surface responded to the change in airflow near the wing surface. Strain-gauge-type sensor had an advantage of a simple fabrication method, however, its performance as an airflow sensor was worse than hall-effect-type sensor due to its difficulty in mechanical and electrical design of a strain gage. On the other hand, hall-effect-type sensor showed better performance than strain-gauge-type sensor in terms of responsiveness to airflow and reproducibility. It was demonstrated that the wing can be enhanced its aerodynamic performance and acquire redundant airflow sensing capabilities by attaching multiple hall-effect-type sensors to the wing model.

Development of bird-inspired robot with multi-degrees-of-freedom attitude control mechanisms in the wings and tail was further carried out. In this study, the aerodynamic performance of a bird-inspired morphing tail mechanism with three degrees of freedom associated with tilt, elevation, and rudder was investigated, with a specific focus on the effect of the morphing tail mechanism on aerodynamic controllability. Through wind tunnel experiments, it was confirmed that both the aerodynamic performance and maneuverability of a bird-inspired flying robot can be controlled by adjusting its tail attitude. The tail mechanism was further verified to be redundant in the production of aerodynamic forces and moments, which may provide an effective approach to achieve flight stabilization under complex conditions with wind gusts in unsteady natural environments. These results point to the capability and importance of tail-based control strategies for adjusting aerodynamic forces and moments, which may provide a useful biomimetic design for bird-inspired aerial vehicles or drones.

6.2 Future tasks and prospects

Findings from the several experiments conducted in this thesis indicate that feather-based flexible structures can be used as a stall prediction sensor while suppressing the effect of wind disturbance. Experimental findings on further fabricated flying robot, particularly on the morphing tail, have clearly shown that the morphing tail can assist in the active control and production of aerodynamic forces and moments. Utilizing aerodynamic control strategies based on airflow sensing capabilities and morphing wings and tails to achieve flight stabilization and maneuvers in unpredictable winds for both birds and bird-inspired flying robots remains an important topic for further research. Active and passive control mechanisms in biological flyers such as insects, bats, and birds are considered to play a crucial role in achieving diverse, robust flight patterns in various complex conditions (Harvey et al., 2022; Liu, 2020).

In order to achieve highly stable flight under untethered and disturbed-wind conditions, further studies on the flight robot integrating a feather-based structures, passive mechanisms for airflow sensing and suppressing the effects of wind disturbances, and morphing wing and tail, an active mechanism for aerodynamic control will be studied. The following research task is the development of a flight system that learns the predictive signs of wind conditions that cause the flying robot to lose its posture and controls the morphing wing and tail of the robot to maintain a stable posture in response to wind disturbances. Another research task is to explore the feasibility of a flight control method using reinforcement learning in real flying robots, as legged robot systems using methods adapted for deep reinforcement learning have been demonstrated on real robots (Haarnoja et al., 2019; Hwangbo et al., 2019). If stable hovering utilizing wind energy is achieved by reinforcement learning in the flying robot, it may provide more efficient hovering flight than a multirotor drone because the bird-inspired flying robot can perform hanging flight without enormous energy consumption.

Reference

Haarnoja, T., Ha, S., Zhou, A., Tan, J., Tucker, G., and Levine, S. (2019) Learning to walk via deep reinforcement learning. *Proceedings of Robotics: Science and Systems XV*, doi: 10.15607/RSS.2019.XV.011.

Harvey, C., Gamble, L. L., Bolander, C. R., Hunsaker, D. F., Joo, J. J. and Inman, D. J. (2022) A review of avian-inspired morphing for UAV flight control. *Prog. Aeosp. Sci.* **132**, 100825, doi: 10.1016/j.paerosci.2022.100825.

Hwangbo, J., Lee, J., Dosovitskiy, A., Bellicoso, D., Lee, J., Tsounis, V., Koltun, V., and Hutter, M. (2019) Learning agile and dynamic motor skills for legged robots. *Sci. Robot.* **4**, eaau5872, doi: 10.1126/scirobotics.aau5872.

Liu H. (2020) Simulation-based insect-inspired flight systems. *Curr. Opin. Insect Sci.* **42**, 105-109, doi: 10.1016/j.cois.2020.10.001.

List of Publications

Research Articles in Journals

(1) **Yuta MURAYAMA**, Toshiyuki NAKATA, and Hao LIU, Flexible flaps inspired by avian feathers can enhance aerodynamic robustness in low Reynolds number airfoils, Frontiers in Bioengineering and Biotechnology, 9:612182, 7 May 2021.

(2) **Yuta MURAYAMA**, Toshiyuki NAKATA, and Hao LIU, Aerodynamic performance of a bird-inspired morphing tail, Journal of Biomechanical Science and Engineering, 8 Dec. 2022.

Conference Publications

(A) *International conferences*

(A-1) **Yuta MURAYAMA**, Toshiyuki NAKATA, Hao LIU, Development of bird-inspired wings with flexible flaps inspired by avian covert feathers for flight robots, SICB+, AZ, USA, 14 Jan.–31 Mar. 2022. (Online presentation)

(B) *Academic conferences*

(B-1) 村山友太，中田敏是，劉浩，鳥の羽根を規範とした柔軟翼を用いたカイトプレーンの外乱応答特性，ロボティクス・メカトロニクス講演会 2020，1P1-L04，石川，2020 年 5 月．（オンライン発表）

(B-2) 姜雅珺，村山友太，村上正志，鳥類翼形態と機能の関係：飛翔の安定性に着目して，第 68 回日本生態学会，岡山，2021 年 3 月．

(B-3) 村山友太，中田敏是，劉浩，高ロバストドローンの創製に向けた羽根規範フレキシブル風況センサの特性評価，ロボティクス・メカトロニクス講演会 2022，2A1-G06，札幌，2022 年 6 月．

(B-4) 保科潤，村山友太，中田敏是，劉浩，鳥の羽根を規範とした風センサによる失速の検知，第 34 回バイオエンジニアリング講演会，1P4-04，福岡，2022 年 6 月．

(B-5) 村山友太，中田敏是，劉浩，ロボットを用いた鳥類の尾羽の空力性能評価とその進化に関する考察，第 33 回バイオフロンティア講演会，1A05，兵庫，2022 年 12 月.

(B-6) 保科潤，村山友太，中田敏是，劉浩，羽根規範型風センサを搭載した飛行ロボットの姿勢制御，第 33 回バイオフロンティア講演会，1F05，兵庫，2022 年 12 月.